Evidence-Based Complementary and Alternative Medicine

Ancient Classical Formulas in Treating Chronic and Critical Diseases

Lead Guest Editor: Jun Jiang
Guest Editors: Chao Liang, Jie Wan, and Jiangning Yin

Ancient Classical Formulas in Treating Chronic and Critical Diseases

Evidence-Based Complementary and Alternative Medicine

Ancient Classical Formulas in Treating Chronic and Critical Diseases

Lead Guest Editor: Jun Jiang
Guest Editors: Chao Liang, Jie Wan, and Jiangning Yin

Contents

Hindawi
Evidence-Based Complementary and Alternative Medicine
Volume 2023, Article ID 3071147, 19 pages
https://doi.org/10.1155/2023/3071147

Research Article

Pharmacodynamic Material Basis and Potential Mechanism Study of Spatholobi Caulis in Reversing Osteoporosis

Jianpeng Xiao,[1,2] **Wei Shang**,[1] **Zhiming Zhao**,[1] **Jun Jiang**,[1,2] **Jianping Chen**,[3] **Hui Cai**,[1] **Jinjin He**,[2] **Zhihui Cai**,[2] **and Zihan Zhao**[2]

[1]*Department of TCM, Jinling Hospital, School of Medicine, Nanjing University, Nanjing, China*
[2]*School of Pharmacy, Jiangsu University, 301# Xuefu Road, Zhenjiang 212013, Jiangsu, China*
[3]*School of Chinese Medicine, The University of Hong Kong, 10 Sassoon Road, Pokfulam, Hong Kong, China*

Correspondence should be addressed to Jun Jiang; jiangjuntcm2007@hotmail.com, Jianping Chen; jpjpchen@yahoo.com, and Hui Cai; njzy_caihui@163.com

Received 20 January 2022; Accepted 3 September 2022; Published 14 April 2023

Academic Editor: Ammar AL-Farga

Objective. To elucidate the mechanism of Spatholobi Caulis (SC) in treating osteoporosis (OP) integrated zebrafish model and bioinformatics. *Methods*. Skeleton staining coupled with image quantification was performed to evaluate the effects of SC on skeleton mineralization area (SSA) and total optical density (TOD). Zebrafish locomotor activity was monitored using the EthoVision XT. Bioactive compounds of SC and their corresponding protein targets were acquired from Traditional Chinese Medicine Systems Pharmacology (TCMSP) database. Potential therapeutic targets for OP were summarized through retrieving 5 databases, and then, the overlapping genes between SC and OP were acquired. The core genes were selected by CytoHubba. Subsequently, Kyoto Encyclopedia of Genes and Genomes (KEGG) pathway and Gene Ontology (GO) functional analysis of the intersection target genes were carried out by R software. Finally, the molecular docking simulation was manipulated between the ingredients and the hub genes. *Results*. Compared with the model group, SC significantly increased the SSA and TOD at 10 mg/mL and improved the locomotor activity in a dose-dependent manner ($p < 0.001$). 33 components of SC were associated with 72 OP-related genes including 10 core genes (MAPK1, VEGFA, MMP9, AKT1, AR, IL6, CALM3, TP53, EGFR, and CAT). Advanced Glycation End Product (AGE) Receptor for AGE (RAGE) signaling pathway was screened out as the principal pathway of SC in anti-OP. The bioactive components (Aloe-emodin, Emodin, Formononetin, Licochalcone A, Luteolin, and Lopac-I-3766) have excellent affinity to core genes (MAPK1, VEGFA, MMP9, AKT1, and IL6). *Conclusion*. SC had the hierarchical network characteristics of "multicomponents/multitargets/multifunctions/multipathways" in reversing OP, but AGE-RAGE signaling pathway may be the main regulatory mechanism.

1. Introduction

Osteoporosis (OP) is a common systemic bone disease with a significant impact on human health and characterized by low bone quality, low bone density, and bone microstructure destruction, which easily leads to decreased bone strength and increased fracture risk [1–3]. OP has been considered a silent disease, for it is usually asymptomatic and cannot be detected until the first fracture occurs [4–6]. According to statistics released by international osteoporosis foundation, OP worldwide causes more than 8.9 million fractures annually, and this number is projected to be tripled by 2050 [7, 8]. The increasing incidence of OP places a heavy social and economic burden on the health care system [9–11]. Despite the fact that substantial pharmacological options have been approved for the management of OP, the potential long-term adverse effects of anti-OP medications and poor adherence to the treatment urgently await more effective strategies to satisfy the unmet medical needs [12–15]. Alternative natural medicine may play an emerging role in against OP by complementarily overcoming the limitations of the current marketed medications [16–18].

Spatholobi Caulis (SC), known as Jixueteng in Chinese Pharmacopoeia (2020 version), is the vine stem of *Spatholobus suberectus* Dunn of the family Leguminosae [19]. SC is a Chinese medicine that can promote blood circulation, dispel stasis, inhibit platelet aggregation, stimulate hematopoiesis, and treat anemia and diseases related to blood stasis syndrome [19–21]. In consequence, SC has been mainly prescribed for the treatment of irregular menstruation [22, 23], dysmenorrhea [24], amenorrhea [25], rheumatism [26], blood deficiency, and chlorosis [27]. Increasing evidence suggested that SC had massive pharmacological properties, including antioxidation [28], anti-infection [29], anticancer [30], and promoted angiogenesis [31]. In addition, it was reported that SC exerted anti-OP through inhibition of osteoclastogenesis and stimulation of chondrogenesis [32]. Also, recent paper demonstrated that AGE-RAGE pathway plays a vital part in OP treatment after intervention by SC [33, 34]. However, studies on the mechanisms underlying SC's antiosteoporotic effects are still lacking.

As a new interdisciplinary developed in recent years, network pharmacology provides a "multiway," "multitarget" method for drug analysis and is similar with the thoughts of traditional Chinese medicine (TCM) compound prescription, which concurs with the characteristics of the overall compatibility of TCM and comprehensive and multipathway treatment of diseases [35]. Recently, numerous studies illustrated that network pharmacology can reach high performance on prediction the mechanism of Chinese medicine, indicating that it might become a powerful tool to systematically explore the new application of TCM [36, 37]. In this study, prednisolone- (PNSL-) induced zebrafish OP model was employed to assess the therapeutic effect of SC. Subsequently, we adopted network pharmacology to explore the underlying mechanism of SC's anti-osteoporotic effects. The major bioactive components of SC and corresponding targets were obtained, and "drug-active components-diseasetargets-signaling pathways" network was constructed. Ultimately, the potential mechanism of SC in the treatment of OP was revealed via a combination of Gene Ontology (GO) function analysis and Kyoto Encyclopedia of Genes and Genomes (KEGG) pathway enrichment analysis.

2. Materials and Methods

2.1. Experimental Animal. Zebrafish larvae were purchased from Nanjing Yishu Lihua Biotechnology Co., Ltd and cultured in blank E3 medium (containing 0.33 mM $CaCl_2$, 0.33 mM $MgSO_4$, 5 mM NaCl, and 0.17 mM KCl). Zebrafish embryos were cultured in Intelligent light incubator with a 14/10 h light/dark cycle [38, 39]. Animal experiments were carried out in accordance with the Guidelines for Animal Experimentation of Jiangsu University (Zhenjiang, China), and the protocol was approved by the Animal Ethics Committee of this institution.

2.2. Experimental Design. Newly hatched zebrafish larvae at the age of 3 days after fertilization (DAF) were placed into 6-well plates (15 larvae in each well) [40, 41]. The zebrafish larvae were randomly divided into 7 groups as follows: Control (CON, blank medium), dimethyl sulfoxide (DMSO, 0.5% DMSO), Model group (MX, 25 μM PNSL), Etidronate Disodium group (ED, 15 mM ED + 25 μM PNSL), SC-H (10 mg/mL SC + 25 μM PNSL), SC-M (1 mg/mL SC + 25 μM PNSL), and SC-L (0.1 mg/mL SC + 25 μM PNSL).

2.3. Observation of Zebrafish Locomotor Activity. After 4-day drug deliveries, zebrafish locomotor activity was monitored by EthoVision behavior system [42, 43]. The instrument parameters are set as follows: "prior to the start of tracking, the software needed to be calibrated; the video sampling rate was 25 frames per second (fps), based on the design recommendations [44]; first, under the Trial List, one trial was selected. For the Arena Settings, each well/arena was calibrated based on the diameter of the well [45]. The diameter of the wells within the well plates used in this manuscript (96-well plate) is 6.54 mm [46]. For the Detection Settings, dynamic subtraction was selected, and the dark contrast and subject contour were adjusted to optimize tracking efficiency [47, 48]. Within the Analysis Profiles, the selected dependent variables were distance moved, velocity, and time spent moving [49]. These endpoints were based on the larvae's center-point activity [50]. The results were then exported to Excel and statistical analysis software suites." According to the methods described above, moving distance (MD), moving speed (AS), travel frequency (TF), and hotspot are selected as the anti-OP drug efficiency evaluation indexes in this model.

2.4. Alizarin Red Staining. At the 10 DAF, all zebrafish larvae were collected and killed under anesthesia by 3-Aminobenzoic acid ethyl ester methanesulfonate (MS-222, 100 mg/L) [51]. After removing MS-222 solution, 4% paraformaldehyde was utilized to fix zebrafish and stained with 0.01% Alizarin Red Staining (ARS, containing 0.5% KOH) overnight [52]. After removal of ARS solution, newly prepared bleaching solution containing 1.5% H_2O_2 and 0.5% KOH was added [53]. 1.5 hours later, all zebrafish had been decolorized and preserved in different ratios of glycerol and 0.5% KOH solution [54]. The stained bones of zebrafish were observed under a microscope (Olympus IX71/IX81, Olympus Corporation, Japan). Digital images [55] were analyzed for quantification of skeleton stained area using ImageJ software. Three replicates were performed.

2.5. Screening of Active Compounds and Corresponding Target Genes in SC. Traditional Chinese Medicine Systems Pharmacology database (TCMSP) was utilized to search the bioactive components of SC, with the screening conditions

of "oral bioavailability (OB) ≥20% and drug like (DL) ≥0.1." Meanwhile, the corresponding target genes of the above components were obtained [56, 57].

2.6. Mining of OP-Related Targets. OP-related targets were collected through retrieving GeneCards [58] (https://www.genecards.org/), Online Mendelian Inheritance in Man (OMIM) [59] (https://omim.org/, updated November 25, 2020), PharmGkb [60] (https://www.pharmgkb.org/), Therapeutic Target Database (TTD) [61] (https://db.idrblab.net/ttd/), and DrugBank [62] (https://www.drugbank.org/) using the keyword "osteoporosis." The OP-related target genes were gathered, and Venn diagram was constructed.

2.7. Overlapping Targets of Drug Potential Genes and OP-Related Genes. R language [63] was applied to obtain the overlapping targets of drug potential genes and OP-related genes. These common target genes were used for further analysis.

2.8. Protein-Protein Interaction (PPI) Network and Hub Genes. PPI network was constructed when the shared target genes were imported into the STRING database [64]. Subsequently, 12 algorithms in CytoHubba, that is, Betweenness, BottleNeck, Closeness, ClusteringCoefficient, Degree, Density of Maximum Neighborhood Component (DMNC), EcCentricity, Edge Percolated Component (EPC), Maximal Clique Centrality (MCC), Maximum Neighborhood Component (MNC), Radiality, and Stress, were utilized to screen the top 10 core target genes [65, 66].

2.9. GO and KEGG Analysis. R language and Bioconductor platform were used to perform GO enrichment analysis and KEGG pathway analysis. The first 10 functional categories of biological process (BP), cellular component (CC), and molecular function (MF) were screened out to construct the histogram and bubble diagram. Then, the target proteins were analyzed using the KEGG enrichment analysis, and the top 30 signaling pathways were chosen to draw the histogram and bubble diagram.

2.10. Network Visualization of "Active Ingredients-Potential Targets-Signaling Pathways". Cytoscape software was adopted to draw a ternary network including bioactive ingredients-target genes-signaling pathways. The above bioactive components and corresponding genes were imported into the software, and the ternary network "drug-active components-potential therapeutic targets of disease-relevant signaling pathways" was drawn [67, 68].

2.11. Molecular Docking Analysis. The plug-in CytoHubba of Cytoscape software was used to screen top 10 hub genes. The core genes were selected to find the related drug components in the compound regulatory network as small molecular ligands. Molecular docking simulation was performed as previously described. The specific process is as follows: "the 2D structure information of drug chemical components was downloaded from PubChem (https://www.ncbi.nlm.nih.gov/) platform and converted into the 3D structure by ChemBio3D software, and the energy optimization of MM2 was carried out to complete the preparation of small molecule ligands. The 3D structure of the candidate target proteins was downloaded from PDB (https://www.rcsb.org/) database, and then, the protein receptors were prepared after the water molecules, and ligands were removed by PyMOL2.4.0 software. AutoDockTools software was used to read the receptor files, which were converted to PDBQT format after hydrotreating ion modification. The ligand files were also converted to PDBQT format for saving and then converted into the 2D structure to draw the active pockets. Finally, AutoDock vina software will be used for molecular docking, and the lowest free energy model is selected for visual analysis."

2.12. Statistical Analysis. The GraphPad Prism 5 software [69–71]was used for statistical analysis, and the data was expressed as the mean ± SD. The differences were performed by one-way analysis of variance, and $p < 0.05$ was considered significant difference [39, 72, 73].

3. Results

3.1. Protective Effect of SC on the Zebrafish OP Model Induced by PNSL. At the 3DAF, zebrafish were incubated with PNSL for three days in 6 well plates to establish a rapid OP model. The SSA and TOD, which represented osteoblast differentiation, were used to determine the amount of bone mineralization of zebrafish larvae. SSA and TOD of the zebrafish larvae were significantly lower in the PNSL-treated groups than in the DMSO with values of 51423.33 and 19405.03, respectively, indicating that PNSL reduced bone mineralization and inhibited osteogenic differentiation in zebrafish larvae (Figure 1). When PNSL-induced zebrafish was treated with 0.1, 1, and 10 mg/mL SC, higher mineralization of the vertebrate column was discovered in a dose-dependent pattern. SSA and TOD were significantly increased to 295764.70 and 109542.50 at 10 mg/mL, respectively, as shown in Figure 1. In conclusion, the study indicated that SC could reverse the bone loss of zebrafish induced by PNSL.

3.2. Protective Effect of SC on Zebrafish Locomotor Activity. The behavior analyzer EthoVision was used to track the movement of zebrafish. As shown in Figures 2(a)–2(c), the Moving speed (MS), moving distance (MD), and travel frequency (TF) of PNSL group were significantly lower than those of the CON, while for SC treatment group, these parameters were close to the DMSO. The results showed that different concentrations of SC increased MD by 109.46%, 79.91%, and 47.27%, respectively, with partial significance ($p < 0.001 - 0.01$). TF for SC-H, SC-M, and SC-L was 371.43%, 254.54%, and 159.62%, respectively. Also, the hot plot revealed zebrafish activity degree (Figure 2(d)). These results with significant differences demonstrated that SC can reverse OP.

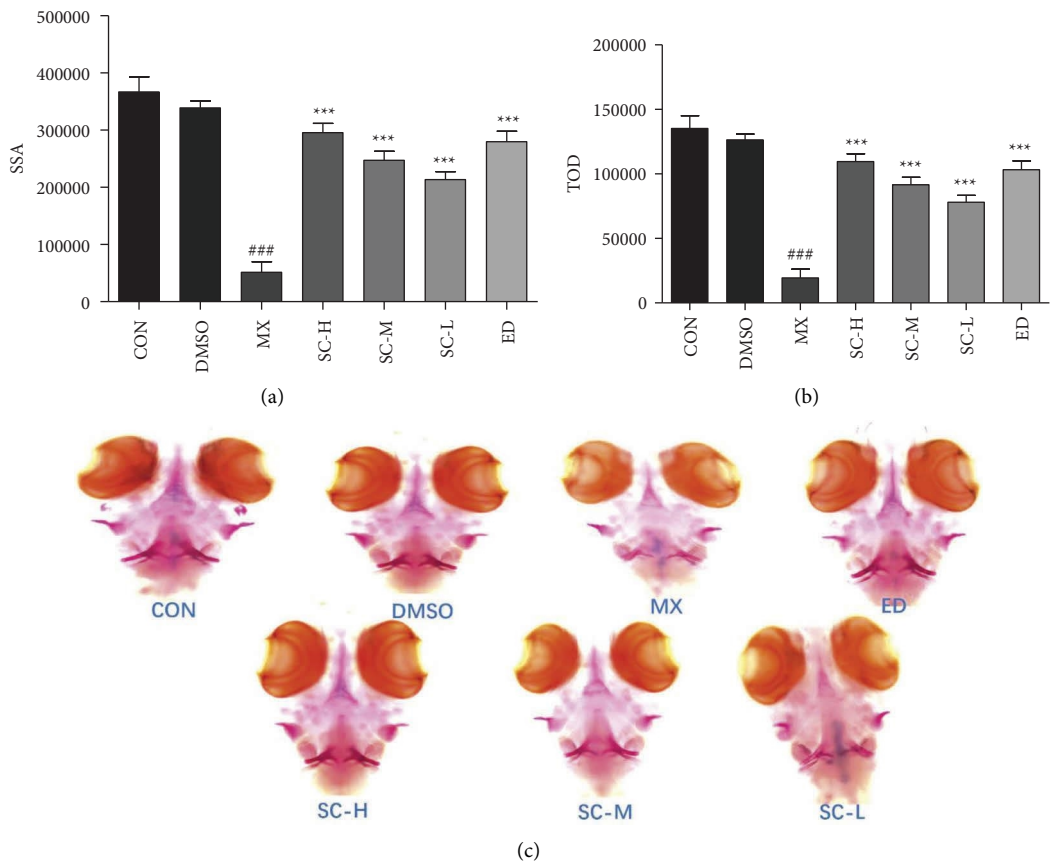

Figure 1: The effect of SC on mineralization in zebrafish larvae ($n = 15$). (a) Skeleton stained area (SSA). (b) Total optical density (TOD). (c) Ventral view of alizarin red stained zebrafish skull (×100). CON, blank E_3 medium; DMSO, 0.5% DMSO; MX, 25 μM PNSL; ED, 15 μM ED + 25 μM PNSL; SC-H, 10.0 μg/mL SC + 25 μM PNSL; SC-M, 1.0 μg/mL SC + 25 μM PNSL; SC-L, 0.1 μg/mL SC + 25 μM PNSL. $^{###}p < 0.001$ compared with DMSO. $^{***}p < 0.001$ compared with MX.

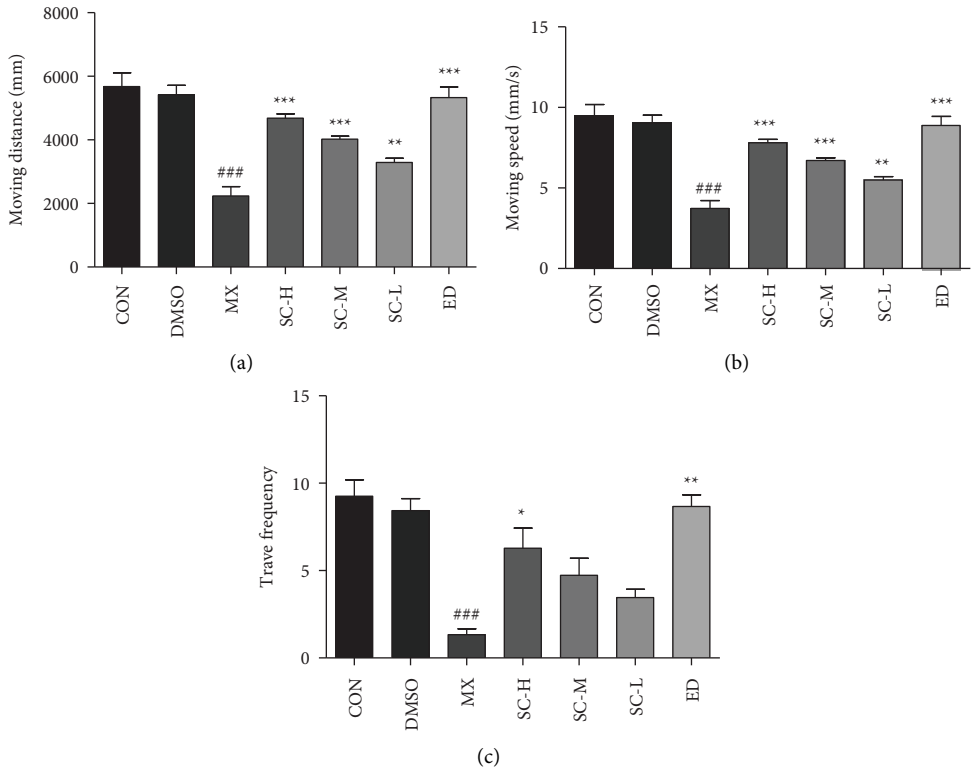

Figure 2: Continued.

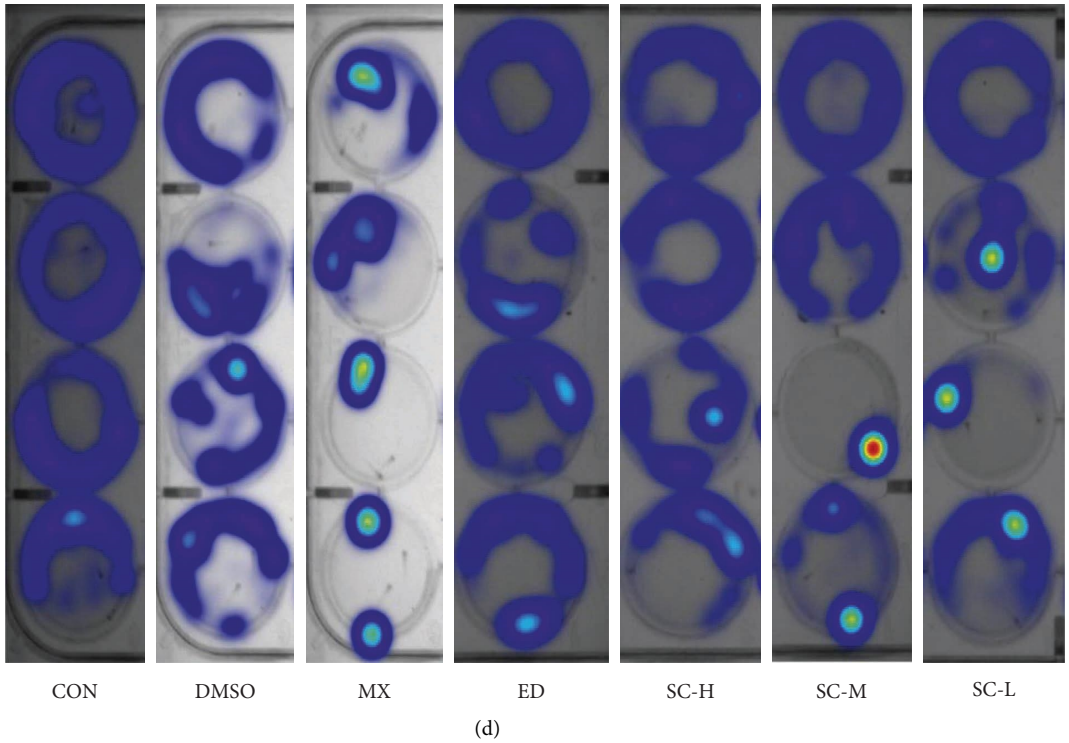

Figure 2: Effect of SC on zebrafish locomotor activity ($n = 15$). (a) Moving distance (MD); (b) moving speed (MS); (c) travel frequency (TF); (d) hot plot. CON, blank E_3 medium; DMSO, 0.5% DMSO; MX, 25 μM PNSL; ED, 15 μM ED + 25 μM PNSL; SC-H, 10.0 μg/mL SC + 25 μM PNSL; SC-M, 1.0 μg/mL SC + 25 μM PNSL; SC-L, 0.1 μg/mL SC + 25 μM PNSL. $^{###}p < 0.001$ compared with DMSO. $^{*}p < 0.05$ compared with MX. $^{**}p < 0.01$ compared with MX. $^{***}p < 0.001$ compared with MX.

3.3. Main Components of SC and Treatment Targets of OP. 68 active components in SC were obtained through retrieving the TCMSP database, and after screening by "OB ≥20% and DL ≥0.1," 33 chemical bioactive components of SC were obtained (Table 1). 609 corresponding genes were collected by UniProt gene annotation simultaneously.

Through PharmGkb, TTD, DrugBank, GeneCards, and OMIM, 3150 OP-related targets were collected (Figure 3(a)). By matching the target of SC with OP-related targets, 72 common genes were derived, which were potential targets of SC in treating OP (Table 2, Figure 3(b)).

3.4. Construction of PPI Network and Acquisition of Core Genes. The 72 obtained intersecting genes were imported into the STRING database to obtain the interaction relationships between them and save the data as a file in TSV format (Figure 4). Secondly, we visualized the PPI network by importing it into the Cytoscape software and identified 10 core genes using plug in-CytoHubba of Cytoscape software, namely, MAPK1, VEGFA, MMP9, AKT1, AR, IL6, CALM3, TP53, EGFR, and CAT (Figure 5).

3.5. GO and KEGG Enrichment Analysis. In order to further elucidate the potential relationship between common genes and the mechanism by which the SC might remedy OP, R language was applied to perform GO and KEGG analysis. A total of 2049 GO terms were collected, of which 1892 are biological process (BP) entries, 106 molecular function (MF) entries, and 51 cellular component (CC) entries. As shown in Figure 6, the top 10 BP terms were principally relevant to the response to steroid hormone, response to metal ion, cellular response to chemical stress, response to drug, gland development, regulation of DNA-binding transcription factor activity, response to oxygen levels, reactive oxygen species metabolic process, muscle cell proliferation, and rhythmic process. The MF analysis indicated that these gene targets were mainly related to nuclear receptor activity, ligand-activated transcription factor activity, cytokine receptor binding, steroid hormone receptor activity, DNA-binding transcription factor binding, and RNA polymerase II-specific DNA-binding transcription factor binding. The CC entries were mainly related to membrane microdomain, membrane raft, membrane region, caveolae, and plasma membrane raft.

Moreover, a total of 139 signaling pathways were yielded through KEGG enrichment analysis, including Bladder cancer, Lipid and atherosclerosis, Kaposi sarcoma-associated herpesvirus infection, AGE-RAGE signaling pathway, IL-17 signaling pathway, Hepatitis C, Human cytomegalovirus infection, Estrogen signaling pathway, Breast cancer, and TNF signaling pathway. As shown in Figure 7, we visualized the top 30 filtered pathways using bubble plot and bar diagram. Among these signaling pathways, AGE-RAGE signaling pathway was chosen to further research (Figure 8); in the picture, red nodes mean

Table 1: All bioactive components of Spatholobi Caulis.

Molecule ID	Component	Molecular weight	Oral bioavailability	Drug like
MOL000295	Alexandrin	576.95	20.63	0.63
MOL000296	Hederagenin	414.79	36.91	0.75
MOL000033	(24S)-24-Propylcholesta-5-ene-3beta-ol	428.82	36.23	0.78
MOL000358	Beta-sitosterol	414.79	36.91	0.75
MOL000392	Formononetin	268.28	69.67	0.21
MOL000417	Calycosin	284.28	47.75	0.24
MOL000436	lopac-I-3766	256.27	87.51	0.15
MOL000449	Stigmasterol	412.77	43.83	0.76
MOL000460	(Z)-1-(2, 4-Dihydroxyphenyl)-3-(3, 4-dihydroxyphenyl) prop-2-en-1-one	272.27	83.78	0.17
MOL000461	3,7-Dihydroxy-6-methoxy-dihydroflavonol	302.3	43.8	0.26
MOL000463	16844-71-6	428.82	27.34	0.76
MOL000467	Castanin	298.31	23.54	0.27
MOL000468	8-o-Methylreyusi	298.31	70.32	0.27
MOL000469	3-Hydroxystigmast-5-en-7-one	428.77	40.93	0.78
MOL000470	8-C-α-L-Arabinosylluteolin	418.38	35.54	0.66
MOL000471	Aloe-emodin	270.25	83.38	0.24
MOL000472	Emodin	270.25	24.4	0.24
MOL000474	(-)-Epoxycaryophyllene	220.39	35.94	0.13
MOL000476	Physcion	284.28	22.29	0.27
MOL000483	(Z)-3-(4-Hydroxy-3-methoxy-phenyl)-N-[2-(4hydroxyphenyl)ethyl]acrylamide	313.38	118.35	0.26
MOL000490	Petunidin	317.29	30.05	0.31
MOL000492	(+)-Catechin	290.29	54.83	0.24
MOL000493	Campesterol	400.76	37.58	0.71
MOL000497	Licochalcone a	338.43	40.79	0.29
MOL000498	Isoorientin	448.41	23.3	0.76
MOL000500	Vestitol	272.32	74.66	0.21
MOL000501	Consume close grain	302.3	68.12	0.27
MOL000502	Cajinin	300.28	68.8	0.27
MOL000503	Medicagol	296.24	57.49	0.6
MOL000504	Kadsurin	456.58	25.22	0.84
MOL000507	Psi-baptigenin	282.26	70.12	0.31
MOL000510	Olmelin	284.28	25.21	0.24
MOL000006	Luteolin	286.25	36.16	0.25

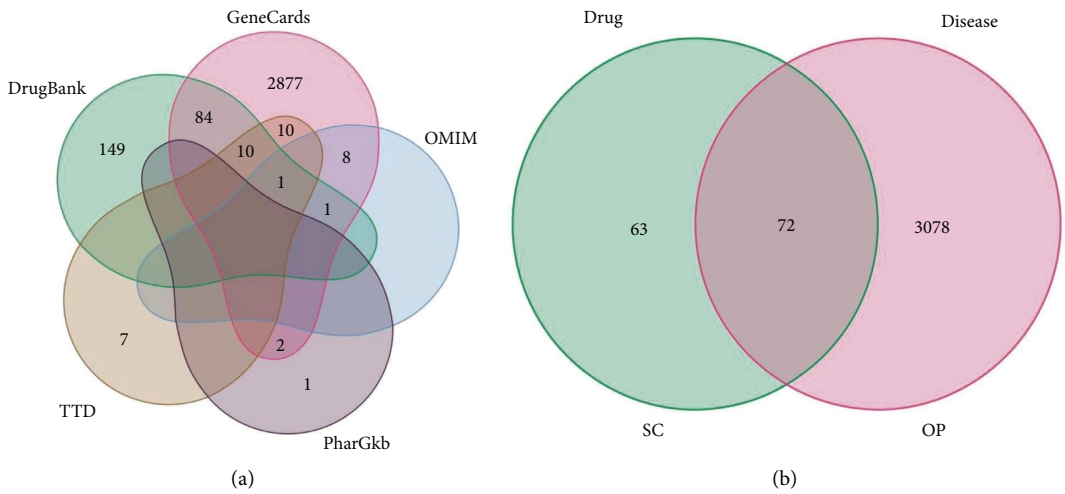

Figure 3: Venn diagram of OP-related disease targets and overlapping targets between OP-related and SC-related targets. (a) OP-related disease targets; (b) overlapping targets between OP-related and SC-related targets.

Table 2: Overlapping targets of drug potential targets and disease-related targets.

Target name	Symbol
RAC-alpha serine/threonine-protein kinase	AKT1
Cellular tumor antigen p53	TP53
Interleukin-6	IL6
Transcription factor AP-1	JUN
Mitogen-activated protein kinase 1	MAPK1
Vascular endothelial growth factor A	VEGFA
Tumor necrosis factor	TNF
Myc proto-oncogene protein	MYC
Signal transducer and activator of transcription 3	STAT3
Epidermal growth factor receptor	EGFR
Caspase-3	CASP3
Pro-epidermal growth factor	EGF
Matrix metalloproteinase-9	MMP9
Prostaglandin G/H synthase 2	PTGS2
Estrogen receptor	ESR1
G1/S-specific cyclin-D1	CCND1
Caspase-8	CASP8
Peroxisome proliferator activated receptor gamma	PPARG
Interleukin-1 beta	IL1B
Catalase	CAT
72 kDa type IV collagenase	MMP2
Interleukin-4	IL4
Androgen receptor	AR
Intercellular adhesion molecule 1	ICAM1
Granulocyte-macrophage colony-stimulating factor	CSF2
Heme oxygenase 1	HMOX1
Interferon gamma	IFNG
Progesterone receptor	PGR
Cell division protein kinase 4	CDK4
Interstitial collagenase	MMP1
Induced myeloid leukemia cell differentiation protein Mcl-1	MCL1
Nitric oxide synthase, inducible	NOS2
Urokinase-type plasminogen activator	PLAU
Amyloid beta A4 protein	APP
Estrogen receptor beta	ESR2
Glutathione S-transferase P	XIAP
CD40 ligand	CD40LG
Retinoblastoma-associated protein	RB1

Table 2: Continued.

Target name	Symbol
Nuclear factor erythroid 2-related factor 2	NFE2L2
Cytochrome P450 1A1	CYP1A1
Caspase-7	CASP7
Nuclear receptor coactivator 2	NCOA2
Nuclear receptor coactivator 1	NCOA1
Baculoviral IAP repeat-containing protein 5	BIRC5
DNA topoisomerase 2-alpha	TOP2A
Mu-type opioid receptor	OPRM1
Protein kinase C delta type	PRKCD
Tyrosine-protein kinase BTK	BTK
DNA topoisomerase 1	TOP1
Retinoic acid receptor RXR-alpha	RXRA
Calmodulin	CALM3
Aldose reductase	AKR1B1
Interleukin-2	IL2RB
Dipeptidyl peptidase IV	DPP4
Actin, aortic smooth muscle	ACTA2
Insulin receptor	INSR
Prostaglandin E synthase	PTGES
Sodium-dependent noradrenaline transporter	SLC6A4
Serum paraoxonase/arylesterase 1	PON1
3 Beta-hydroxysteroid dehydrogenase/Delta 5-->4-isomerase type 1	HSD3B1
Tyrosinase	TYR
Mineralocorticoid receptor	NR3C2
3 beta-hydroxysteroid dehydrogenase/Delta 5-->4-isomerase type 2	HSD3B2
Trypsin-3	PRSS3
Alcohol dehydrogenase 1B	ADH1B
Alcohol dehydrogenase 1C	ADH1C
Sodium-dependent dopamine transporter	SLC6A3
Carbonic anhydrase II	CA2
Glycogen phosphorylase, muscle form	PYGM
Gamma-aminobutyric acid receptor subunit alpha-1	GABRA1
Sodium channel protein type 5 subunit alpha	SCN5A
Eukaryotic translation initiation factor 6	EIF6

Figure 4: Protein-protein interaction network (PPI). The PPI network from STRING was further analyzed using Cytoscape software (the line between two nodes indicates the interaction; the darker the color of the node, the more the relationship between them).

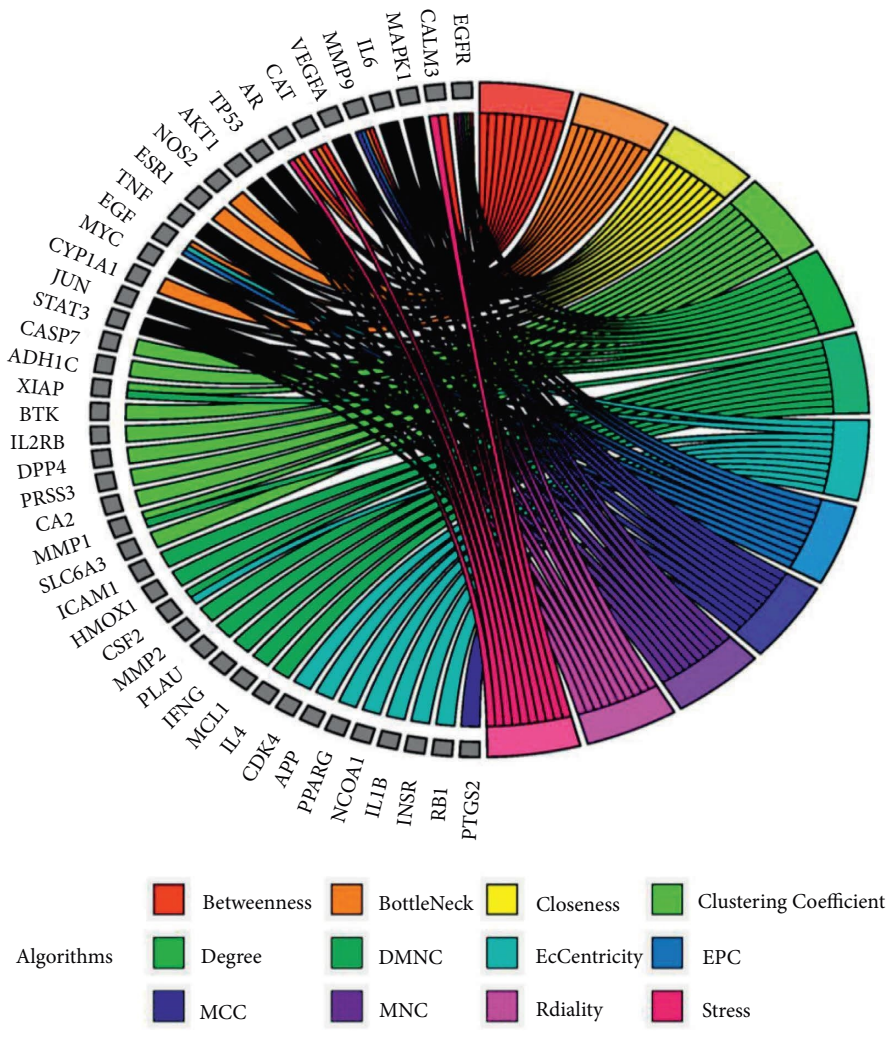

(a)

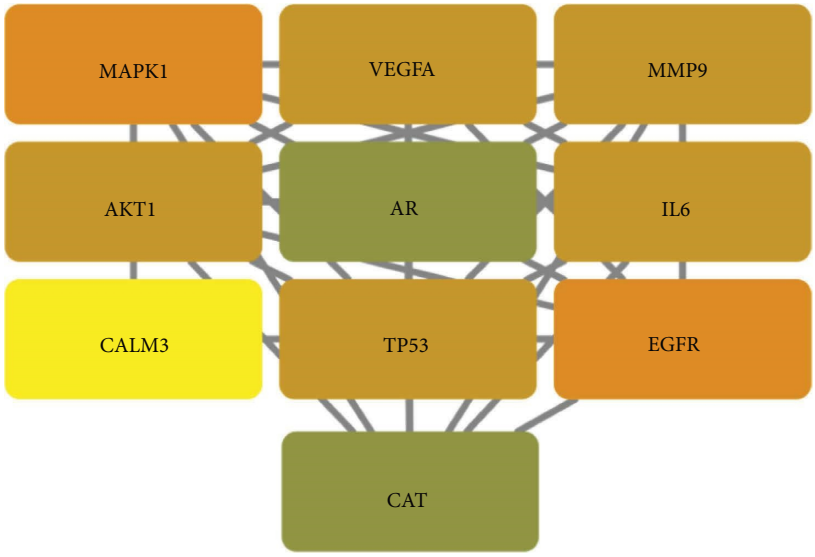

(b)

Figure 5: Analysis of 10 main core target genes. (a) Chord diagram of the corresponding relationship between the top 10 genes and 12 cytohubba algorithms. (b) The top 10 hub genes.

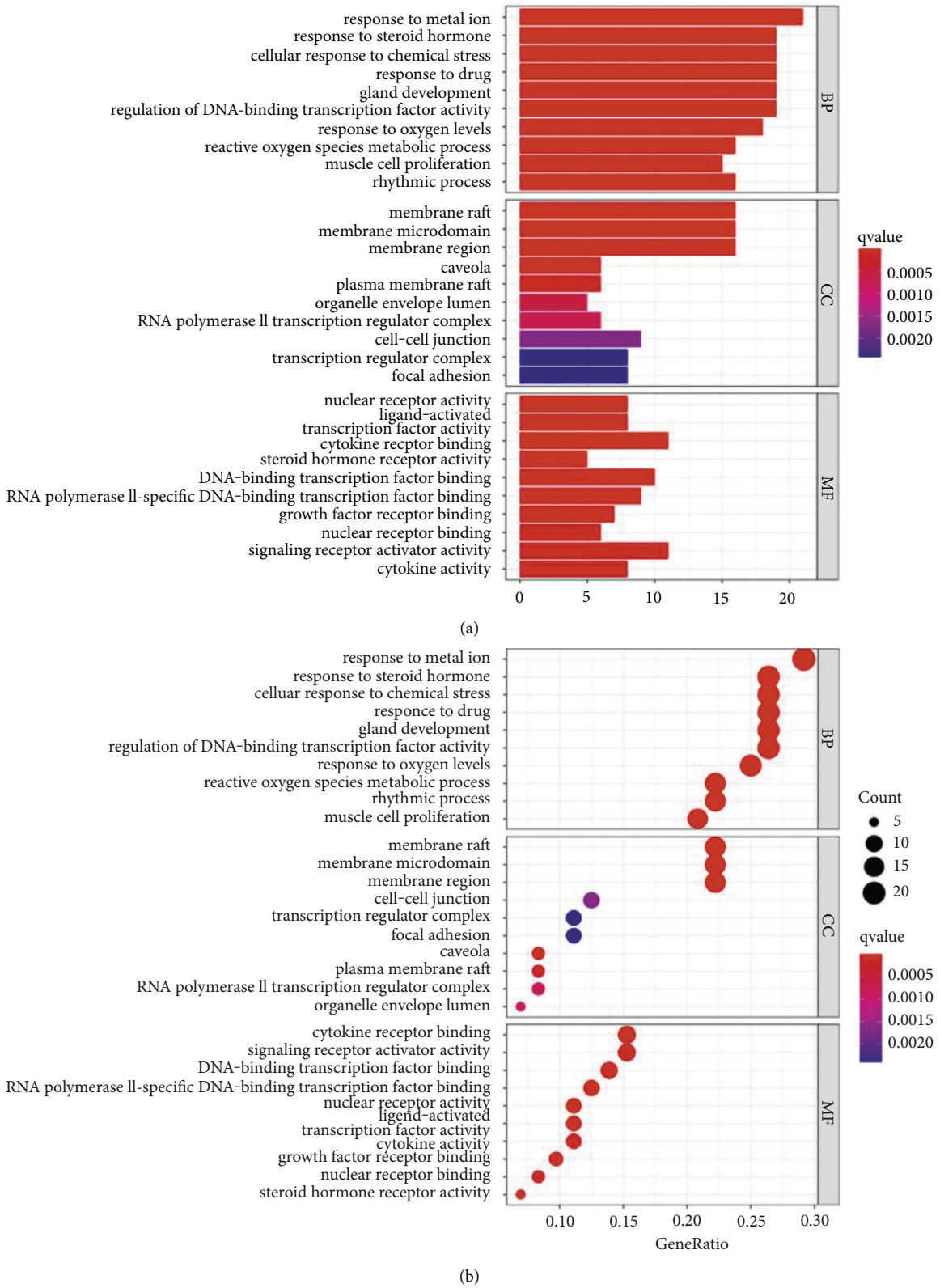

Figure 6: GO function analysis. (a) Barplot; (b) barble, including BP, MF, and CC. The y-axis shows top 10 significantly enriched BP, CC, and MF categories, and the x-axis displays the number of enrichment genes of these terms ($p < 0.05$). The color of each bar represents the adjusted p value, and the length represents the number of enriched genes.

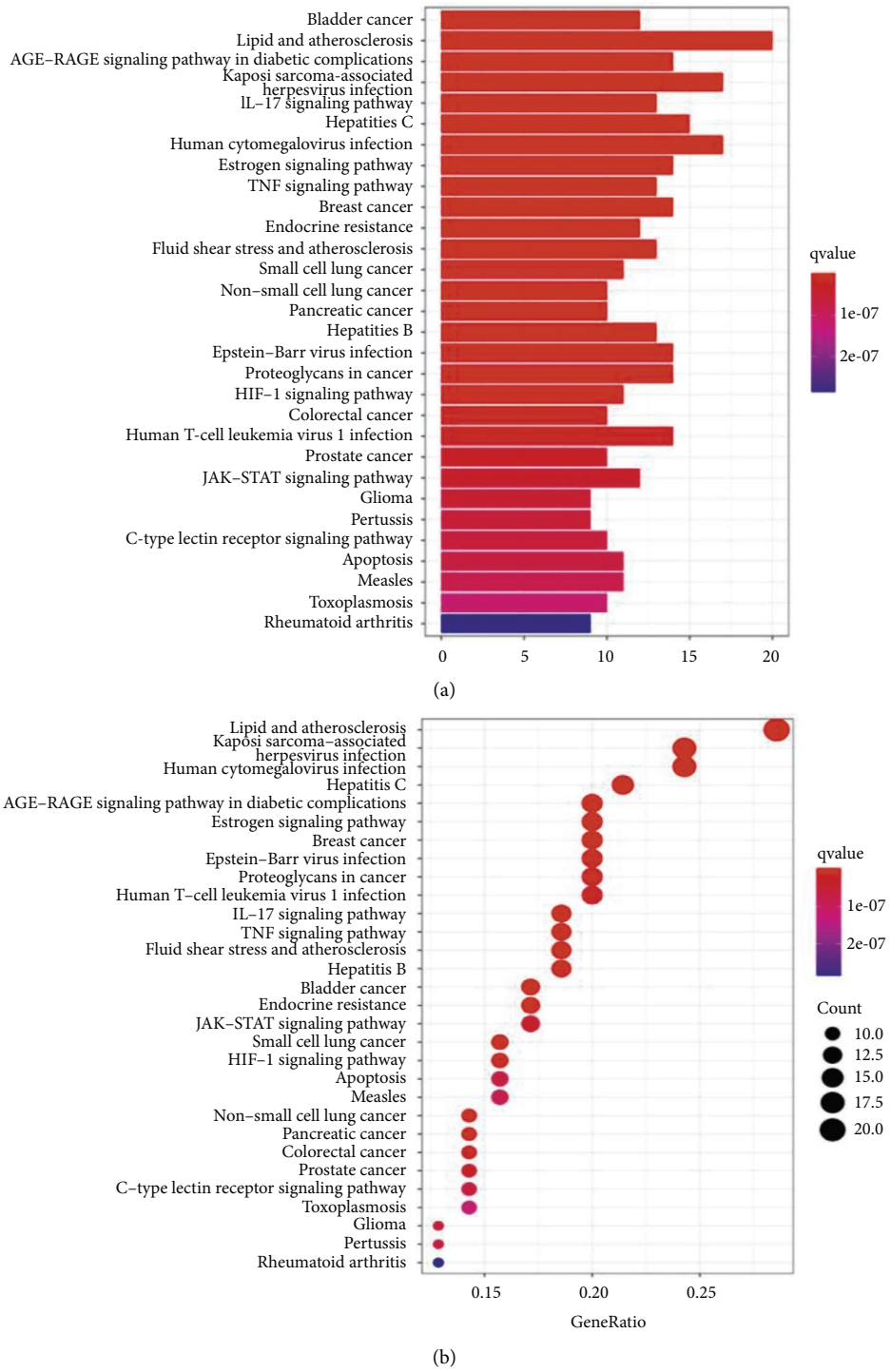

Figure 7: KEGG pathway analysis. (a) Barplot; (b) barble, including BP, MF, and CC. The y-axis shows top 30 significantly enriched KEGG pathways, and the x-axis displays the number of enrichment genes of these terms ($p < 0.05$). The color of each bar represents the adjusted p value, and the length represents the number of enriched genes.

the genes in the road map present in the SC network in this study. Finally, a ternary network of "active ingredients—potential targets-signaling pathways" was drawn successfully (Figure 9).

3.6. Molecular Docking Results. 10 core genes (MAPK1, VEGFA, MMP9, AKT1, AR, IL6, CALM3, TP53, EGFR, and CAT) were identified using 12 algorithms in CytoHubba. After KEGG enrichment analysis, we searched for OP in the

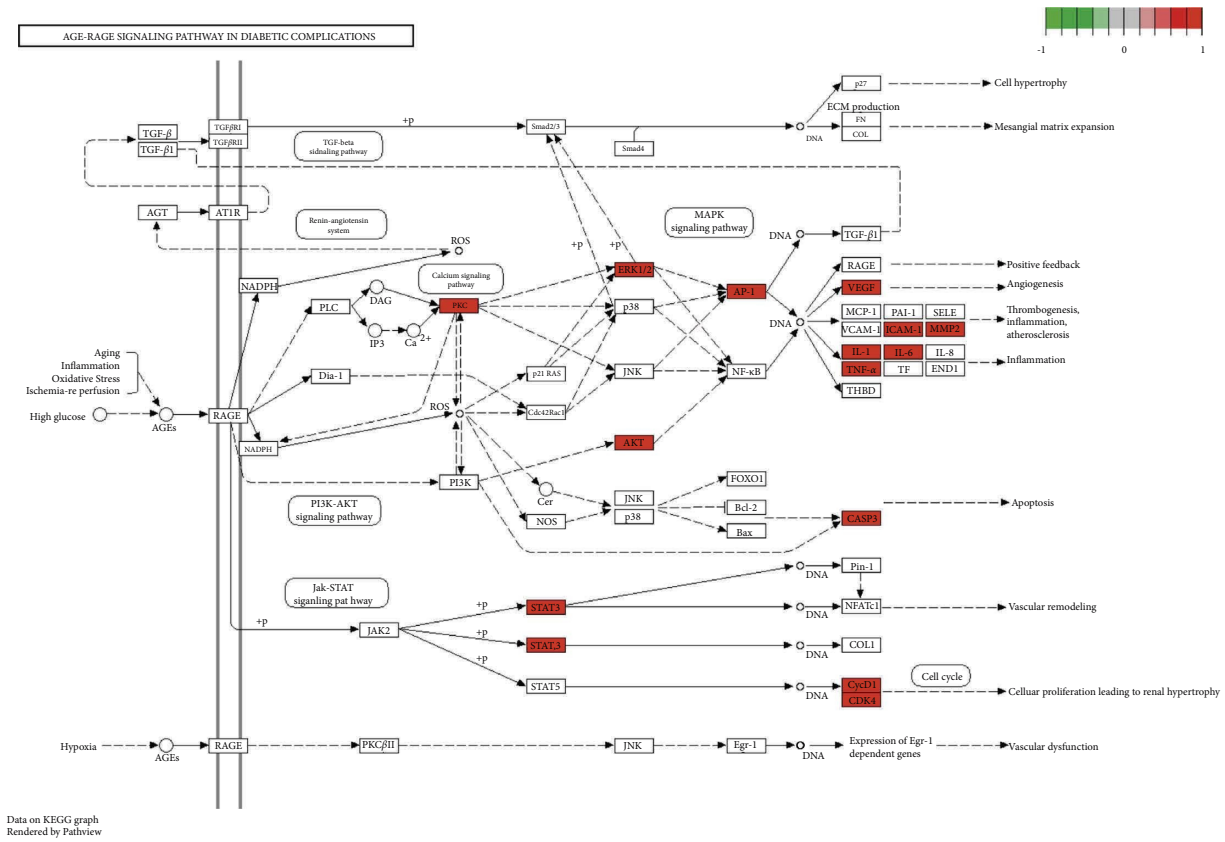

FIGURE 8: The main nodes of AGE-RAGE signaling pathway. Red nodes mean the genes in the road map present in the SC network in this study.

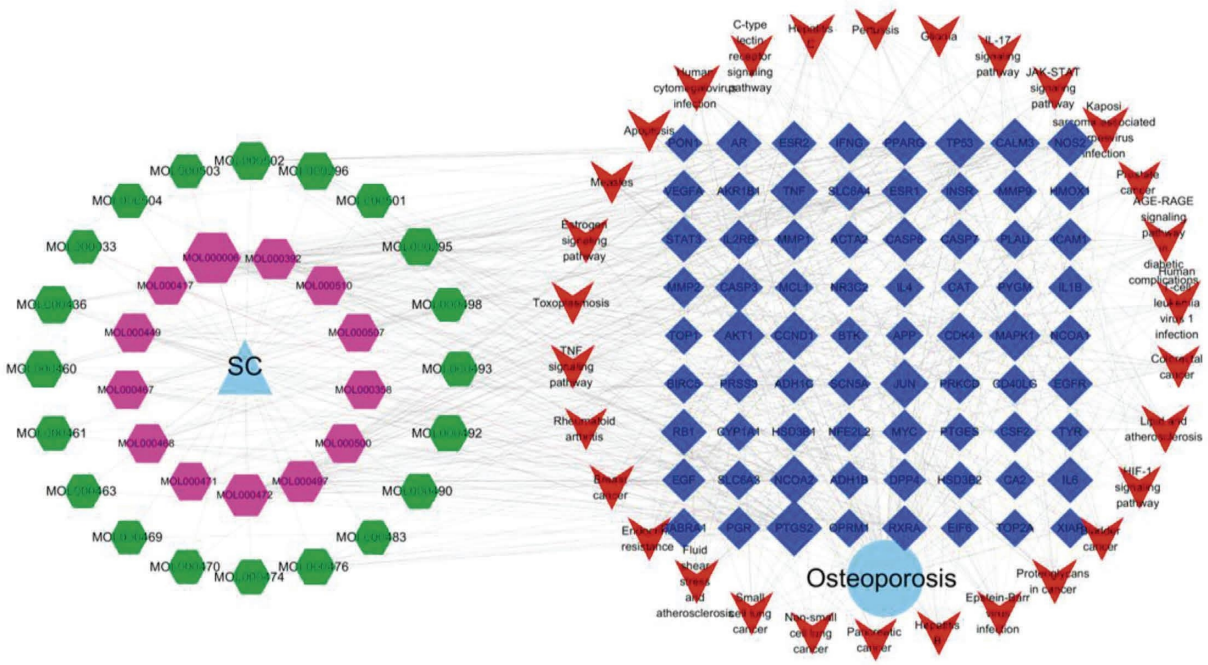

FIGURE 9: The network of "drug-active ingredients-target genes -pathways -disease." Yellow triangle represents drug; hexagon node represents the ingredients of SC. Blue square node represents potential treatment targets; red *V* node represents potential OP-related pathways; light blue node represents OP.

Table 3: Docking energy and interacting residues between receptors and ligands.

Receptor	Ligand	Affinity (kcal/mol)	Residues
AKT1	Aloe-emodin	−6.6	LEU-52, GLN47, GLU40
	Emodin	−6.8	TRP-11, HIS-13, GLU-91
	Formononetin	−7	TRP-11, HIS-13, GLU-91
	Licochalcone a	−6	TRP-11, HIS-13, GLU-95
	Luteolin	−8.4	ARG-23, LYS-14, ARG-86
	lopac-I-3766	−6.3	LYS-8, GLU-95, HIS-89
IL6	Aloe-emodin	−6.9	ASN-63, THR-143
	Emodin	−6.9	ASN-144, THR-143, LEU-147
	Formononetin	−8.8	GLN-175, ARG-182, ARG-179
	Licochalcone a	−6.6	ARG-182, GLN-175
	Luteolin	−7.1	ASP-34, ARG-179
	lopac-I-3766	−8.6	ARG-104, GLN-156, ASP-160, THR-43
MAPK1	Aloe-emodin	−7.8	ASP-111, GLU-71, LYS-54
	Emodin	−9.1	ARG-70, ARG-172, ARG-148
	Formononetin	−8.1	ASN-154, LYS-54
	Licochalcone a	−7.3	ARG-67
	Luteolin	−8.6	LYS-114, LYS-54
	lopac-I-3766	−7.4	GLN-105, LEU-156
MMP9	Aloe-emodin	−7.6	GLU-47, ARG-51
	Emodin	−7.8	ASN-38, ARG-95, ARG-51
	Formononetin	−7.8	THR-426, LEU-188
	Licochalcone a	−6.5	ARG-143
	Luteolin	−8	GLU-47, ASN-38
	lopac-I-3766	−7.3	HIS-401, THR-426
VEGFA	Aloe-emodin	−6.3	ASP-34
	Emodin	−6.5	ASP-34, ILE-46
	Formononetin	−5.9	SER-50
	Licochalcone a	−5.8	GLN-37
	Luteolin	−6.2	ASP-34
	lopac-I-3766	−7.7	GLN-22, ASN-62

Table 4: Bonding position and H-bond interaction between receptors and ligands.

Receptor	Ligand	Position	Receptor	Interaction	Distance
AKT1	Aloe-emodin	O (5)	GLN-47	H-donor	2.5
		O (3)	GLU-40	H-acceptor	3.4
		O (1)	LEU-52	H-donor	2.6
	Emodin	O (5)	GLU-91	H-donor	3.3
		O (3)	HIS-13	H-acceptor	3.4
		6-ring	TRP-11	H-acceptor	3.7
	Formononetin	6-ring	TRP-11	H-acceptor	3.5
		O (4)	GLU-91	H-donor	3
		O (2)	HIS-13	H-acceptor	3
	Licochalcone a	O (1)	GLU-95	H-donor	3.1
		O (2)	HIS-13	H-acceptor	3.2
		O (3)	TRP-11	Pi-H	3.8
	luteolin	O (6)	ARG-23	H-acceptor	2.1
		O (4)	LYS-14	H-acceptor	2.1
		O (4)	ARG-86	H-acceptor	2.5
		O (2)	LYS-14	H-acceptor	2.3
	lopac-I-3766	O (4)	LYS-8	H-acceptor	2
		6-ring	GLU-95	Pi-H	3.5
		O (1)	HIS-89	H-donor	3.4

Table 4: Continued.

Receptor	Ligand	Position	Receptor	Interaction	Distance
IL6	Aloe-emodin	O (1)	ASN-63	H-donor	3.3
		O (3)	THR-143	H-acceptor	3.3
		O (5)	THR-143	H-acceptor	3.6
	Emodin	O (3)	ASN-144	H-acceptor	3.1
		O (3)	THR-143	H-acceptor	3.3
	Formononetin	6-ring	GLN-175	H-acceptor	3
		O (1)	ARG-182	H-acceptor	2.3
		O (1)	ARG-182	H-acceptor	1.8
	Licochalcone a	O (1)	ARG-179	H-acceptor	2.2
		O (1)	ARG-182	H-acceptor	2.5
		6-ring	GLN-175	H-donor	2.2
	Luteolin	O (5)	ASP-34	H-donor	3.3
		O (1)	ARG-179	H-acceptor	2.8
		O (1)	ARG-179	H-acceptor	2.7
	lopac-I-3766	O (4)	ARG-104	H-acceptor	2.3
		O (4)	ARG-104	H-acceptor	2.7
		O (1)	THR-43	H-acceptor	2.2
		O (1)	ASP-160	H-donor	2.2
MAPK1	Aloe-emodin	O (4)	GLU-71	H-donor	3.6
		O (4)	LYS-54	H-acceptor	2.2
		6-ring	ASP-111	Pi-H	3.3
	Emodin	O (1)	ARG-70	H-acceptor	2.8
		O (2)	ARG-172	H-acceptor	2.3
		O (2)	ARG-148	H-acceptor	2
	Formononetin	O (4)	ASN-154	H-donor	2.6
		O (2)	LYS-54	H-acceptor	2
	Licochalcone a	O (1)	ARG-67	H-acceptor	1.8
		O (1)	ARG-67	H-acceptor	3
	Luteolin	O (6)	LYS-114	H-acceptor	2.6
		O (2)	LYS-54	H-donor	2.3
	lopac-I-3766	O (1)	GLN-105	H-donor	3.7
		O (2)	LEU-156	H-acceptor	3.6
MMP9	Aloe-emodin	O (5)	GLU-47	H-donor	2.6
		O (5)	ARG-51	H-acceptor	2.2
		O (5)	ARG-51	H-acceptor	3.4
	Emodin	O (5)	ASN-38	H-donor	3.6
		6-ring	ARG-51	H-acceptor	2.7
	Formononetin	O (1)	THR-426	H-acceptor	2.5
	Licochalcone a	O (2)	ARG-143	H-acceptor	2.1
		O (2)	ARG-143	H-acceptor	2.6
	Luteolin	O (1)	ASN-38	H-donor	2.7
		O (5)	GLU-47	H-donor	2
		O (6)	GLU-47	H-donor	2.7
	lopac-I-3766	O (4)	THR-426	H-acceptor	2.6
VEGFA	Aloe-emodin	O (5)	ASP-34	H-donor	2.1
		O (5)	ASP-34	H-donor	2.6
	Emodin	O (4)	ASP-34	H-donor	3.3
		O (5)	ILE-46	H-donor	3.6
	Formononetin	O (1)	SER-50	H-acceptor	3.6
		O (1)	SER-50	H-donor	2.4
	Licochalcone a	O (1)	GLN-37	H-donor	2.6
	Luteolin	O (5)	ASP-34	H-donor	2.1
		O (5)	ASP-34	H-donor	2.2
	lopac-I-3766	O (2)	GLN-22	H-acceptor	2.5
		O (3)	GLN-22	H-donor	2.3
		O (1)	ASN-62	H-acceptor	2

KEGG pathway database and found that there are mainly two pathways directly related to OP and related diseases, including AGE-RAGE signaling pathway and Estrogen signaling pathway. Subsequently, we found that five of the top 10 hub genes (MAPK1, VEGFA, MMP9, AKT1, and IL6) were enriched in AGE-RAGE signaling pathway. Aloe-

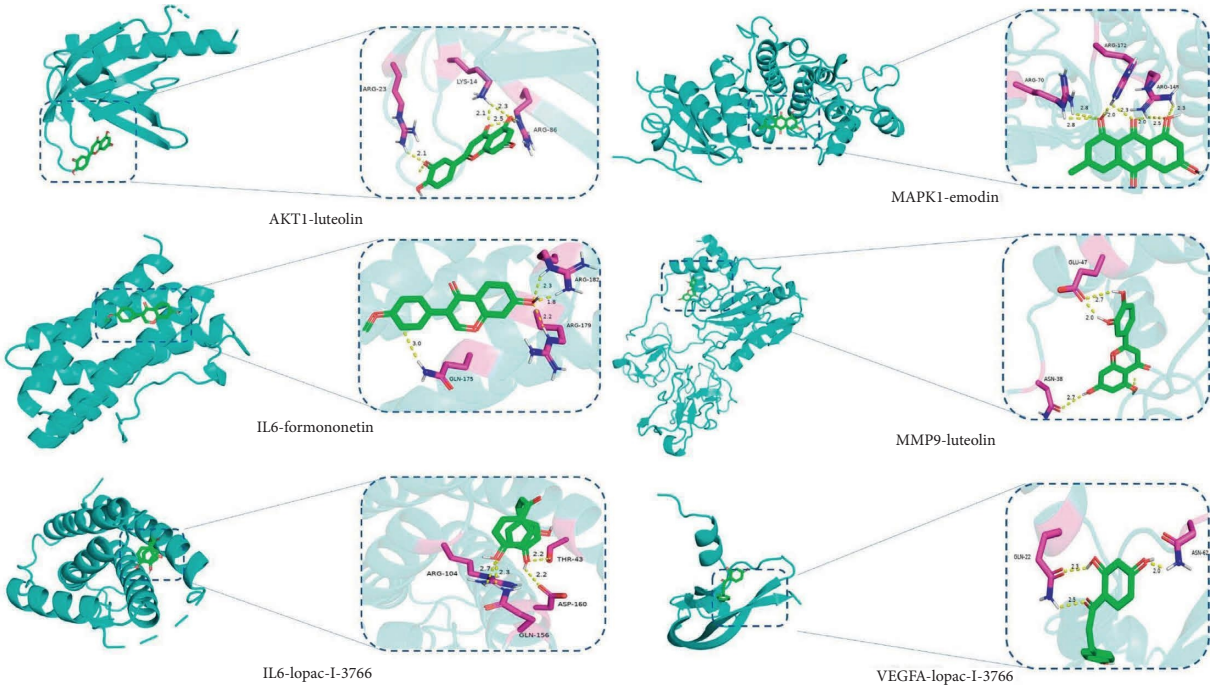

Figure 10: Docking graph between bioactive components and core genes.

emodin, emodin, formononetin, licochalcone A, luteolin, and lopac-I-3766 were selected as the top active components for molecular docking with MAPK1, VEGFA, MMP9, AKT1, and IL6 in turn. "The binding energy between drug component ligands and target receptors is an important indicator to evaluate the binding capacity. It is generally considered that the docking affinity is stronger when the binding energy is less than—5.0 kcal/mol, and the docking activity is extremely strong when the binding energy is less than—7.0 kcal/mol." From the docking results (Tables 3 and 4), it was found that AKT1-luteolin, IL6-formononetin, IL6-lopac-I-3766, MAPK1-emodin, MMP9-luteolin, and VEGFA- lopac-I-3766 had the lower binding energies. It is speculated that SC mainly exerted anti-OP effect through above molecular docking process. Eventually, we chose above protein targets and active component with the lowest docking affinity for visualization (Figure 10).

4. Discussion

OP is a metabolic disease caused by various factors, such as age, endocrine, viral infection, and a variety of cytokines. Given that the multitarget and multipathway pharmacological properties of TCM make it more suitable for the treatment of OP, SC is a widely used traditional medicine for promoting blood circulation to remove blood stasis and nourishing blood. Modern pharmacological studies revealed that SC exerted anti-OP through inhibition of osteoclastogenesis and stimulation of chondrogenesis. However, the underlying mechanism remains unclear. The aim is to clarify the potential mechanisms of SC for OP treatment integrated zebrafish model and network pharmacology.

Zebrafish is an ideal animal model in vivo for studying bone deformations for the high similarity of the structure and genetics of bone with human beings [74]. In the present study, we established the zebrafish OP model induced by PNSL to evaluate the effects of SC on the bone formation and examined the bone mineralization by Alizarin red staining, which is a vital dye staining, and the biological mineralization process of zebrafish can be observed directly. Our results indicated that PNSL exposure inhibited osteogenic differentiation and bone mineralization in zebrafish larvae ($p < 0.05$; Figures 1(a) and 1(b)). Compared with DMSO group, treatment with PNSL at 25 μmol/L caused an apparent decrease in the SSA and TOD with values of 51423.33 and 19405.03, respectively, which corresponded to the ventral view of Alizarin Red stained zebrafish skull, as shown in Figure 1(c). After the intervention of SC, TOD and SSA were increased to 295764.70 and 109542.50 at 10 mg/mL, respectively (Figures 1(a) and 1(b)). Besides, SC increased MD by 131.50%, 85.34%, and 69.60%, with partial significance ($p < 0.001 - 0.01$). TF for SC-H, SC-M, and SC-L was 371.43%, 254.54%, and 159.62% (Figures 2(a)–2(c)). Also, the hot plot revealed zebrafish activity degree (Figure 2(d)). These results demonstrated that SC played a positive effect on the function of osteoblastic differentiation and mineralization in zebrafish larvae.

Behavioral changes of zebrafish have been linked to chemical exposure [75, 76]. The behavior analyzer EthoVision XT made it possible to examine numerous motor events and facilitated the quantitative analysis of behavior [77]. The behavioral change of zebrafish is an essential indicator to assess the anti-OP effect of SC. The MD and TF in PNSL group further supported that the construction of

osteoporosis model was successful. MD for SC was 60.32%–131.50%, 71.59%–85.34%, and 47.63%–69.60%, respectively. These results with significant differences demonstrated that SC could improve dyskinesia of zebrafish to some extent.

By evaluating the pharmacokinetic characteristics of the chemical ingredients in SC, we identified 33 bioactive components and determined 72 potential therapeutic targets of OP. These common targets of SC were related to the regulation of diverse biological activities, including response to steroid hormone, response to metal ion, cellular response to chemical stress, response to drug, regulation of DNA-binding transcription factor activity, response to oxygen levels, and muscle cell proliferation. These results were consistent with those of the previously reported pathological processes of OP [78–80]. Pathway enrichment analysis indicated that the targets of SC were enriched in diverse pathways implicated in OP pathology, such as AGE-RAGE, lipid and atherosclerosis, IL-17, Estrogen, and TNF signaling pathway.

In this study, 10 core genes (MAPK1, VEGFA, MMP9, AKT1, AR, IL6, CALM3, TP53, EGFR, and CAT) were identified using plug-in CytoHubba in Cytoscape. Subsequently, we found that five of the top 10 hub genes (MAPK1, VEGFA, MMP9, AKT1, and IL6) were enriched in AGE-RAGE signaling pathway. MAPK1, generally known as ERK2, is a member of mitogen-activated protein kinase family and acts as an essential regulator of cell proliferation, differentiation, inflammation, and bone metabolism. It has been demonstrated the activation of MAPK1 could promote osteoblastogenesis and bone mineralization in zebrafish larvae. VEGFA is a signal factor promoting neovascularization and increase vascular permeability. A recent research reported that VEGFA was a latent marker of endothelial dysfunction in postmenopausal osteoporosis. Moreover, through directly targeting VEGFA, MIR-16-5P mitigated the symptom of postmenopausal women with osteoporosis. MMP9 is a member of matrix metalloproteinases family, responsible for extracellular matrix degradation and cleavage of its structural components. A previous study illustrated that MMP9 exerted a crucial role in pathogenesis of osteoporosis, and the inhibitory effect on bone resorption was emerged by inhibiting the expression of MMP9. AKT1, also called Protein Kinase B, is a crucial signal transducer of PI3K/AKT signaling pathway. The phosphorylation of AKT1 modulates the expression of multiple downstream effectors including mTOR-C1 and FOXO3 proteins and then mitigates OP induced by iron overload. Based on the above analysis results, it is also speculated that SC against OP may play a role through the above process.

GO and KEGG enrichment analysis results showed that the therapeutic targets of SC for diseases mainly enriched in Bladder cancer, Lipid and atherosclerosis, AGE-RAGE signaling pathway, Kaposi sarcoma-associated herpesvirus infection, IL-17 signaling pathway, Hepatitis C, Human cytomegalovirus infection, Estrogen signaling pathway, TNF signaling pathway, and breast cancer. Studies have shown that all of these play a crucial role in the progression of OP. We searched for OP in the KEGG pathway database and found that there are mainly two pathways directly related to OP and related diseases, including AGE-RAGE signaling pathway and Estrogen signaling pathway. Subsequently, we found that five of the top 10 hub genes (MAPK1, VEGFA, MMP9, AKT1, and IL6) were enriched in AGE-RAGE signaling pathway. The AGE-RAGE signaling pathway plays a crucial role in bone remodeling process. In general, AGEs not only induce osteoclastogenesis by upregulation of RANKL mRNA, but they also affect osteoblasts by suppressing cell growth, promoting apoptosis, and downregulating differentiation, which impairs mineralization. It was reported that AGEs upregulated the expression of RAGE in human MSCs and then AGEs interacted with RAGE and increased the expression of TGF-b mRNA, which suppressed bone mineralization and destroyed bone remodeling [33]. In this study, five of the top 10 hub genes were enriched in the AGE-RAGE signaling pathway, so we speculated that the underlying mechanism of SC on OP might be mainly the inhibition of AGE-RAGE signaling pathway.

5. Conclusion

Compared with model group, SC significantly increased the SSA and TOD at 10 mg/mL and improved the locomotor activity in a dose-dependent manner ($p < 0.001$). 33 components of SC were associated with 72 OP-related genes including 10 core genes. AGE-RAGE signaling pathway was screened out as the principal pathway of SC in anti-OP. The bioactive components (Aloe-emodin, Emodin, Formononetin, Licochalcone A, Luteolin, and Lopac-I-3766) have excellent affinity to core genes (MAPK1, VEGFA, MMP9, AKT1, and IL6). *Conclusion.* SC had the hierarchical network characteristics of "multicomponents/multitargets/multifunctions/multipathways" in reversing OP, but AGE-RAGE signaling pathway may be the main regulatory mechanism. We have demonstrated the anti-OP effect of SC and revealed its underlying mechanism by adopting zebrafish model and network pharmacology. SC mainly regulated AGE-RAGE signaling pathway to exert anti-OP therapeutic effect.

Data Availability

The original contributions presented in the study are included in the article andsupplementary materials. Further inquiries can be directed to the corresponding authors.

Conflicts of Interest

The authors declare that they have no conflicts of interest.

Authors' Contributions

All authors listed have made a substantial, direct, and intellectual contribution to the work and approved it for publication. Jianpeng Xiao and Wei Shang contributed equally to this work.

Acknowledgments

The Natural Science Foundation of Jiangsu Province (No. BK20170560), the National Natural Science Foundation of China (No. 81703773), and the Science and Technology Development Plan of Traditional Chinese Medicine in Jiangsu Province (YB201990) supported this work.

References

[1] X. Y. Cai, Z. J. Zhang, J. L. Xiong, M. Yang, and Z.-T. Wang, "Experimental and molecular docking studies of estrogen-like and anti-osteoporosis activity of compounds in fructus psoraleae," *Journal of Ethnopharmacology*, vol. 276, no. 1, pp. 114044–114053, 2021.

[2] X. Y. Qin, Z. C. Niu, X. L. Han et al., "Anti-perimenopausal osteoporosis effects of erzhi formula via regulation of bone resorption through osteoclast differentiation: a network pharmacology-integrated experimental study," *Journal of Ethnopharmacology*, vol. 270, no. 01, pp. 1138–1145, 2021.

[3] H. Lee, M. H. Kim, L. Y. Choi, and W. M. Yang, "Ameliorative effects of osteo-F, a newly developed herbal formula, on osteoporosis via activation of bone formation," *Journal of Ethnopharmacology*, vol. 268, no. 1, pp. 113590–121140, 2021.

[4] C. B. Johnston and M. Dagar, "Osteoporosis in older adults," *Medical Clinics of North America*, vol. 104, no. 5, pp. 873–884, 2020.

[5] H. Liu, Y. Guo, R. Zhu et al., "Fructus ligustri lucidi preserves bone quality through induction of canonical wnt/β-catenin signaling pathway in ovariectomized rats," *Phytotherapy Research*, vol. 35, no. 1, pp. 424–441, 2021.

[6] J. Pepe, J. J. Body, P. Hadji et al., "Osteoporosis in premenopausal women: a clinical narrative review by the ects and the IOF," *Journal of Clinical Endocrinology and Metabolism*, vol. 105, no. 8, pp. 2487–2506, 2020.

[7] J. Y. Noh, Y. Yang, and H. Jung, "Molecular mechanisms and emerging therapeutics for osteoporosis," *International Journal of Molecular Sciences*, vol. 21, no. 20, pp. 7623–7722, 2020.

[8] I. R. Reid, "A broader strategy for osteoporosis interventions," *Nature Reviews Endocrinology*, vol. 16, no. 6, pp. 333–339, 2020.

[9] J. Proietto, "Obesity and bone," *F1000Research*, vol. 9, no. 1, pp. 1111–1117, 2020.

[10] C. Diéguez-Castillo, C. Jiménez-Luna, J. Prados, J. L. Martin-Ruiz, and O. Caba, "State of the art in exocrine pancreatic insufficiency," *Medicina*, vol. 56, no. 10, pp. 523–610, 2020.

[11] J. Jiang, J. Li, and X. Jia, "The antiosteoporotic activity of central-icaritin (CIT) on bone metabolism of ovariectomized rats," *Molecules*, vol. 19, no. 11, pp. 18690–18704, 2014.

[12] P. Chotiyarnwong and E. V. McCloskey, "Pathogenesis of glucocorticoid-induced osteoporosis and options for treatment," *Nature Reviews Endocrinology*, vol. 16, no. 8, pp. 437–447, 2020.

[13] R. M. Slaton, K. Boyd, and M. Iranikhah, "Romosozumab and sequential therapy in postmenopausal osteoporosis," *Sr Care Pharm*, vol. 35, no. 7, pp. 297–308, 2020.

[14] A. Munoz-Garach, B. García-Fontana, and M. Munoz-Torres, "Nutrients and dietary patterns related to osteoporosis," *Nutrients*, vol. 12, no. 7, pp. 1986–2016, 2020.

[15] S. L. Watson, B. K. Weeks, L. J. Weis, A. T. Harding, S. A. Horan, and B. R. Beck, "High-intensity resistance and impact training improves bone mineral density and physical function in postmenopausal women with osteopenia and osteoporosis: the LIFTMOR randomized controlled trial," *Journal of Bone and Mineral Research*, vol. 33, no. 2, pp. 211–220, 2018.

[16] Q. Cheng, X. Zhang, J. Jiang et al., "Postmenopausal iron overload exacerbated bone loss by promoting the degradation of type I collagen," *BioMed Research International*, vol. 2017, Article ID 1345193, 9 pages, 2017.

[17] J. Jiang, J. Li, Z. Zhang, E. Sun, L. Feng, and X. b. Jia, "Mechanism of enhanced antiosteoporosis effect of circinalicaritin by self-assembled nanomicelles in vivo with suet oil and sodium deoxycholate," *International Journal of Nanomedicine*, vol. 10, no. 1, pp. 2377–2389, 2015.

[18] B. J. Zhao, J. Wang, J. Song et al., "Beneficial effects of a flavonoid fraction of herba epimedii on bone metabolism in ovariectomized rats," *Planta Medica*, vol. 82, no. 04, pp. 322–329, 2016.

[19] Y. Mei, L. Wei, C. Chai et al., "A method to study the distribution patterns for metabolites in xylem and phloem of Spatholobi Caulis," *Molecules*, vol. 25, no. 1, pp. 167–215, 2019.

[20] H. L. Chen, J. Yang, Y. F. Fu, X. n. Meng, W. d. Zhao, and T. j. Hu, "Effect of total flavonoids of spatholobus suberectus Dunn on PCV2 induced oxidative stress in RAW264.7 cells," *BMC Complementary and Alternative Medicine*, vol. 17, no. 1, pp. 244–252, 2017.

[21] J. Chang, W. Sun, J. Zeng et al., "Establishment of an in vitro system based on AGM-S3 co-culture for screening traditional herbal medicines that stimulate hematopoiesis," *Journal of Ethnopharmacology*, vol. 240, no. 1, pp. 111938–111944, 2019.

[22] F. Peng, L. Xiong, and C. Peng, "(-)-Sativan inhibits tumor development and regulates miR-200c/PD-L1 in triple negative breast cancer cells," *Frontiers in Pharmacology*, vol. 11, no. 1, pp. 251–262, 2020.

[23] J. Jiang, S. Xiao, S. Yan, J. Zhang, and X. Xu, "The effects of sulfur fumigation processing on Panacis quinquefolii radix in chemical profile, immunoregulation and liver and kidney injury," *Journal of Ethnopharmacology*, vol. 249, no. 112377, 2020.

[24] S. Qin, K. Wei, Z. Cui et al., "Comparative genomics of spatholobus suberectus and insight into flavonoid biosynthesis," *Frontiers of Plant Science*, vol. 11, no. 1, pp. 528108–528121, 2020.

[25] Y. F. Fu, L. H. Jiang, W. D. Zhao et al., "Immunomodulatory and antioxidant effects of total flavonoids of spatholobus suberectus dunn on PCV2 infected mice," *Scientific Reports*, vol. 7, no. 1, pp. 8676–8684, 2017.

[26] S. R. Chen, A. Q. Wang, L. G. LinQiu, Y. T. Wang, and Y. Wang, "In vitro study on anti-hepatitis C virus activity of spatholobus suberectus dunn," *Molecules*, vol. 21, no. 10, pp. 1367–1383, 2016.

[27] X. Y. Liu, L. Zhang, X. W. Yang et al., "Simultaneous detection and quantification of 57 compounds in spatholobi caulis applying ultra-fast liquid chromatography with tandem mass spectrometry," *Journal of Separation Science*, vol. 43, no. 23, pp. 4247–4262, 2020.

[28] P. Tang, H. Liu, B. Lin et al., "Spatholobi caulis dispensing granule reduces deep vein thrombus burden through anti-inflammation via SIRT1 and Nrf2," *Phytomedicine*, vol. 77, no. 1, pp. 153285–153293, 2020.

[29] H. P. Zhang, D. D. Zhang, Y. Ke, and K. Bian, "The vasodilatory effects of anti-inflammatory herb medications: a comparison study of four botanical extracts," *Evidance Based Complementary Alternative Medicine*, vol. 2017, Article ID 1021284, 15 pages, 2017.

[30] S. S. Qin, Y. X. Zhu, K. H. Wei, M. J. Li, J. H. Miao, and Z. Y. Zhang, "[Study on herbal textual evolution and flavonoids and their pharmacological of spatholobi caulis]," *Zhongguo Zhongyao Zazhi*, vol. 43, no. 11, pp. 2216–2223, 2018.

[31] C. Zhang, J. Liu, X. He et al., "Caulis Spatholobi ameliorates obesity through activating brown adipose tissue and modulating the composition of gut microbiota," *International Journal of Molecular Sciences*, vol. 20, no. 20, pp. 5150–5167, 2019.

[32] N. K. Im, S. G. Lee, D. S. Lee, P. H. Park, I. S. Lee, and G. S. Jeong, "Spatholobus suberectus inhibits osteoclastogenesis and stimulates chondrogenesis," *American Journal of Chinese Medicine*, vol. 42, no. 5, pp. 1123–1138, 2014.

[33] K. Asadipooya and E. M. Uy, "Advanced glycation End products (AGEs), receptor for AGEs, diabetes, and bone: review of the literature," *Journal of the Endocrine Society*, vol. 3, no. 10, pp. 1799–1818, 2019.

[34] F. Conti, D. T. Wolosinska, and G. Pugliese, "Diabetes and bone fragility: a dangerous liaison," *Aging Clinical and Experimental Research*, vol. 25, no. S1, pp. 39–41, 2013.

[35] Z. Xiong, C. Zheng, Y. Chang, K. Liu, L. Shu, and C. Zhang, "Exploring the pharmacological mechanism of duhuo jisheng decoction in treating osteoporosis based on network pharmacology," *Evidance Based Complementary Alternative Medicine*, vol. 2021, Article ID 5510290, 21 pages, 2021.

[36] J. Han, M. Wan, Z. Ma, C. Hu, and H. Yi, "Prediction of targets of curculigoside A in osteoporosis and rheumatoid arthritis using network pharmacology and experimental verification," *Drug Design, Development and Therapy*, vol. 14, no. 1, pp. 5235–5250, 2020.

[37] W. J. Liu, Z. M. Jiang, Y. Chen et al., "Network pharmacology approach to elucidate possible action mechanisms of sinomenii caulis for treating osteoporosis," *Journal of Ethnopharmacology*, vol. 257, no. 1, pp. 112871–112880, 2020.

[38] K. Dietrich, I. A. Fiedler, A. Kurzyukova et al., "Skeletal biology and disease modeling in zebrafish," *Journal of Bone and Mineral Research*, vol. 36, no. 3, pp. 436–458, 2021.

[39] Y. Feng, C. Sun, Y. Yuan et al., "Enhanced oral bioavailability and in vivo antioxidant activity of chlorogenic acid via liposomal formulation," *International Journal of Pharmaceutics*, vol. 501, no. 1-2, pp. 342–349, 2016.

[40] I. Wibowo, N. Marlinda, F. R. Nasution et al., "Downregulation of complement genes in lipopolysaccharide-challenged zebrafish (*Danio rerio*) larvae exposed to Indonesian propolis," *Brazilian Journal of Biology*, vol. 83, no. 1, pp. 2452022–e252461, 2021.

[41] O. J. Olatunji, Y. Feng, O. O. Olatunji, J. Tang, Z. Ouyang, and Z. Su, "Cordycepin protects PC12 cells against 6-hydroxydopamine induced neurotoxicity via its antioxidant properties," *Biomedicine & Pharmacotherapy*, vol. 81, no. 1, pp. 7–14, 2016.

[42] S. Shams, S. Amlani, M. Scicluna, and R. Gerlai, "Argus: an open-source and flexible software application for automated quantification of behavior during social interaction in adult zebrafish," *Behavior Research Methods*, vol. 51, no. 2, pp. 727–746, 2019.

[43] F. Crittenden, H. R. Thomas, J. M. Parant, and C. N. Falany, "Activity suppression behavior phenotype in SULT4A1 frameshift mutant zebrafish," *Drug Metabolism & Disposition*, vol. 43, no. 7, pp. 1037–1044, 2015.

[44] Z. H. Cai, H. J. Wang, J. Jiang et al., "Elaborate the mechanism of ancient classic prescriptions (ErzhiFormula) in reversing GIOP by network pharmacology coupled with zebrafish verification," *Evidence-Based Complementary and Alternative Medicine*, vol. 2022, Article ID 7019792, 17 pages, 2022.

[45] T. J. Hamilton, J. Szaszkiewicz, J. Krook, and W. Burggren, "Analysis of the potential behavioral impact of methanol when used as a solvent: dataset from zebrafish (*Danio rerio*) behavioral research," *Data in Brief*, vol. 36, no. 1, pp. 107018–107022, 2021.

[46] M. B. Orger and G. G. de Polavieja, "Zebrafish behavior: opportunities and challenges," *Annual Review of Neuroscience*, vol. 40, no. 1, pp. 125–147, 2017.

[47] M. S. Abreu, C. Maximino, F. Banha et al., "Emotional behavior in aquatic organisms? lessons from crayfish and zebrafish," *Journal of Neuroscience Research*, vol. 98, no. 5, pp. 764–779, 2020.

[48] L. Li, "Circadian vision in zebrafish: from molecule to cell and from neural network to behavior," *Journal of Biological Rhythms*, vol. 34, no. 5, pp. 451–462, 2019.

[49] K. N. Zabegalov, T. O. Kolesnikova, S. L. Khatsko et al., "Understanding zebrafish aggressive behavior," *Behavioural Processes*, vol. 158, no. 1, pp. 200–210, 2019.

[50] A. Chandrasekhar, S. Guo, I. Masai, T. Nicolson, and C. F. Wu, "Zebrafish: from genes and neurons to circuits, behavior and disease," *Journal of Neurogenetics*, vol. 31, no. 3, pp. 59-60, 2017.

[51] L. Liu, W. Tao, W. Pan et al., "Hydroxysafflor yellow A promoted bone mineralization and inhibited bone resorption which reversed glucocorticoids-induced osteoporosis," *BioMed Research International*, vol. 2018, Article ID 6762146, 8 pages, 2018.

[52] J. Jiang, S. Xiao, X. Xu, H. Ma, C. Feng, and X. Jia, "Isomeric flavonoid aglycones derived from epimedii folium exerted different intensities in anti-osteoporosis through OPG/RANKL protein targets," *International Immunopharmacology*, vol. 62, no. 1, pp. 277–286, 2018.

[53] F. R. Bohns, Y. R. Shih, Y. J. Chuang, R. Akhtar, and P. Chen, "Influence of prednisolone and alendronate on the de novo mineralization of zebrafish caudal fin," *JBMR Plus*, vol. 5, no. 2, pp. e10435–e11051, 2021.

[54] S. Vimalraj, S. Saravanan, and R. Subramanian, "Rutin-Zn(II) complex promotes bone formation—a concise assessment in human dental pulp stem cells and zebrafish," *Chemico-Biological Interactions*, vol. 349, no. 1, pp. 109674–109680, 2021.

[55] C. C. Teerlink, M. J. Jurynec, R. Hernandez et al., "A role for the MEGF6 gene in predisposition to osteoporosis," *Annals of Human Genetics*, vol. 85, no. 2, pp. 58–72, 2021.

[56] X. Zhang, D. Wang, X. Ren, A. G. Atanasov, R. Zeng, and L. Huang, "System bioinformatic approach through molecular docking, network pharmacology and microarray data analysis to determine the molecular mechanism underlying the effects of rehmanniae radix praeparata on cardiovascular diseases," *Current Protein & Peptide Science*, vol. 20, no. 10, pp. 964–975, 2019.

[57] Y. F. Meng, W. Zhu, Y. Wu et al., "Effect of curcumin on aging retinal pigment epithelial cells," *Drug Design, Development and Therapy*, vol. 9, no. 1, pp. 5337–5344, 2015.

[58] Q. Tao, J. Du, X. Li et al., "Network pharmacology and molecular docking analysis on molecular targets and mechanisms of huashi baidu formula in the treatment of COVID-19," *Drug Development and Industrial Pharmacy*, vol. 46, no. 8, pp. 1345–1353, 2020.

[59] T. H. Liu, W. H. Chen, X. D. Chen et al., "Network pharmacology identifies the mechanisms of action of taohongsiwu

decoction against essential hypertension," *Medical Science Monitor*, vol. 26, no. 1, pp. 920682–920691, 2020.

[60] Y. Wan, L. Xu, Z. Liu et al., "Utilising network pharmacology to explore the underlying mechanism of wumei pill in treating pancreatic neoplasms," *BMC Complementary and Alternative Medicine*, vol. 19, no. 1, pp. 158–169, 2019.

[61] P. Liu, H. Xu, Y. Shi, L. Deng, and X. Chen, "Potential molecular mechanisms of plantain in the treatment of gout and hyperuricemia based on network pharmacology," *Evidance Based Complementary Alternative Medicine*, vol. 2020, Article ID 3023127, 20 pages, 2020.

[62] B. Niu, H. Zhang, C. Li et al., "Network pharmacology study on the active components of *Pterocypsela elata* and the mechanism of their effect against cerebral ischemia," *Drug Design, Development and Therapy*, vol. 13, no. 1, pp. 3009–3019, 2019.

[63] T. Fang, L. Liu, and W. Liu, "Network pharmacology-based strategy for predicting therapy targets of *Tripterygium wilfordii* on acute myeloid leukemia," *Medicine (Baltimore)*, vol. 99, no. 50, pp. 235466–e24239, 2020.

[64] S. Banerjee, P. Bhattacharjee, A. Kar, and P. K. Mukherjee, "LC-MS/MS analysis and network pharmacology of trigonella foenum-graecum—a plant from Ayurveda against hyperlipidemia and hyperglycemia with combination synergy," *Phytomedicine*, vol. 60, no. 1, pp. 152944–152956, 2019.

[65] X. Wen, S. Liu, and M. Cui, "Effect of BRCA1 on the concurrent chemoradiotherapy resistance of cervical squamous cell carcinoma based on transcriptome sequencing analysis," *BioMed Research International*, vol. 2020, Article ID 3598417, 16 pages, 2020.

[66] G. Sun, S. Yan, L. Shi et al., "Decreased expression of miR-15b in human gliomas is associated with poor prognosis," *Cancer Biotherapy and Radiopharmaceuticals*, vol. 30, no. 4, pp. 169–173, 2015.

[67] Y. Zeng, G. Lou, Y. Ren et al., "Network pharmacology-based analysis of zukamu granules for the treatment of COVID-19," *European Journal of Integrative Medicine*, vol. 42, no. 1, pp. 101282–111022, 2021.

[68] G. Wang, J. J. Wang, F. Li, and S. S. T. To, "Development and evaluation of a novel drug delivery: pluronics/SDS mixed micelle loaded with myricetin in vitro and in vivo," *Journal of Pharmaceutical Sciences*, vol. 105, no. 4, pp. 1535–1543, 2016.

[69] T. Zhao, G. Mao, R. Mao et al., "Antitumor and immunomodulatory activity of a water-soluble low molecular weight polysaccharide from schisandra chinensis (turcz.) baill," *Food and Chemical Toxicology*, vol. 55, pp. 609–616, 2013.

[70] Y. Wang, Y. Chen, Y. Wan, H. Zhang, and Z. Jiao, "Anticancer efficacy enhancement and attenuation of side effects of doxorubicin with titanium dioxide nanoparticles," *International Journal of Nanomedicine*, vol. 6, pp. 2321–2326, 2011.

[71] Q. Chen, Z. Guo, J. Zhao, and Q. Ouyang, "Comparisons of different regressions tools in measurement of antioxidant activity in green tea using near infrared spectroscopy," *Journal of Pharmaceutical and Biomedical Analysis*, vol. 60, pp. 92–97, 2012.

[72] Q. Qian, S. L. Li, E. Sun et al., "Metabolite profiles of icariin in rat plasma by ultra-fast liquid chromatography coupled to triple-quadrupole/time-of-flight mass spectrometry," *Journal of Pharmaceutical and Biomedical Analysis*, vol. 66, pp. 392–398, 2012.

[73] J. Wu, G. Li, Y. Yao, Z. Wang, W. Sun, and J. Wang, "MicroRNA-421 is a new potential diagnosis biomarker with higher sensitivity and specificity than carcinoembryonic antigen and cancer antigen 125 in gastric cancer," *Biomarkers*, vol. 20, no. 1, pp. 58–63, 2015.

[74] J. Chen, L. Zhao, and Y. Wang, "[Application of zebrafish model in multimodal identification of active constituents of traditional Chinese medicine]," *Zhongguo Zhongyao Zazhi*, vol. 45, no. 14, pp. 3387–3394, 2020.

[75] B. D. Fontana, P. R. Ziani, J. Canzian et al., "Taurine protects from pentylenetetrazole-induced behavioral and neurochemical changes in zebrafish," *Molecular Neurobiology*, vol. 56, no. 1, pp. 583–594, 2019.

[76] E. Han, K. Ho Oh, S. Park et al., "Analysis of behavioral changes in zebrafish (*Danio rerio*) larvae caused by aminoglycoside-induced damage to the lateral line and muscles," *Neurotoxicology*, vol. 78, no. 1, pp. 134–142, 2020.

[77] G. Limonta, A. Mancia, A. Benkhalqui et al., "Microplastics induce transcriptional changes, immune response and behavioral alterations in adult zebrafish," *Scientific Reports*, vol. 9, no. 1, Article ID 15775, 2019.

[78] H. Matsubayashi, H. Ishiwatari, K. Imai et al., "Steroid therapy and steroid response in autoimmune pancreatitis," *International Journal of Molecular Sciences*, vol. 21, no. 1, pp. 257–320, 2019.

[79] E. Hsu and R. Pacifici, "From osteoimmunology to osteomicrobiology: how the microbiota and the immune system regulate bone," *Calcified Tissue International*, vol. 102, no. 5, pp. 512–521, 2018.

[80] R. Pacifici, "Bone remodeling and the microbiome," *Cold Spring Harbor Perspectives in Medicine*, vol. 8, no. 4, pp. a031203–a031218, 2018.

Hindawi
Evidence-Based Complementary and Alternative Medicine
Volume 2022, Article ID 8020182, 15 pages
https://doi.org/10.1155/2022/8020182

Research Article

Zuogui Pill Ameliorates Glucocorticoid-Induced Osteoporosis through ZNF702P-Based ceRNA Network: Bioinformatics Analysis and Experimental Validation

Peng Zhang,[1,2,3] Honglin Chen,[1,2,3] Qi Shang,[1,2,3] Guifeng Chen,[1,2,3] Jiahui He,[1,2,3] Gengyang Shen,[2,3] Xiang Yu,[2,3] Zhida Zhang,[2,3] Wenhua Zhao,[1,2,3] Guangye Zhu,[1] Jinglin Huang,[1] De Liang,[2,3] Jingjing Tang,[2,3] Jianchao Cui,[2,3] Zhixiang Liu,[4] Xiaobing Jiang,[2,3] and Hui Ren[2,3]

[1]*The First Clinical School, Guangzhou University of Chinese Medicine, Guangzhou 510405, China*
[2]*The First Affiliated Hospital of Guangzhou University of Chinese Medicine, Guangzhou 510405, China*
[3]*Lingnan Medical Research Center of Guangzhou Univercity of Chinese Medicine, Guangzhou 510405, China*
[4]*Affiliated Huadu Hospital, Southern Medical University, Guangzhou 510800, China*

Correspondence should be addressed to Hui Ren; renhuispine@163.com

Received 1 April 2022; Revised 8 July 2022; Accepted 7 August 2022; Published 29 August 2022

Academic Editor: Jun Jiang

Glucocorticoid-induced osteoporosis (GIOP) is a musculoskeletal disease with increased fracture risk caused by long-term application of glucocorticoid, but there exist few effective interventions. Zuogui Pill (ZGP) has achieved clinical improvement for GIOP as an ancient classical formula, but its molecular mechanisms remain unclear due to scanty relevant studies. This study aimed to excavate the effective compounds and underlying mechanism of ZGP in treating GIOP and construct relative ceRNA network by using integrated analysis of bioinformatics analysis and experimental validation. Results show that ZNF702P is significantly upregulated in GIOP than normal cases based on gene chip sequencing analysis. Totally, 102 ingredients and 535 targets of ZGP as well as 480 GIOP-related targets were selected, including 122 common targets and 8 intersection targets with the predicted mRNAs. The ceRNA network contains one lncRNA (ZNF702P), 6 miRNAs, and 8 mRNAs. Four hub targets including JUN, CCND1, MAPK1, and MAPK14 were identified in the PPI network. Six ceRNA interaction axes including ZNF702P-hsa-miR-429-JUN, ZNF702P-hsa-miR-17-5p/hsa-miR-20b-5p-CCND1, ZNF702P-hsa-miR-17-5p/hsa-miR-20b-5p-MAPK1, and ZNF702P-hsa-miR-24-3p-MAPK14 were obtained. By means of molecular docking, we found that all the hub targets could be effectively combined with related ingredients. GO enrichment analysis showed 649 biological processes, involving response to estrogen, response to steroid hormone, inflammatory response, macrophage activation, and osteoclast differentiation, and KEGG analysis revealed 102 entries with 36 relative signaling pathways, which mainly contained IL-17 signaling pathway, T cell receptor signaling pathway, FoxO signaling pathway, the PD-L1 expression and PD-1 checkpoint pathway, MAPK signaling pathway, TNF signaling pathway, Estrogen signaling pathway, and Wnt signaling pathway. Our experiments confirmed that ZNF702P exhibited gradually increasing expression levels during osteoclast differentiation of human peripheral blood monocytes (HPBMs) induced by RANKL, while ZGP could inhibit osteoclast differentiation of HPBMs induced by RANKL in a concentration-dependent manner. Therefore, by regulating inflammatory response, osteoclast differentiation, and hormone metabolism, ZGP may treat GIOP by regulating hub target genes, such as JUN, CCND1, MAPK1, and MAPK14, and acting on numerous key pathways, which involve the ZNF702P-based ceRNA network.

1. Introduction

As the most common secondary osteoporosis, glucocorticoid-induced osteoporosis (GIOP) is a musculoskeletal disease with destruction of bone microstructure, reduced bone mass and strength, and increased risk of fracture caused by long-term application of glucocorticoid (GC) [1]. Statistics show that millions of adults in the world use long-term GCs for treating diseases such as rheumatoid arthritis and bronchial asthma, while some foods and drugs have excessive amounts of hormones, which make many people take GCs invisibly for a long time [2, 3]. Long-term use of GCs often leads to patients suffering from serious complications such as GIOP and fractures, which not only threaten human health, but also bring heavy economic burden for society and family. Existing drugs including vitamin *D*, calcium, denosumab, teriparatide, and bisphosphonates serve as recommended therapies for the treatment of GIOP [4], but long-term use of them trigger some side effects causing rapid bone loss and increasing the risks of jaw osteonecrosis, atypical femoral fractures, and multiple rebound-related vertebral fractures [5]. The clinical management of GIOP is still debated, so it is indispensable for developing a new drug therapy against GIOP [6].

Recently, substantial achievements have been made against GIOP from the perspective of regulating bone homeostasis [7]. However, the ambiguity of potential targets and the diversity of therapeutic drugs have become the bottleneck for clinically preventing and treating GIOP. Therefore, it has become a pressing clinical need to study the pathogenesis of GIOP and find potential biomarkers against GIOP.

Research shows that GCs can not only inhibit BMSC and osteoblast proliferation as well as preosteoblast differentiation, and promote apoptosis and autophagy in osteoblasts, but also influence osteoclast differentiation and extend osteoclast lifespan, among which miRNA, autophagy, and apoptosis play a crucial part in mediating bone homeostasis in GIOP [3]. In addition, GCs can indirectly mediate bone homeostasis by regulating sex hormones and neuromuscular system [8]. At the same time, our previous studies have also found that miRNAs and autophagy play a key role in the pathogenesis of GIOP, and further confirmed that the imbalance of bone homeostasis is the basic pathological mechanism of GIOP, and the decline of bone formation runs through the onset and progression of GIOP [9, 10].

Long noncoding RNAs (lncRNAs) are a kind of endogenous noncoding RNAs with a length of more than 200 bp and nonlong open reading frame [11, 12]. Studies have revealed that lncRNAs play a vital role in embryonic development, cell proliferation and differentiation, and organogenesis [13–15], and lncRNAs can regulate epigenetic, transcriptional, and post-transcriptional functions [16]. Some lncRNAs can serve as competing endogenous RNAs (ceRNAs) to absorb miRNAs, and thus participate in the expression regulation of target genes [17]. The ceRNA network is an intrinsic mechanism of RNA interaction and regulation. However, it remains unclear whether this mechanism plays a role in regulating bone homeostasis and whether it is involved in the pathogenesis of GIOP.

Traditional Chinese medicine (TCM) has accumulated a wealth of clinical practice experience in the treatment of osteoporosis-related diseases, which has the advantages of mild efficacy, long-lasting effect, low side effects, and long-term use [18]. Zuogui Pill (ZGP), as an ancient classical formula, has been widely used for clinically treating bone diseases like GIOP and fracture [19, 20]. Some studies have demonstrated that ZGP may prevent GIOP in zebrafish larvae by reversing bone formation/resorption imbalance and activating the TGF-β-Smad signal [20]. Additionally, ZGP could upregulate the expression of the vital signal molecules in the Wnt signaling pathway including Wnt1, LRP-5, and β-catenin so as to prevent and treat GIOP [19]. Moreover, our previous studies have confirmed that ZGP could prevent and treat GIOP possibly by downregulating DKK1 mRNA expression [21] or upregulating mTORC1 mRNA expression [22], which could be important targets for preventing and treating GIOP [23]. However, there exist few studies to focus on the ceRNA network involved in the mechanism of ZGP against GIOP. Therefore, this present study aimed to investigate differences in vertebral bone tissue RNA expression data between GIOP patients and normal patients, excavate the effective compounds and underlying mechanism of ZGP in treating GIOP, and construct relative ceRNA network by using integrated analysis of gene chip sequencing, network pharmacology, and experimental validation.

2. Materials and Methods

2.1. Identification of the Differentially Expressed lncRNA in Vertebral Bone Tissue of GIOP Patients Compared to Normal. The total RNA was extracted from vertebral bone tissue of GIOP patients ($n = 3$) and normal patients ($n = 3$) by using Trizol reagents (Invitrogen). The extracted total RNA samples were subjected to agarose electrophoresis and Nanodrop quality inspection and quantification. Oligo magnetic beads were used to enrich the lncRNA, and the KAPA Stranded RNA-Seq Library Prep Kit (Illumina, Aksomics, Shanghai) was used to construct the library. The constructed library was checked by Agilent 2100 Bioanalyzer (Aksomics, Shanghai), and the final quantification of the library was performed by qPCR. According to the quantitative results and the final sequencing data, the sequencing libraries of different samples were mixed into the sequencing process. The screening thresholds to determine the differentially expressed lncRNA were P value <0.05 and $|\log_2$ fold change (FC)$| > 1$. The present study was approved by the Ethics Committee of the 1st Affiliated Hospital of Guangzhou University of Chinese Medicine (GZUCM) with the approval number ZYYECR[2016]028.

2.2. Prediction of Differentially Expressed lncRNA-miRNA Interactions and miRNA-mRNA Interactions. The miRcode database (http://www.mircode.org/) was used to predict lncRNA-miRNA interactions. Then the miRDB database (http://www.mirdb.org/), miRTarBase database (http://mirtarbase.mbc.nctu.edu.tw/php/index.php), and TargetScan

database (http://www.targetscan.org/) were used to predict the miRNA-mRNA interactions, and only the interactions included in all three databases were selected.

2.3. Obtaining the Bioactive Components and Targets of ZGP Drugs. The bioactive components and targets of ZGP drugs including Di Huang, Shan Yao, Gou Qi Zi, Shan Zhu Yu, Niu Xi, Tu Si Zi, Gui Ban, and Lu Jiao were obtained through BATMAN database(http://bionet.ncpsb.org/batman-tcm/) with "score cutoff" set to 48, "P value cutoff" set to 0.05, and "popular organisms" set as humans [19]. Moreover, the active compounds of ZGP drugs were retrieved through the TCMSP database (http://tcmspw.com/tcmsp.php). Gui Ban and Lu Jiao are not included in the TCMSP database, so the bioactive components of Gui Ban and Lu Jiao reported in literature were searched manually to make a supplementary summary. The above components were screened with oral bioavailability (OB) > 30% and drug likeness (DL) > 0.18 to obtain the eligible compounds and their corresponding targets from the TCMSP database [24]. Finally, the bioactive components and targets obtained from the TCMSP platform and BATMAN database were summarized and deduplicated.

2.4. Gene Targets of GIOP. The key word "glucocorticoid-induced osteoporosis" was searched in the GeneCards database (https://www.genecards.org/) [25] with the species set as "Homo sapiens."

2.5. Construction of Drug-Compound-Target Network. Using *R* software (v3.6.1), the targets of GIOP were mapped with the targets of ZGP to obtain the common targets. Then the drugs and compounds corresponding to the common targets were identified and Drug-Compound-Target Network was constructed.

2.6. Construction of ceRNA Network. The overlap between the common targets and the predicted mRNAs mentioned in 2.2 was taken as the intersection targets. The intersection targets as mRNA in ceRNA network were selected and lncRNA-miRNA-mRNA interactions were identified to construct the ceRNA network by Cytoscape3.7.2 (http://www.cytoscape.org/).

2.7. Protein-Protein Interaction (PPI) Analysis. The STRING database (https://string-db.org/) was retrieved to get the PPI data of the intersection targets. Next, the PPI information of the intersection targets was input into Cytoscape (v3.7.2) software to construct the PPI network and calculate degrees and betweenness centralities of targets in the network through network topology analysis. The targets whose degrees and betweenness centralities were above average were determined to be the hub targets.

2.8. Molecular Docking. AutoDock Vina (v1.1.2) software [26] was utilized to carry out molecular docking simulations between hub targets and their corresponding compounds to verify their interaction activity. The Pubchem database (https://pubchem.ncbi.nlm.nih.gov/) was searched for the 3D structure of compounds. AutoDock Tools (v1.5.6) were used to distribute charge and combine nonpolar hydrogen for compounds and convert the results into a PDBQT file. The crystal structures of target proteins from the RCSB PDB website (http://www.rcsb.org/) were downloaded. Then the target protein was separated from its ligand, added polar hydrogen, and distributed charge via AutoDock Tools, which would be subsequently stored as a PDBQT file. AutoDock Tools were also utilized to calculate the center and size of the docking box. Molecular docking simulations among the target proteins and compounds were performed with every affinity calculated. Then PyMol were used to draw and analyze the docking results.

2.9. GO Enrichment Analysis and KEGG Pathway Analysis. Gene Ontology (GO) enrichment analysis concerning biological process (BP) via the clusterProfiler package (R3.6.1) was performed and the enrichment results with $P < 0.05$ were selected. Then the 20 representative items closely related to the pathological process of GIOP were presented. Next, we carried out Kyoto Encyclopedia of Genes and Genomes (KEGG) analysis of the intersection targets using the clusterProfiler package (R3.6.1), extracted the significant enrichment results ($P < 0.05$), and plotted pathway-target network using Cytoscape.

2.10. Experimental Validation by In Vitro Assays

2.10.1. Cells and Reagents. The source of ZGP was obtained from the 1st Affiliated Hospital of GZUCM. Recombinant human TRANCE/TNFSF11/RANKL (6449-TEC) was purchased from R&D Systems (Minneapolis, MN. United States). Recombinant human M-CSF protein (11792-H08Y) was purchased from China Bio (Beijing). The cell counting kit-8 (CCK-8) was purchased from Beyotime, while TRAP working solution was obtained from Sigma Aldrich (St.Louis, MO, USA).

2.10.2. Human Peripheral Blood Monocyte Culture and Assay. The clinical experiments involved in this paper were authorized by the Ethics Committee of the 1st Affiliated Hospital of GZUCM (No. K[2019]129). In the current research, all patients who participated in this trial were provided informed consent at the beginning. Then, 10-mL of external venous blood was drawn from volunteer patients ($n = 3$). The manipulation of human peripheral blood monocytes (HPBMs) was performed as described previously [27]. First, 10-mL of whole blood from patients was put into a 50-mL centrifuge tube, then diluted with 10-mL of PBS and gently mixed. Afterward, we continuously centrifuged the initial blood specimen at 2000 rpm for 20 minutes. When centrifugation was finished, the blood sample was stratified and the leukocyte layer in the center of the sample containing HPBMs was aspirated by pipette and transferred to a single fresh 15 mL centrifuge tube in liquid with 10–15 mL of

PBS. Next, the solution was centrifuged at 1500 rpm for 10 min and the supernatant was lifted to precipitate and be the wanted HPBMs. HPBMs were resuspended in 10 mL of medium containing 20 ng/mL hM-CSF protein and subsequently transferred to culture dishes to incubate for 5 days. Then tartrate-resistant acid phosphatase (TRAP) staining was performed to identify osteoclasts, which are TRAP-positive ($TRAP^+$) cells with more than 3 nuclei. When the incubation time was reached, HPBMs turned into $TRAP^+$ mature osteoclasts after 10 days of cell intervention using 50 ng/mL of hRANKL.

2.10.3. Cell Counting Kit 8 Assay. The HPBMs were treated with a concentration gradient of ZGP for 3, 5, and 7 days after induction of osteoclast development. According to the manufacturer's protocol, we performed a cell counting kit 8 (CCK-8) assay to detect cell proliferation abilities using an optical density (OD) setting of 450 nm in the microplate reader (Varioskan Flash; Thermo Fisher Scientific, Waltham, MA, USA).

2.10.4. RNA Extraction and Real-Time Quantitative Polymerase Chain Reaction (RT-qPCR). HPBMs were inoculated in 6-well plates at a cell count of 2×10^5 cells. After induction of osteoclast development, 1 mL of Trizol reagent was applied to each well for total RNA extraction from the cells. Subsequently, retrotranscription of 1 μg of total RNA was performed using a cDNA synthesis kit (Takara Inc.Shiga, Japan). 20 μL of SYBR Green qPCR SuperMix (Takara Inc.) was used for detection of *ZNF702P* cDNAs and RT-qPCR machine (Bio-Rad, Hercules, CA, USA). The thermal cycling conditions for the final gene amplification were: 95°C for 30 s, 40 cycles of 95°C for 5s, and a final step of 60°C for 30s. Quantitative analysis was performed using the 2ΔΔCT method for the calculation of the relative expression of each gene. The gene-related detection primers of *ZNF702P* (Forward: ACAAGGCATTCGGGTGTGAT; Reverse:ACCACTGAAGGCTCTGTCAC) were compounded by Shanghai Sangon Biotechnology Co.Ltd (China).

2.11. Statistical Analysis. All results were expressed as mean ± standard deviation. Student's *t*-tests were used to compare two separate samples. One-way ANOVA was used for comparison of univariate samples between multiple groups. , P value <0.05 indicates statistical significance.

3. Results

3.1. Differential Expression Analysis of lncRNA in GIOP. To explore differential expressed lncRNA in GIOP, vertebral bone tissue of GIOP patients and normal patients was analyzed, showing that ZNF702P was significantly upregulated in GIOP ($P < 0.0001$), which means that ZNF702P could be a potential biomarker to identify GIOP, as shown in Figure 1.

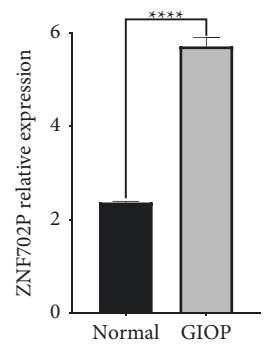

Figure 1: Differential expression analysis of lncRNA in GIOP. Data are displayed as mean ± standard deviation. $^{****}P < 0.0001$.

3.2. lncRNA-miRNA-mRNA Interactions. Totally, 75 ZNF702P-miRNA interactions and 936 miRNA-mRNA interactions were obtained. After removing duplication, there were 621 mRNAs predicted for subsequent analysis, as shown in Supplementary Table 1.

3.3. The Active Compounds and Targets of ZGP. Based on BATMAN database and TCMSP platform, 120 active compounds of ZGP were obtained including 7 compounds from Niu Xi, 3 compounds from Di Huang, 40 compounds from Gou Qi Zi, 4 compounds from Gui Ban, one compound from Lu Jiao, 22 compounds from Shan Yao, 32 compounds from Shan Zhu Yu, and 11 compounds from Tu Si Zi. After the duplicates were removed, 102 bioactive components and 535 targets of ZGP were screened, as shown in Supplementary Table 2.

3.4. The Common Targets of ZGP and GIOP. Through the retrieval of GeneCards database, we obtained a total of 480 gene targets of GIOP. After they were mapped with the targets of ZGP, totally 122 common targets were obtained, as demonstrated in Figure 2 and Table 1.

3.5. Construction of the Drug-Compound-Target Network. The correspondence among the drugs, compounds, and common targets of ZGP in treating GIOP was visualized by Cytoscape, as demonstrated in Figure 3. The network contained 208 nodes and 610 edges, including 8 drug nodes, 78 compound nodes, and 122 target nodes. In Figure 3, the red circle nodes stand for the drugs, the pink triangle nodes stand for active compounds, and the orange V-shape nodes stand for targets. The edges stand for the corresponding relationship among drugs, compounds, and common targets of ZGP in treating GIOP.

3.6. Construction of the ceRNA Network. There are 8 intersection targets between the predicted mRNAs and the common targets, as shown in Figure 4. Then we constructed the ceRNA network through ZNF702P-miRNA-mRNA interactions, as shown in Figure 5.

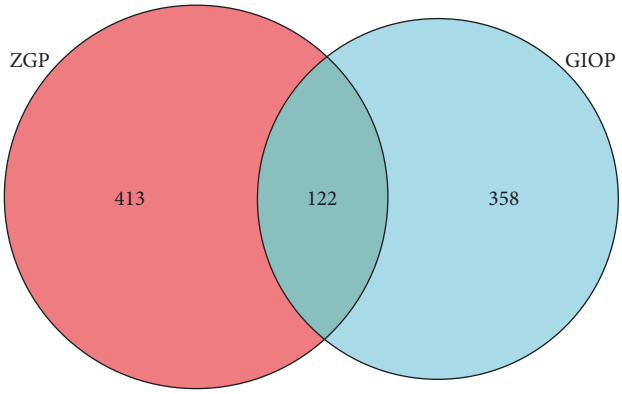

Figure 2: Venn diagram of ZGP-GIOP common targets.

3.7. PPI Network Construction and Hub Target Screening. The intersection targets were imported into the STRING database. And then we imported the PPI data into Cytoscape (v 3.7.2) to draw the PPI network in Figure 6. There were 4 targets including JUN, CCND1, MAPK1, and MAPK14 whose degrees and betweenness centralities were above the average, which were predicted as the hub targets. The detailed network topology information was shown in Supplementary Table 3.

3.8. Molecular Docking Validation. The 3D structures of the 4 hub genes were obtained through the RCSB PDB database. According to Table 2, all the hub targets demonstrated good and stable binding activity with their bioactive compounds. Then the docking results of all the hub targets with the strongest binding ability were visualized in Figure 7. For example, sesamin combined with CCND1 by forming Pi-alkyl bonds with the residues including Arg-63 and Leu-67 (docking affinity: -6.3 kcal/mol). The docking affinity of beta-sitosterol on JUN was -6.8 kcal/mol. The residues containing Arg-26 and Lys-30 were linked to beta-sitosterol by forming alkyl bonds. The docking affinity of quercetin on MAPK1 was -8.5 kcal/mol. There existed hydrogen bonds provided by the Gln-95, Glu-99, and Asp-157 residues in the link to quercetin. The docking affinity of beta-vulgarin on MAPK14 was -9.6 kcal/mol. The residue Thr-102 formed one hydrogen bond in the interaction with beta-vulgarin. In addition, the residues Leu-100, Leu-71, Lys-49, and Leu-167 provided a powerful electrostatic force for the combination of beta-vulgarin and MAPK14.

3.9. GO Enrichment Analysis. Totally 649 items of biological process (BP) were obtained, among which the filtrated 20 items involving anti-GIOP effects of ZGP were closely correlated with cellular senescence, negative regulation of phosphorylation, activation of MAPK activity, response to estrogen, response to steroid hormone, inflammatory response, macrophage activation and osteoclast differentiation, etc. GO,BP enrichment analysis results are shown in Figure 8.

Table 1: Potential target genes of ZGP in the treatment of GIOP.

Number	Gene	Number	Gene	Number	Gene
1	NR3C2	42	HMOX1	83	TAT
2	NOS2	43	CYP3A4	84	PLA2G4A
3	PTGS1	44	CYP1A2	85	FASN
4	ESR1	45	MYC	86	MTOR
5	AR	46	ICAM1	87	SAA1
6	PPARG	47	IL1B	88	PDE4B
7	PTGS2	48	CCL2	89	PDE4D
8	ESR2	49	VCAM1	90	PDE4A
9	MAPK14	50	CXCL8	91	ANXA1
10	GSK3B	51	PRKCB	92	SLC9A3R1
11	CDK2	52	BIRC5	93	TYR
12	PIK3CG	53	IL2	94	PRKAB1
13	PRKACA	54	NR1I2	95	KCNQ1
14	PDE3A	55	SERPINE1	96	PRKCD
15	ADRB2	56	IFNG	97	PDE2A
16	BCL2	57	IL1A	98	SCNN1A
17	BAX	58	NFE2L2	99	PRKAA1
18	CASP9	59	AHR	100	TLR7
19	JUN	60	SLC2A4	101	KCNJ1
20	CASP3	61	NR1I3	102	AGTR1
21	CASP8	62	INSR	103	ACP1
22	TGFB1	63	PPARA	104	PRKAA2
23	RELA	64	CHUK	105	INS
24	AKT1	65	SPP1	106	CALCA
25	VEGFA	66	RUNX2	107	PDE7B
26	CCND1	67	IGFBP3	108	PIK3CA
27	BCL2L1	68	IGF2	109	PDE1A
28	FOS	69	IRF1	110	PIK3CB
29	CDKN1A	70	GSTM1	111	PDE7A
30	MMP9	71	ADRB1	112	PDE4C
31	MAPK1	72	GRIN2A	113	PDE1C
32	IL10	73	GRIN2B	114	CYP19A1
33	EGF	74	HTR1A	115	PDE8A
34	RB1	75	APP	116	PIK3R1
35	TNF	76	CCNA2	117	PPP2CA
36	IL6	77	NR3C1	118	ACE
37	TP53	78	PIM1	119	SLPI
38	NFKBIA	79	VDR	120	CD44
39	MMP1	80	ASS1	121	IKBKB
40	STAT1	81	TRAF2	122	MAPK8
41	ERBB2	82	FDPS		

3.10. KEGG Pathway Analysis. The KEGG pathway enrichment analysis of 8 target genes was conducted using *R* software. We finally got 102 items including 36 key signaling pathways, as described in Table 3. We conducted network visualization via Cytoscape as plotted in Figure 9. According to Figure 9, we have deeply filtered the key signaling pathways, and selected four core signaling pathways, including the IL-17 signaling pathway, T cell receptor signaling pathway, FoxO signaling pathway, PD-L1 expression and PD-1 checkpoint pathway, which may play an important role in the pathophysiology of GIOP.

3.11. RT-qPCR Analysis. In contrast to the control group, ZNF702P exhibited gradually increasing expression levels during osteoclast differentiation of HPBMs induced by RANKL from 3 days to 5 days (Figure 10(a)). It suggests that the expression level of ZNF702P is positively correlated with osteoclast differentiation.

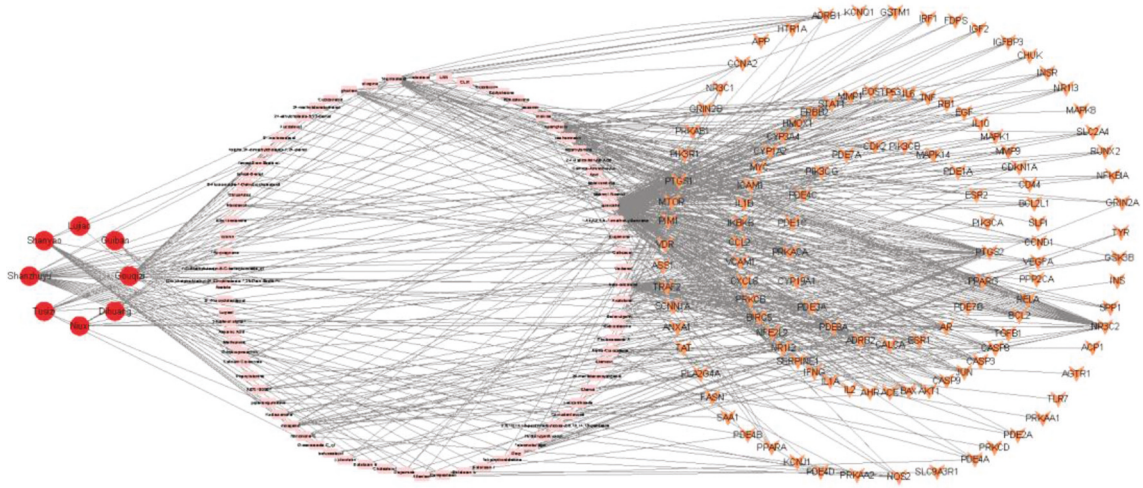

Figure 3: Drug-compound-target network.

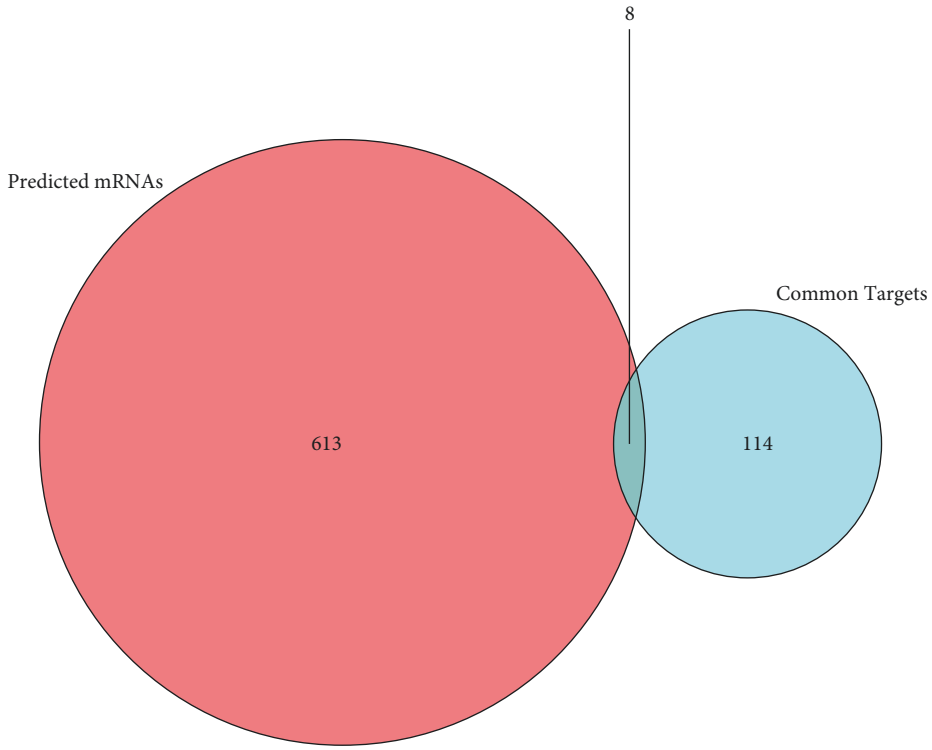

Figure 4: The overlap between the common targets and the predicted mRNAs.

3.12. CCK-8 Analysis. CCK-8 results showed that there was no cytotoxicity to HPBMs when the ZGP concentrations were no higher than 1000 ng/mL with the proliferation of HPBMs neither promoted nor inhibited, which were selected for subsequent experiments (Figure 10(b)).

3.13. TRAP Staining Analysis. After HPBMs were induced to osteoclast differentiation, the effects of ZGP were detected during this process (Figure 10(c)). TRAP staining results revealed that the number and area of $TRAP^+$ cells decreased rapidly with increasing ZGP concentration, suggesting that ZGP could inhibit osteoclast differentiation (Figures 10(d)–10(e)).

4. Discussion

GIOP is a systemic bone disease secondary to glucocorticoid intake, which is the most common secondary osteoporosis [28]. Although numerous protein-coding genes have been identified to be GIOP-related genes [29], these genes could not give a good interpretation to the onset and development of GIOP. Currently, multiple studies have focused on the epigenetic regulation and the roles of lncRNAs in the pathogenesis of osteoporosis [30]. In this study, we constructed the ZNF702P-associated ceRNA network according to the expression profiles of vertebral bone tissues between GIOP patients and healthy controls.

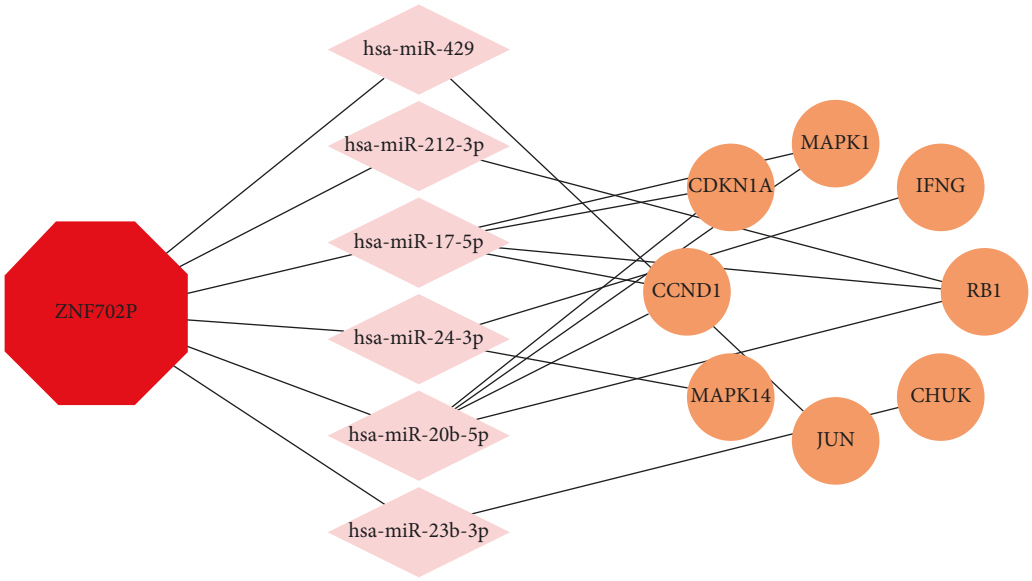

Figure 5: The ceRNA network.

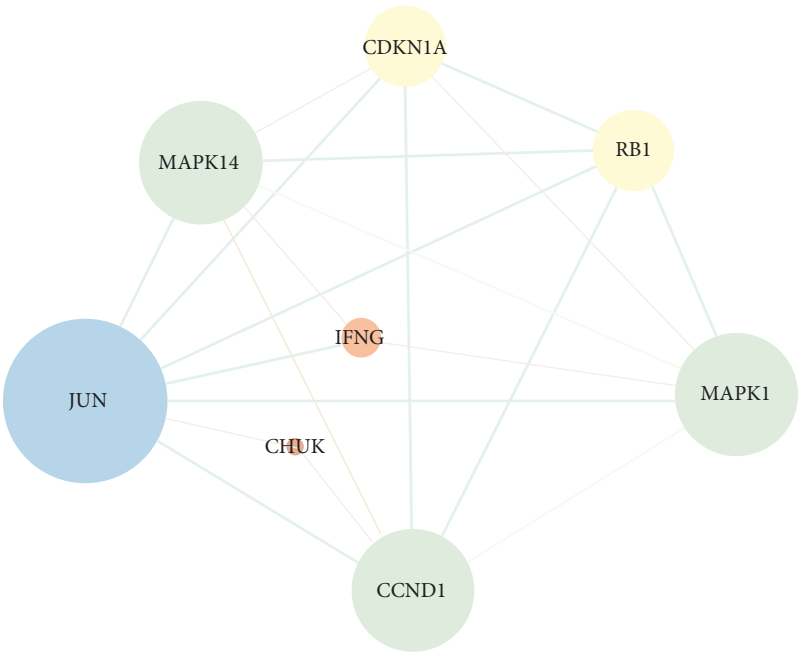

Figure 6: PPI network of intersection targets.

Table 2: Docking scores of hub targets with their bioactive compounds.

Targets	PDB ID	Compounds	Affinity (kcal/mol)
CCND1	2W9F	Quercetin	−5.7
CCND1	2W9F	Sesamin	−6.3
JUN	1JNM	Beta-sitosterol	−6.8
JUN	1JNM	Quercetin	−5.2
JUN	1JNM	Kaempferol	−5.3
MAPK1	5NHV	Quercetin	−8.5
MAPK14	2GTN	Beta-vulgarin	−9.6
MAPK14	2GTN	Glycitein	−8.7
MAPK14	2GTN	Isorhamnetin	−9.0

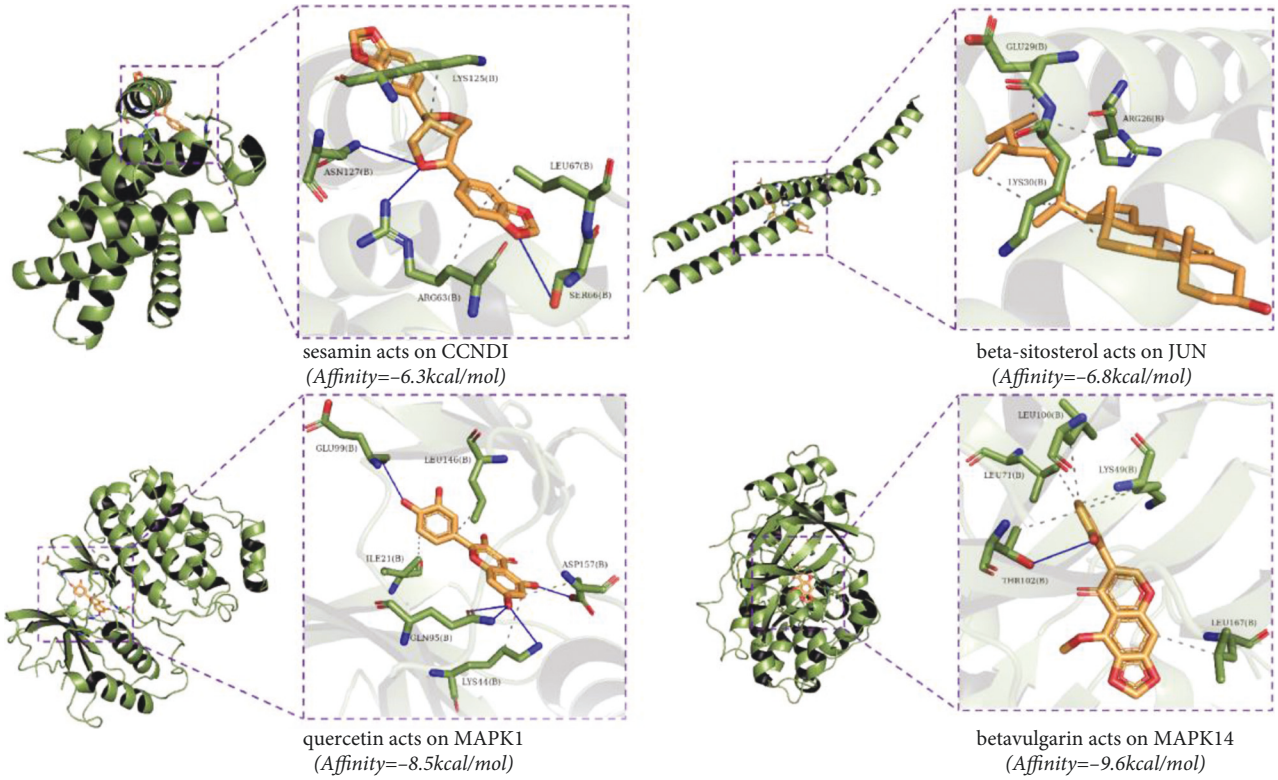

Figure 7: Detailed target-compound interactions with the highest molecular docking affinities.

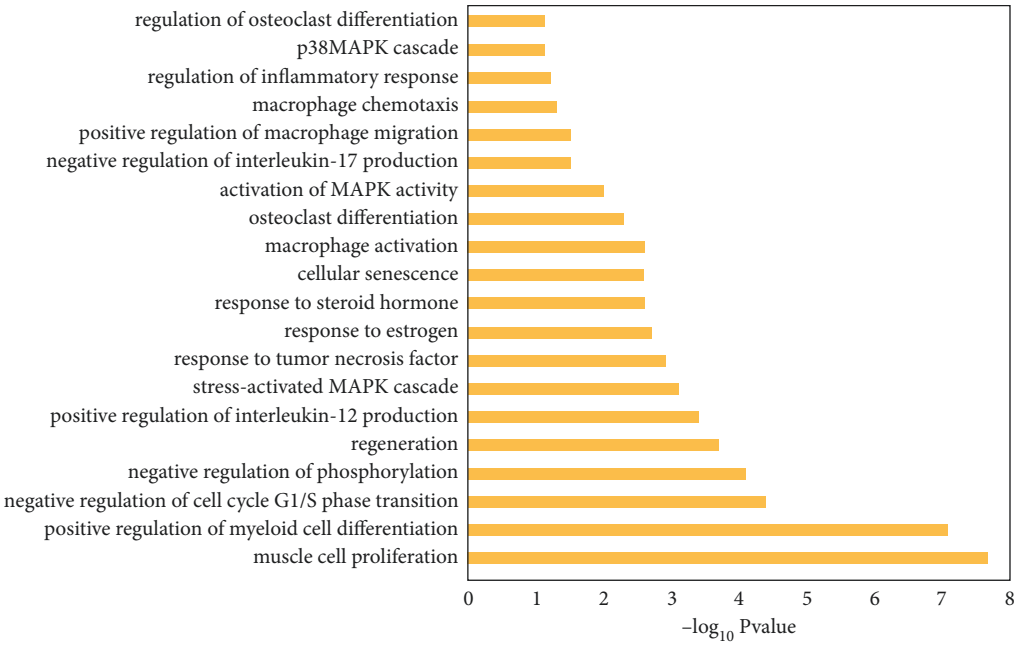

Figure 8: GO, BP enrichment analysis.

Chinese traditional formula Zuogui Pill has been widely used for clinically treating GIOP for many years as an ancient classical formula [20,31]. Zuogui Pill has been confirmed to exert ameliorative effects on postmenopausal osteoporosis in rat by regulating transduction of coupling signals between osteoblast and osteoclast as well as the differentiation of osteoclasts [19]. ZGP can upregulate the expression of the crucial molecules in the Wnt signaling pathway, including Wnt1, LRP-5, and β-catenin, thus preventing and treating GIOP in rats [20]. ZGP can also activate osteogenic differentiation of BMSCs [32].

Table 3: KEGG pathway enrichment analysis.

Id	Signaling pathway	Enriched genes	*P* value
hsa05235	PD-L1 expression and PD-1 checkpoint pathway	CHUK/IFNG/MAPK1/MAPK14/JUN	0.000000008
hsa04657	IL-17 signaling pathway	CHUK/IFNG/MAPK1/MAPK14/JUN	0.000000010
hsa04660	T cell receptor signaling pathway	CHUK/IFNG/MAPK1/MAPK14/JUN	0.000000017
hsa04068	FoxO signaling pathway	CHUK/MAPK1/CDKN1A/CCND1/MAPK14	0.000000055
hsa04933	AGE-RAGE signaling pathway in diabetic complications	MAPK1/CCND1/MAPK14/JUN	0.000001473
hsa04620	Toll-like receptor signaling pathway	CHUK/MAPK1/MAPK14/JUN	0.000001724
hsa04625	C-type lectin receptor signaling pathway	CHUK/MAPK1/MAPK14/JUN	0.000001724
hsa04668	TNF signaling pathway	CHUK/MAPK1/MAPK14/JUN	0.000002322
hsa04921	Oxytocin signaling pathway	MAPK1/CDKN1A/CCND1/JUN	0.000008283
hsa04621	NOD-like receptor signaling pathway	CHUK/MAPK1/MAPK14/JUN	0.000015728
hsa04917	Prolactin signaling pathway	MAPK1/CCND1/MAPK14	0.000033537
hsa04662	B cell receptor signaling pathway	CHUK/MAPK1/JUN	0.000053955
hsa04012	ErbB signaling pathway	MAPK1/CDKN1A/JUN	0.000060091
hsa04912	GnRH signaling pathway	MAPK1/MAPK14/JUN	0.000078655
hsa04010	MAPK signaling pathway	CHUK/MAPK1/MAPK14/JUN	0.000105958
hsa04066	HIF-1 signaling pathway	IFNG/MAPK1/CDKN1A	0.000126302
hsa04722	Neurotrophin signaling pathway	MAPK1/MAPK14/JUN	0.000163970
hsa04926	Relaxin signaling pathway	MAPK1/MAPK14/JUN	0.000208317
hsa04151	PI3K-akt signaling pathway	CHUK/MAPK1/CDKN1A/CCND1	0.000218113
hsa04630	JAK-STAT signaling pathway	IFNG/CDKN1A/CCND1	0.000408207
hsa04370	VEGF signaling pathway	MAPK1/MAPK14	0.001419283
hsa04664	Fc epsilon RI signaling pathway	MAPK1/MAPK14	0.001881216
hsa04622	RIG-I-like receptor signaling pathway	CHUK/MAPK14	0.001992380
hsa04115	p53 signaling pathway	CDKN1A/CCND1	0.002164888
hsa04350	TGF-beta signaling pathway	IFNG/MAPK1	0.003563485
hsa04071	Sphingolipid signaling pathway	MAPK1/MAPK14	0.005653447
hsa04919	Thyroid hormone signaling pathway	MAPK1/CCND1	0.005840102
hsa04371	Apelin signaling pathway	MAPK1/CCND1	0.007434779
hsa04915	Estrogen signaling pathway	MAPK1/JUN	0.007540373
hsa04550	Signaling pathways regulating pluripotency of stem cells	MAPK1/MAPK14	0.008078683
hsa04150	mTOR signaling pathway	CHUK/MAPK1	0.009440243
hsa04310	Wnt signaling pathway	CCND1/JUN	0.010773382
hsa04062	Chemokine signaling pathway	CHUK/MAPK1	0.014239283
hsa04015	Rap1 signaling pathway	MAPK1/MAPK14	0.016890221
hsa04024	cAMP signaling pathway	MAPK1/JUN	0.017818328
hsa04014	Ras signaling pathway	CHUK/MAPK1	0.020399537

In our previous studies, we have established GIOP rat model with subcutaneous injection of dexamethasone, and we have confirmed that ZGP treatment could ameliorate GIOP with enhanced volumetric bone mineral density, bone mineral content, trabecular bone volume fraction, trabecular number, and vertebral compressive strength [21, 22]. Moreover, we have found that Gui Ban (*Plastrum Testudinis*), one main drug in Zuogui Pill, may reverse GIOP by targeting OPG, Runx2, and CTSK [33]. To our knowledge, few studies have been reported on the regulation of mRNA expression and protein levels through ZNF702P-based ceRNA network in the treatment of GIOP by ZGP. These complex networks may provide multiple clues to elucidate the pathogenesis of GIOP. Therefore, this study first explored ZNF702P as a potential biomarker, thus exerting therapeutic effect of ZGP on GIOP.

To identify the core of ceRNA networks, we got 4 hub targets including JUN, CCND1, MAPK1, and MAPK14 by PPI analysis. Then AutoDock Vina was used to verify the binding activity among hub targets and their related components with binding energy less than -5.0 kcal/mol, which showed good and stable combination with each other [34]. According to drug-compound-target network and molecular docking results, the active compounds with high values consisted of quercetin, sesamin, beta-sitosterol, and kaempferol. Quercetin is identified as an antiosteoporotic flavonoid, which promotes osteogenesis, antioxidant expression, angiogenesis, osteoclast, and adipocyte apoptosis, while inhibiting RANKL-mediated osteoclastogenesis, osteoblast apoptosis, oxidative stress, and inflammatory response [35]. Sesamin, a member of the lignan family, has estrogenic activity and plays an important role in healing osteoporotic fracture by activating angiogenesis and chondrogenesis [36]. Moreover, existing study reveals that sesamin could promote osteogenesis by upregulating the Wnt/β-catenin pathway and inhibit osteoclastogenesis by downregulating the NF-κB pathway, suggesting that it could be a therapeutic medication for osteoporosis treatment [37]. As a major phytosterol in plants, beta-sitosterol has medical benefit of bone strengthening, which was reported to exert protective function on GIOP in rats via the RANKL/OPG pathway [38]. Kaempferol, as a natural anti-inflammatory flavonoid, has been reported to have curative effects on ameliorating GIOP via activating the JNK and the p38-

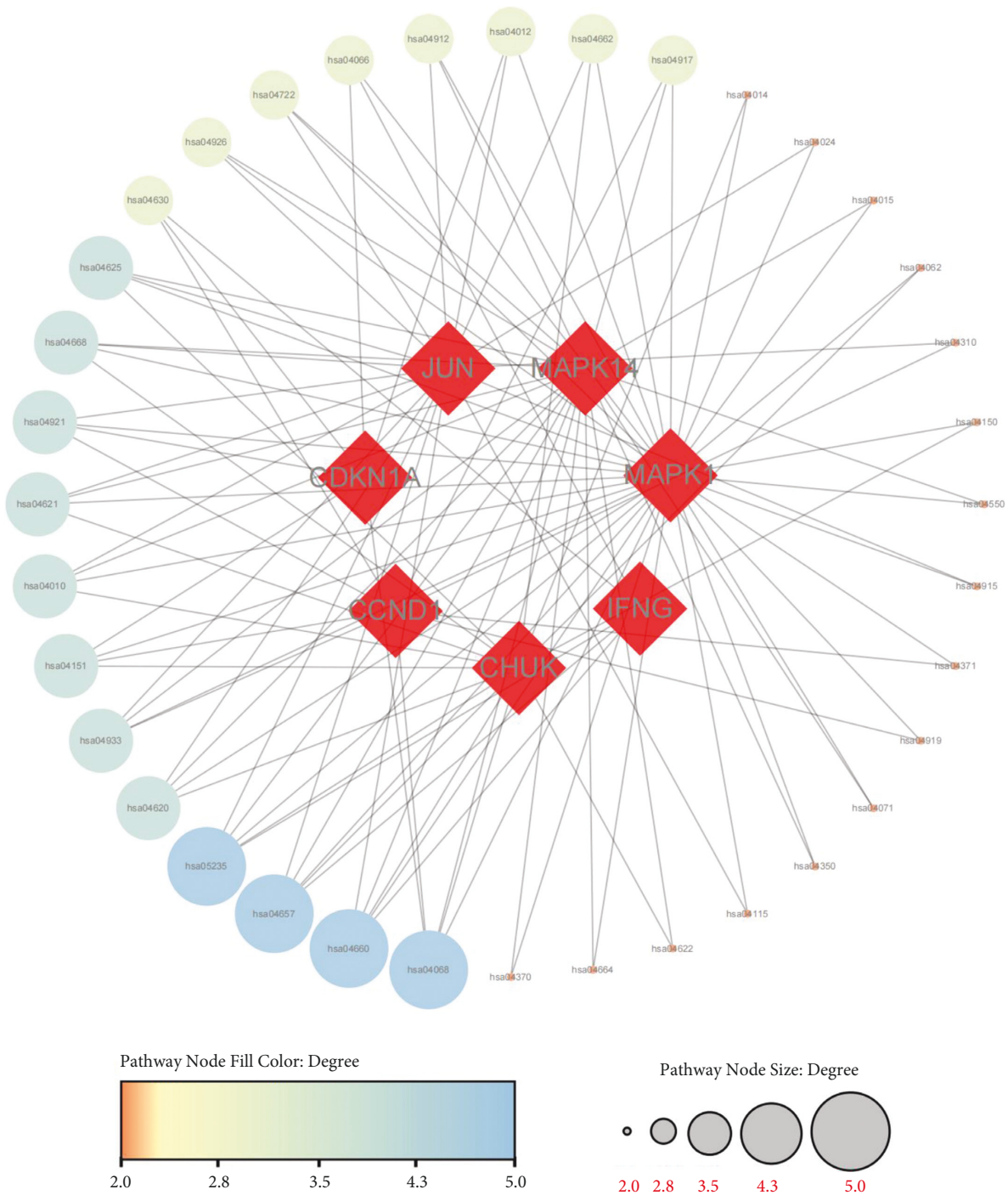

Figure 9: Pathway-target network.

MAPK signaling pathways in dexamethasone-treated MC3T3-E1 cells and improving bone mineralization [39].

The pathophysiology of GIOP is related to inhibiting the proliferation of osteoblasts, promoting the apoptosis of osteoblasts and lengthening the lifespan of osteoclasts, which has received increasing attention [4]. JUN is an important molecule on the MAPK signaling pathway, which is considered as a leading factor mediating RANKL and affecting osteoclastogenesis [40]. Mitigating the downstream levels of c-Jun contributes to inactivating the NF-κB/MAPK signaling pathway and NFATc-1, which suppresses the expression of osteoclast-specific genes and inhibits osteoclastogenesis [41]. CCND1(Cyclin D1) is an important gene to regulate the cell cycle, which is closely linked with bone formation [42]. The glucocorticoid receptor (GR) represses CCND1 via Tcf-β-catenin, the transcriptional effector of the Wnt signaling pathway [43]. The downregulation of CCND1 expression could inhibit osteogenic proliferation and differentiation of MC3T3-E1 cells, as MC3T3-E1 cell apoptosis targeting CCND1 might be regulated by the Wnt/β-catenin

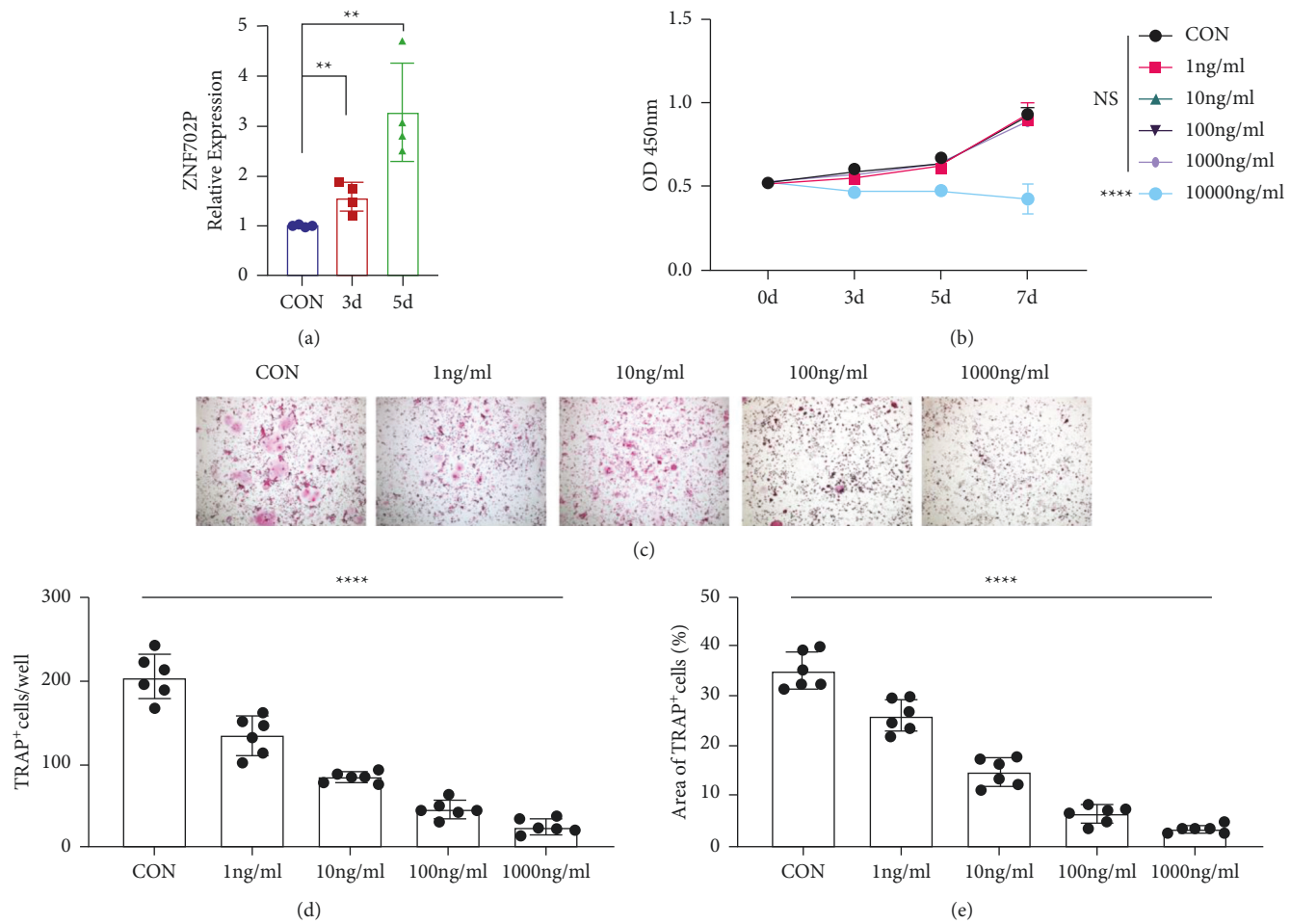

Figure 10: Experimental validation by *in vitro* asays (a) RT-qPCR validated that ZNF702P exhibited gradually increasing expression levels during osteoclast differentiation of HPBMs induced by RANKL. (b) CCK-8 assays with different concentrations of ZGP. (c) TRAP staining analysis showed that ZGP could inhibit osteoclast differentiation of HPBMs induced by RANKL in a concentration-dependent manner. Histograms of the count (d) and area (e) of TRAP$^+$ multinucleated cells per well. Data are displayed as mean ± standard deviation. $^{**}P < 0.01$; $^{****}P < 0.0001$.

pathway [31]. Therefore, CCND1 may be a potential biomarker against GIOP.

MAPK1 is a key molecule in the inflammatory response of chondrocytes [44]. The inhibition of MAPK1 could enhance apoptosis induced by GC [45]. Moreover, MAPK1 is a regulatory factor on the ERK signaling pathway involved in regulation of osteoblast differentiation which may be a promising target in preventive and therapeutic strategies for GIOP [46]. MAPK14 is one of the four p38 MAPKs, which plays a key role in physical stress or proinflammatory cytokines leading to direct activation of transcription factors [47]. In mammals, phosphorylated-MAPK14 is able to transcriptionally activate Serum Glucocorticoid Kinase 1(SGK1) [48], which is a regulator in osteoclastogenesis and bone homeostasis [49].

Importantly, six key ceRNA interaction axes including ZNF702P-hsa-miR-429-JUN, ZNF702P-hsa-miR-17-5p/hsa-miR-20b-5p-CCND1, ZNF702P-hsa-miR-17-5p/hsa-miR-20b-5p-MAPK1, and ZNF702P-hsa-miR-24-3p-MAPK14 were obtained. Evidence has revealed that overexpression of miR-429 promoted MC3T3-E1 cell differentiation, and enhanced matrix mineralization and alkaline phosphatase activity [50]. Some studies have demonstrated that miR-429 downregulated JUN expression [51]. Research has confirmed that miR-17-5p could suppress osteogenic differentiation and inhibit bone formation [52]. It has been revealed that miR-17-5p upregulated CCND1 expression [53], but downregulated the expression of MAPK1 mRNA [54]. It has been reported that miR-20b-5p exhibited regulatory effect on the Wnt signaling pathway related to osteogenesis [55], while overexpression of miR-20b-5p downregulated CCND1 expression [56]. And some studies also showed that miR-20b-5p was highly linked to MAPK1 [57]. Additionally, miR-24-3p serves as a regulatory factor of Smad5, which exerts important functions on osteogenic differentiation [58]. Also, evidence demonstrated that the overexpression of miR-24-3p upregulated the phosphorylation activity of MAPK14 [59].

Then we conducted GO and KEGG enrichment analyses of the intersection targets and identified not only multiple

biological processes correlated with GIOP, including cellular senescence, activation of MAPK activity, response to estrogen, response to steroid hormone, the differentiation of osteoclast, the activation of macrophages, and inflammatory response, but also numerous signaling pathways, including the IL-17 signaling pathway, T cell receptor signaling pathway, FoxO signaling pathway, PD-L1 expression and PD-1 checkpoint pathway, MAPK signaling pathway, TNF signaling pathway, Estrogen signaling pathway, and Wnt signaling pathway. In general, the functional analyses focused on three aspects including regulation of inflammatory response, cell cycle-like osteoclast differentiation, and hormone metabolism, all of which take part in the pathogenesis of GIOP. Notably, osteoclast differentiation is activated and promoted during the progression of GIOP [5]. Our *in vitro* experiments confirmed that ZNF702P exhibited gradually increasing expression levels during osteoclast differentiation of HPBMs induced by RANKL. The expression level of ZNF702P is positively correlated with osteoclast differentiation, which is consistent with the results in Figure 1, indicating that ZNF702P could serve as a biomarker of osteoclastogenesis activation, which plays an important role in GIOP. Moreover, our *in vitro* experiments validated that ZGP could inhibit osteoclast differentiation of HPBMs induced by RANKL in a concentration-dependent manner. It is speculated that ZGP may suppress the expression levels of ZNF702P in HPBMs to inhibit osteoclast differentiation so as to anti-GIOP.

According to the KEGG pathway analysis, there are several signaling pathways worthy to explore in the future researches. For instance, the IL-17 signaling pathway participates in regulating osteoclast differentiation, and the IL-17 signaling pathway can stimulate the synthesis of TNF-α, IL-6, and NF-κB, thereby promoting RANKL-induced osteoclast differentiation [60]. Moreover, studies have shown that the inflammatory factor, TNF-α, can promote RANKL expression and induce osteoclast formation [61,62]. So, the IL-17 signaling pathway [63] and the TNF signaling pathway [64] are closely correlated with the regulation of osteoclasts by the OPG/RANKL/RANK system. Therefore, the IL-17 and TNF signaling pathways might exert important functions in the process of ZGP treatment against GIOP, which needs further identification. PD-L1 expression and PD-1 checkpoint pathway is closely linked to bone homeostasis, and lack of members in this pathway leads to deterioration of bone structure [65]. The FoxO signaling pathway exerts essential effects on regulating bone cell functions including bone development, remodeling, and homeostasis, which contributes to osteoporosis [66]. The T cell receptor signaling pathway is reported to be associated with bone loss [67]. Modern studies have confirmed that the inhibition of the MAPK signaling pathway can suppress osteoclastogenesis and bone resorption [68]. Based on the KEGG pathway analysis, osteoclast-specific genes including MAPK1, MAPK14, and JUN were enriched in the MAPK signaling pathway. Thus, we speculate that ZGP might regulate the expression of MAPK1, MAPK14, and JUN on MAPK signaling way so as to inhibit osteoclast differentiation and bone resorption, which may be the potential mechanism of ZGP treating GIOP. Notably, the estrogen signaling pathway can combine the Wnt signaling pathway and the protein kinase pathway to exert regulatory functions on osteoblasts' and osteoclasts' proliferation, apoptosis, and differentiation [69]. Moreover, both the MAPK and estrogen signaling pathways have been reported to regulate bone formation and bone mass control [70].

Collectively, our results predicted some potential therapeutic targets and pathways, providing reference for future studies on ZGP treatment against GIOP. However, one limitation of this study is that further *in vivo* and *in vitro* experiments are needed to confirm our findings.

5. Conclusion

By regulating inflammatory response, osteoclast differentiation, and hormone metabolism, ZGP may treat GIOP by regulating hub target genes, such as JUN, CCND1, MAPK1, and MAPK14, and acting on numerous key pathways, which involve ZNF702P-based ceRNA network. Our findings firstly offered novel insights into the roles of ZNF702P-based ceRNA interaction axes in the pathogenesis of GIOP and provided potential diagnostic biomarkers. However, the specific mechanism and material basis still need to be further verified *in vivo* and *in vitro*.

Data Availability

The datasets used and analyzed during the current study are available from the first author on reasonable request.

Ethical Approval

The present study was approved by the Ethics Committee of the 1st Affiliated Hospital of GZUCM with approval numbers ZYYECR[2016]028 and No. K[2019]129.

Conflicts of Interest

The authors declare that they have no conflicts of interest.

Authors' Contributions

All authors participated in study conception, design, and data analysis and helped to draft the manuscript. All authors read and approved the submitted manuscript. The authors Peng Zhang, Honglin Chen, and Qi Shang contributed equally to this work.

Acknowledgments

The project was generously supported by the grants from National Natural Science Foundation of China (81774338 and 81904225), Guangdong Natural Science Foundation (2020A1515110322, 2021A1515011247 and 2022A1515012062), Innovative Team Project and Key Project of the Department of Education of Guangdong Province (2021KCXTD017 and 2018KZDXM021), High-Level University Collaborative Innovation Team of GZUCM (2021xk57), Guangzhou Clinical Characteristic Technology

Project (2019TS70), General Project of Guangdong Traditional Chinese Medicine Bureau (20221308), Medical Research Foundation of Guangdong Province (A2021320), Guangzhou Science and Technology Project (202201011169 and 202201020307), Young Talent Support Project of Guangzhou Association for Science and Technology (QT20220101302), Graduate Research Innovation Project of Guangzhou University of Chinese Medicine (A1-2606-21-429-001Z22), and 2022 Provincial Undergraduate Innovation and Entrepreneurship Training Program of Guangzhou University of Chinese Medicine (202210572088).

Supplementary Materials

Supplementary Table 1. LncRNA-miRNA-mRNA interactions. *Supplementary Table 2.* The drugs, active compounds, and targets of ZGP. *Supplementary Table 3.* Detailed network topology information of intersection targets. (*Supplementary Materials*)

References

[1] Y. Zhang, M. Li, Z. Liu, and Q. Fu, "Arbutin ameliorates glucocorticoid-induced osteoporosis through activating autophagy in osteoblasts," *Experimental Biology and Medicine (Maywood, NJ, United States)*, vol. 246, no. 14, pp. 1650–1659, 2021.

[2] R. M. R. Pereira, M. O. Perez, A. P. Paula et al., "Guidelines for the prevention and treatment of glucocorticoid-induced osteoporosis: an update of Brazilian Society of Rheumatology (2020)," *Archives of Osteoporosis*, vol. 16, no. 1, p. 49.

[3] K. Hartmann, M. Koenen, S. Schauer et al., "Molecular actions of glucocorticoids in cartilage and bone during health, disease, and steroid therapy," *Physiological Reviews*, vol. 96, no. 2, pp. 409–447, 2016.

[4] P. Chotiyarnwong and E. V. McCloskey, "Pathogenesis of glucocorticoid-induced osteoporosis and options for treatment," *Nature Reviews Endocrinology*, vol. 16, no. 8, pp. 437–447, 2020.

[5] J. Han, L. Li, C. Zhang et al., "Eucommia, cuscuta, and drynaria extracts ameliorate glucocorticoid-induced osteoporosis by inhibiting osteoclastogenesis through PI3K/akt pathway," *Frontiers in Pharmacology*, vol. 12, Article ID 772944, 2021.

[6] I. Chiodini, D. Merlotti, A. Falchetti, and L. Gennari, "Treatment options for glucocorticoid-induced osteoporosis," *Expert Opinion on Pharmacotherapy*, vol. 21, no. 6, pp. 721–732, 2020.

[7] L. Wang, B. L. Heckmann, X. Yang, and H. Long, "Osteoblast autophagy in glucocorticoid-induced osteoporosis," *Journal of Cellular Physiology*, vol. 234, no. 4, pp. 3207–3215, 2019.

[8] R. Rizzoli and E. Biver, "Glucocorticoid-induced osteoporosis: who to treat with what agent," *Nature Reviews Rheumatology*, vol. 11, no. 2, pp. 98–109, 2015.

[9] H. Ren, D. Liang, X. Jiang et al., "Variance of spinal osteoporosis induced by dexamethasone and methylprednisolone and its associated mechanism," *Steroids*, vol. 102, pp. 65–75, 2015.

[10] H. Ren, D. Liang, G. Shen et al., "Effects of combined ovariectomy with dexamethasone on rat lumbar vertebrae," *Menopause*, vol. 23, no. 4, pp. 441–450, 2016.

[11] D. de Gonzalo-Calvo and C. Bar, "Going the long noncoding RNA way toward cardiac regeneration: mapping candidate long noncoding RNA controllers of regeneration," *Canadian Journal of Cardiology*, vol. 37, no. 3, pp. 374–376, 2021.

[12] J. E. Wilusz, H. Sunwoo, and D. L. Spector, "Long noncoding RNAs: functional surprises from the RNA world," *Genes & Development*, vol. 23, no. 13, pp. 1494–1504, 2009.

[13] M. Kretz, D. E. Webster, R. J. Flockhart et al., "Suppression of progenitor differentiation requires the long noncoding RNA ANCR," *Genes & Development*, vol. 26, no. 4, pp. 338–343, 2012.

[14] P. J. Batista and H. Y. Chang, "Long noncoding RNAs: cellular address codes in development and disease," *Cell*, vol. 152, no. 6, pp. 1298–1307, 2013.

[15] P. Grote, L. Wittler, D. Hendrix et al., "The tissue-specific lncRNA Fendrr is an essential regulator of heart and body wall development in the mouse," *Developmental Cell*, vol. 24, no. 2, pp. 206–214, 2013.

[16] Y. Ren, Y. Song, L. Zhang et al., "Coding of non-coding RNA: insights into the regulatory functions of pri-MicroRNA-encoded peptides in plants," *Frontiers of Plant Science*, vol. 12, Article ID 641351, 2021.

[17] Y. Tay, J. Rinn, and P. P. Pandolfi, "The multilayered complexity of ceRNA crosstalk and competition," *Nature*, vol. 505, no. 7483, pp. 344–352, 2014.

[18] W. L. Lin, P. Y. Lin, Y. C. Hung, and T. P. Hsueh, "Benefits of herbal medicine on bone mineral density in osteoporosis: a meta-analysis of randomized controlled trials," *The American Journal of Chinese Medicine*, vol. 48, no. 08, pp. 1749–1768, 2020.

[19] M. J. Liu, Y. Li, J. H. Pan et al., "Effects of zuogui pill (see text) on Wnt singal transduction in rats with glucocorticoid-induced osteoporosis," *Journal of Traditional Chinese Medicine*, vol. 31, no. 2, pp. 98–102, 2011.

[20] H. Yin, S. Wang, Y. Zhang, M. Wu, J. Wang, and Y. Ma, "Zuogui Pill improves the dexamethasone-induced osteoporosis progression in zebrafish larvae," *Biomedicine & Pharmacotherapy*, vol. 97, pp. 995–999, 2018.

[21] Z. Zhang, H. Ren, G. Shen, and Y. Zhang, "Zuogui pill regulates DKK1 in the prevention and treatment of glucocorticoid-induced osteoporosis," *Chinese Journal of Tissue Engineering Research*, vol. 22, pp. 2520–2525, 2018.

[22] J. Huang, H. Ren, and G. Shen, "Effects of zuogui pill on the expression of mTORC1 mRNA in lumbar vertebrae of glucocorticoid-induced osteoporosis," *Journal of Traditional Chinese Medicine*, vol. 59, no. 16, pp. 1405–1409, 2018.

[23] H. Z. Ke, W. G. Richards, X. Li, and M. S. Ominsky, "Sclerostin and Dickkopf-1 as therapeutic targets in bone diseases," *Endocrine Reviews*, vol. 33, no. 5, pp. 747–783, 2012.

[24] M. Chen and Q. Sun, "Systemic pharmacology understanding of the key mechanism of Sedum sarmentosum Bunge in treating hepatitis," *Naunyn-Schmiedeberg's Archives of Pharmacology*, vol. 394, no. 2, pp. 421–430, 2021.

[25] G. Stelzer, N. Rosen, I. Plaschkes et al., "The GeneCards suite: from gene data mining to disease genome sequence analyses," *Current Protocols in Bioinformatics*, vol. 54, 2016.

[26] O. Trott and A. J. Olson, "AutoDock Vina: improving the speed and accuracy of docking with a new scoring function, efficient optimization, and multithreading," *Journal of Computational Chemistry*, vol. 31, no. 2, pp. 455–461, 2010.

[27] H. Chen, G. Shen, Q. Shang et al., "Plastrum testudinis extract suppresses osteoclast differentiation via the NF-κB signaling pathway and ameliorates senile osteoporosis," *Journal of Ethnopharmacology*, vol. 276, Article ID 114195, 2021.

[28] N. Weare-Regales, S. N. Hudey, and R. F. Lockey, "Practical guidance for prevention and management of glucocorticoid-induced osteoporosis for the allergist/immunologist," *Journal of Allergy and Clinical Immunology: In Practice*, vol. 9, 2021.

[29] N. Lovsin and J. Marc, "Glucocorticoid receptor regulates TNFSF11 transcription by binding to glucocorticoid responsive element in TNFSF11 proximal promoter region," *International Journal of Molecular Sciences*, vol. 22, no. 3, p. 1054, 2021.

[30] F. Hu, C. Jiang, G. Bu, Y. Fu, and Y. Yu, "Silencing long noncoding RNA colon cancer-associated transcript-1 upregulates microRNA-34a-5p to promote proliferation and differentiation of osteoblasts in osteoporosis," *Cancer Gene Therapy*, vol. 28, pp. 1150–1161, 2021.

[31] L. J. Wang and H. Q. Cai, "Let-7b downgrades CCND1 to repress osteogenic proliferation and differentiation of MC3T3-E1 cells: an implication in osteoporosis," *The Kaohsiung Journal of Medical Sciences*, vol. 36, no. 10, pp. 775–785, 2020.

[32] A. Yang, C. Yu, F. You, C. He, and Z. Li, "Mechanisms of zuogui pill in treating osteoporosis: perspective from bone marrow mesenchymal stem cells," *Evidence-Based Complementary and Alternative Medicine*, vol. 2018, Article ID 3717391, 2018.

[33] D. Liang, H. Ren, T. Qiu et al., "Extracts from plastrum testudinis reverse glucocorticoid-induced spinal osteoporosis of rats via targeting osteoblastic and osteoclastic markers," *Biomedicine & Pharmacotherapy*, vol. 82, pp. 151–160, 2016.

[34] Y. Fang, J. Liu, L. Xin et al., "Exploration of the immuno-inflammatory potential targets of xinfeng capsule in patients with ankylosing spondylitis based on data mining, network pharmacology, and molecular docking," *Evidence-based Complementary and Alternative Medicine*, vol. 2022, pp. 1–10, 2022.

[35] S. K. Wong, K. Y. Chin, and S. Ima-Nirwana, "Quercetin as an agent for protecting the bone: a review of the current evidence," *International Journal of Molecular Sciences*, vol. 21, pp. 6448–17, 2020.

[36] Z. Yang, L. Feng, M. Wang et al., "Sesamin promotes osteoporotic fracture healing by activating chondrogenesis and angiogenesis pathways," *Nutrients*, vol. 14, pp. 2106–10, 2022.

[37] Z. Yang, L. Feng, H. Wang et al., "DANCR mediates the rescuing effects of sesamin on postmenopausal osteoporosis treatment via orchestrating osteogenesis and osteoclastogenesis," *Nutrients*, vol. 13, pp. 4455–12, 2021.

[38] T. Wang, S. Li, C. Yi, X. Wang, and X. Han, "Protective role of beta-sitosterol in glucocorticoid-induced osteoporosis in rats via the RANKL/OPG pathway," *Alternative Therapies in Health & Medicine*, vol. AT015, 2022.

[39] B. Xie, Z. Zeng, S. Liao, C. Zhou, L. Wu, and D. Xu, "Kaempferol ameliorates the inhibitory activity of dexamethasone in the osteogenesis of mc3t3-E1 cells by JNK and p38-MAPK pathways," *Frontiers in Pharmacology*, vol. 12, Article ID 739326, 2021.

[40] B. F. Boyce, Y. Xiu, J. Li, L. Xing, and Z. Yao, "NF-κB-Mediated regulation of osteoclastogenesis," *Endocrinol Metab (Seoul)*, vol. 30, no. 1, pp. 35–44, 2015.

[41] Q. Zhang, X. Tang, Z. Liu et al., "Hesperetin prevents bone resorption by inhibiting RANKL-induced osteoclastogenesis and jnk mediated irf-3/c-jun activation," *Frontiers in Pharmacology*, vol. 9, p. 1028, 2018.

[42] J. Z. Wang and B. H. Zhao, "MiR-23b-3p functions as a positive factor for osteoporosis progression by targeting CCND1 in MC3T3-E1 cells," *In Vitro Cellular & Developmental Biology - Animal*, vol. 57, no. 3, pp. 324–331, 2021.

[43] E. Tonsing-Carter, K. M. Hernandez, C. R. Kim et al., "Glucocorticoid receptor modulation decreases ER-positive breast cancer cell proliferation and suppresses wild-type and mutant ER chromatin association," *Breast Cancer Research*, vol. 21, no. 1, p. 82, 2019.

[44] Q. Li, M. Wu, G. Fang et al., "MicroRNA1865p downregulation inhibits osteoarthritis development by targeting MAPK1," *Molecular Medicine Reports*, vol. 23, no. 4, p. 253, 2021.

[45] J. Yan, N. Jiang, G. Huang et al., "Deregulated MIR335 that targets MAPK1 is implicated in poor outcome of paediatric acute lymphoblastic leukaemia," *British Journal of Haematology*, vol. 163, no. 1, pp. 93–103, 2013.

[46] B. Hu, L. Chen, Y. Chen, Z. Zhang, X. Wang, and B. Zhou, "Cyanidin-3-glucoside regulates osteoblast differentiation via the ERK1/2 signaling pathway," *ACS Omega*, vol. 6, no. 7, pp. 4759–4766, 2021.

[47] L. M. Bell, M. L. Leong, B. Kim et al., "Hyperosmotic stress stimulates promoter activity and regulates cellular utilization of the serum- and glucocorticoid-inducible protein kinase (Sgk) by a p38 MAPK-dependent pathway," *Journal of Biological Chemistry*, vol. 275, no. 33, pp. 25262–25272, 2000.

[48] G. L. Firestone, J. R. Giampaolo, and B. A. O'Keeffe, "Stimulus-dependent regulation of serum and glucocorticoid inducible protein kinase (SGK) transcription, subcellular localization and enzymatic activity," *Cellular Physiology and Biochemistry*, vol. 13, no. 1, pp. 1–12, 2003.

[49] Z. Zhang, Q. Xu, C. Song et al., "Serum- and glucocorticoid-inducible kinase 1 is essential for osteoclastogenesis and promotes breast cancer bone metastasis," *Molecular Cancer Therapeutics*, vol. 19, no. 2, pp. 650–660, 2020.

[50] J. Huang, J. Peng, G. Cao et al., "Hypoxia-induced MicroRNA-429 promotes differentiation of mc3t3-E1 osteoblastic cells by mediating ZFPM2 expression," *Cellular Physiology and Biochemistry*, vol. 39, no. 3, pp. 1177–1186, 2016.

[51] C. Zhang, C. Chang, H. Gao, Q. Wang, F. Zhang, and C. Xu, "MiR-429 regulates rat liver regeneration and hepatocyte proliferation by targeting JUN/MYC/BCL2/CCND1 signaling pathway," *Cellular Signalling*, vol. 50, pp. 80–89, 2018.

[52] T. Fang, Q. Wu, L. Zhou, S. Mu, and Q. Fu, "miR-106b-5p and miR-17-5p suppress osteogenic differentiation by targeting Smad5 and inhibit bone formation," *Experimental Cell Research*, vol. 347, no. 1, pp. 74–82, 2016.

[53] Q. Wang, J. Han, P. Xu, X. Jian, X. Huang, and D. Liu, "Silencing of LncRNA SNHG16 downregulates cyclin D1 (CCND1) to abrogate malignant phenotypes in oral squamous cell carcinoma (OSCC) through upregulating miR-17-5p," *Cancer Management and Research*, vol. 13, pp. 1831–1841, 2021.

[54] Q. Zhang, X. Xiao, M. Li et al., "Acarbose reduces blood glucose by activating miR-10a-5p and miR-664 in diabetic rats," *PLoS One*, vol. 8, no. 11, Article ID e79697, 2013.

[55] M. Francis and A. Grider, "MiRNA-target interactions in osteogenic signaling pathways involving zinc via the metal regulatory element," *Biometals*, vol. 32, no. 1, pp. 111–121, 2019.

[56] H. Yang, J. Lin, J. Jiang, J. Ji, C. Wang, and J. Zhang, "miR-20b-5p functions as tumor suppressor microRNA by targeting cyclinD1 in colon cancer," *Cell Cycle*, vol. 19, no. 21, pp. 2939–2954, 2020.

[57] T. Liu, X. Li, Y. Cui et al., "Bioinformatics analysis identifies potential ferroptosis key genes in the pathogenesis of

intracerebral hemorrhage," *Frontiers in Neuroscience*, vol. 15, Article ID 661663, 2021.

[58] Z. Li, Y. Sun, S. Cao, J. Zhang, and J. Wei, "Downregulation of miR-24-3p promotes osteogenic differentiation of human periodontal ligament stem cells by targeting SMAD family member 5," *Journal of Cellular Physiology*, vol. 234, no. 5, pp. 7411–7419, 2019.

[59] Q. Bian, B. Chen, B. Weng et al., "circBTBD7 promotes immature porcine sertoli cell growth through modulating miR-24-3p/MAPK7 Axis to inactivate p38 MAPK signaling pathway," *International Journal of Molecular Sciences*, vol. 22, pp. 9385–17, 2021.

[60] Y. Wang, J. Xu, X. Zhang et al., "TNF-alpha-induced LRG1 promotes angiogenesis and mesenchymal stem cell migration in the subchondral bone during osteoarthritis," *Cell Death & Disease*, vol. 8, no. 3, Article ID e2715, 2017.

[61] Z. Liu, C. Li, P. Huang et al., "CircHmbox1 targeting miRNA-1247-5p is involved in the regulation of bone metabolism by TNF-alpha in postmenopausal osteoporosis," *Frontiers in Cell and Developmental Biology*, vol. 8, Article ID 594785, 2020.

[62] C. H. Li, Z. Z. Ma, L. L. Jian et al., "Iguratimod inhibits osteoclastogenesis by modulating the RANKL and TNF-alpha signaling pathways," *International Immunopharmacology*, vol. 90, Article ID 107219, 2021.

[63] D. Daoussis, A. P. Andonopoulos, and S. N. C. Liossis, "Wnt pathway and IL-17: novel regulators of joint remodeling in rheumatic diseases. Looking beyond the RANK-RANKL-OPG axis," *Seminars in Arthritis and Rheumatism*, vol. 39, no. 5, pp. 369–383, 2010.

[64] F. Ohori, H. Kitaura, S. Ogawa et al., "IL-33 inhibits TNF-alpha-induced osteoclastogenesis and bone resorption," *International Journal of Molecular Sciences*, vol. 21, no. 3, p. 1130, 2022.

[65] S. R. Greisen, T. W. Kragstrup, J. S. Thomsen et al., "The programmed death-1 pathway counter-regulates inflammation-induced osteoclast activity in clinical and experimental settings," *Frontiers in Immunology*, vol. 13, Article ID 773946, 2022.

[66] X. Ma, P. Su, C. Yin et al., "The roles of FoxO transcription factors in regulation of bone cells function," *International Journal of Molecular Sciences*, vol. 21, no. 3, p. 692, 2020.

[67] K. Titanji, A. Vunnava, A. Foster et al., "T-cell receptor activator of nuclear factor-κB ligand/osteoprotegerin imbalance is associated with HIV-induced bone loss in patients with higher CD4+ T-cell counts," *AIDS*, vol. 32, no. 7, pp. 885–894, 2018.

[68] H. Wu, B. Hu, X. Zhou et al., "Artemether attenuates LPS-induced inflammatory bone loss by inhibiting osteoclastogenesis and bone resorption via suppression of MAPK signaling pathway," *Cell Death & Disease*, vol. 9, no. 5, p. 498, 2018.

[69] R. Y. Kim, H. J. Yang, Y. M. Song, I. S. Kim, and S. J. Hwang, "Estrogen modulates bone morphogenetic protein-induced sclerostin expression through the Wnt signaling pathway," *Tissue Engineering Part A*, vol. 21, pp. 2076–2088, 2015.

[70] P. I. Lin, Y. T. Tai, W. P. Chan, Y. L. Lin, M. H. Liao, and R. M. Chen, "Estrogen/ERα signaling axis participates in osteoblast maturation via upregulating chromosomal and mitochondrial complex gene expressions," *Oncotarget*, vol. 9, no. 1, pp. 1169–1186, 2018.

Hindawi
Evidence-Based Complementary and Alternative Medicine
Volume 2022, Article ID 3439656, 19 pages
https://doi.org/10.1155/2022/3439656

Research Article

Danggui Buxue Decoction Ameliorates Idiopathic Pulmonary Fibrosis through MicroRNA and Messenger RNA Regulatory Network

Huizhe Zhang,[1,2] Xue Wang,[1] Yanchen Shi,[1] Mengying Liu,[3] Qingqing Xia,[4] Weilong Jiang,[4] and Yufeng Zhang[4]

[1]*Nanjing University of Chinese Medicine, Nanjing, Jiangsu 210023, China*
[2]*Department of Respiratory Medicine, Yancheng Hospital of Traditional Chinese Medicine, Yancheng Hospital Affiliated to Nanjing University of Chinese Medicine, Yancheng, Jiangsu 224005, China*
[3]*Department of Pulmonary and Critical Care Medicine, Nanjing Drum Tower Hospital Clinical College of Nanjing Medical University, Nanjing, Jiangsu 210008, China*
[4]*Department of Pulmonary and Critical Care Medicine, Jiangyin Hospital of Traditional Chinese Medicine, Jiangyin Hospital Affiliated to Nanjing University of Chinese Medicine, Jiangyin, Jiangsu 214400, China*

Correspondence should be addressed to Yufeng Zhang; yufengzhang@njucm.edu.cn

Received 13 January 2022; Revised 25 March 2022; Accepted 5 April 2022; Published 26 April 2022

Academic Editor: Jun Jiang

Objective. To develop a putative microRNA (miRNA) and messenger RNA (mRNA) regulatory network of Danggui Buxue decoction's (DGBXD) amelioration of idiopathic pulmonary fibrosis (IPF). Methods. The Gene Expression Omnibus (GEO) database was used to identify differentially expressed miRNAs (DE-miRNAs) and differentially expressed mRNAs (DE-mRNAs). Using miRNet, the predicted target genes of identified DE-miRNAs were estimated, and then the target genes of DE-miRNAs in IPF were comprehensively examined. The Enrichr database was used to conduct functional enrichment and pathway enrichment. Traditional Chinese Medicine Systems Pharmacology Database and Analysis Platform (TCMSP) was employed to obtain the target genes of DGBXD as well as active compounds. A putative miRNA-mRNA regulatory network of DGBXD acting on IPF was developed by intersecting the target genes of DGBXD with the DE-miRNA target genes in IPF. A bleomycin-induced mouse model was established and used to perform histopathology as well as real-time quantitative polymerase chain reaction (qRT-PCR) analyses of some miRNA-mRNA pairs. Results. Fourteen upmodulated DE-miRNAs and six downmodulated DE-miRNAs were screened. The downstream target genes of upmodulated and downmodulated DE-miRNAs were predicted. Subsequently, 1160 upmodulated DE-mRNAs and 1427 downmodulated DE-mRNAs were identified. Then, target genes of DE-miRNAs comprising 49 downmodulated and 53 upmodulated target genes were further screened to perform functional enrichment and pathway enrichment analyses. Subsequently, 196 target genes of DGBXD were obtained from TCMSP, with six downregulated target genes and six upregulated target genes of DGBXD acting on IPF being identified. A promising miRNA-mRNA regulatory network of DGBXD acting on IPF was developed in this study. Moreover, mir-493 together with its target gene Olr1 and mir-338 together with Hif1a were further validated by qRT-PCR. Conclusion. This study proposed detailed possible processes of miRNA-mRNA modulatory axis in IPF and constructed a prospective IPF-related miRNA-mRNA modulatory network with the aim of alleviating IPF with DGBXD.

1. Introduction

Idiopathic pulmonary fibrosis (IPF) is a chronic and progressive lung condition whose characteristics include pulmonary fibrosis. The etiology of IPF remains unknown, with its pathological manifestation being usual interstitial pneumonia (UIP) [1]. IPF is more common in the elderly, but it is a rare disease with an estimated incidence of approximately 2.8–9.3 per 100,000 people in Europe and North America [2–4]. However, in China, epidemiological data

about this condition are scarce, although its incidence has significantly increased in recent years [5]. IPF cannot be cured, so the main goals of the current treatment are to delay disease progression, improve quality of life, and prolong patient survival [6]. Limited drug options are available for IPF, with pirfenidone and nintedanib having obvious curative effects, while traditional Chinese medicine (TCM) can play an integral role in managing IPF [7–10]. Nonetheless, the prognosis of patients with IPF remains dismal, with median survival duration of approximately 2–3 years from the initial diagnosis [11]. There is thus a crucial need to develop a successful treatment for IPF.

MicroRNAs (miRNAs) are endogenous, double-stranded small RNA molecules ranging in length between 20 and 24 nucleotides that do not encode proteins [12]. miRNAs play an integral role in silencing RNA and post-transcriptionally modulating the expression of genes by interacting with messenger RNA (mRNA) via the base pairs of intramolecular complementary sequences [13]. Studies have reported that a single miRNA can regulate numerous genes, while many miRNAs can also coregulate a single gene. Therefore, miRNAs are involved in myriad cellular activities, such as cell differentiation, apoptosis, proliferation, migration, and energy metabolism [14]. Furthermore, miRNAs play significant roles in organ fibrosis, particularly in IPF, potentially being correlated with disease pathogenesis [15–19].

Studies have demonstrated that TCM can modulate miRNA-mRNA networks in the treatment of different diseases [20–22]. However, to the best of our knowledge, no evidence has been reported on the use of TCM for treating IPF through regulating the miRNA-mRNA network. Recently, in a study conducted by the authors of this paper, a putative IPF-related miRNA-mRNA modulatory network was developed, which could aid in the discovery of new miRNA-mRNA axes of IPF [23]. This can also promote further studies on TCM acting on IPF-related miRNA-mRNA regulatory networks.

Danggui Buxue decoction (DGBXD), which is an ancient classical formula among hundreds of thousands of TCM formulae, has been clinically used in China for over 800 years. The two herbs contained in DGBXD are Radix Astragali (RA; Huangqi in Chinese) and Radix Angelicae Sinensis (RAS; Danggui in Chinese) [24]. Recently, a series of studies on the use of DGBXD for treating IPF were conducted. The obtained results confirmed the effectiveness and safety of RA and RAS in IPF patients [25] and clarified the multipathway, multitarget, and multicomponent mechanisms by which RA and RAS act in the treatment of IPF [26, 27]. Therefore, DGBXD can effectively treat IPF by targeting multiple genes. Building on the previous reports on DGBXD- and miRNA-related studies [28, 29] and the miRNA-mRNA regulatory network that we developed earlier, this study further investigates whether DGBXD alleviates IPF by regulating the miRNA-mRNA modulatory network, which can facilitate further research of the relevant miRNA-mRNA pairs experimentally verified and the material basis by which DGBXD acts on IPF through the miRNA-mRNA modulatory network.

In this research, differentially expressed miRNAs (DE-miRNAs) between tissues of patients with IPF and tissues of healthy controls were screened for the first time using miRNA datasets and downstream target genes of the DE-miRNAs and were predicted using a network database. In addition, differentially expressed mRNAs (DE-mRNAs) between IPF and normal tissues were acquired with the aid of an IPF mRNA dataset. Moreover, target genes of DE-miRNAs in IPF were identified to conduct functional enrichment based on Gene Ontology (GO) and pathway enrichment based on the Kyoto Encyclopedia of Genes and Genomes (KEGG). Subsequently, target genes of DGBXD, as well as active compounds, were discovered. After the active target genes of DGBXD intersected with the DE-miRNA target genes in IPF, the target genes of DGBXD acting on IPF were also determined. Ultimately, a putative miRNA-mRNA regulatory network associated with the action of DGBXD on IPF was identified. The experimental verification of relevant miRNA-mRNA pairs was performed, which should facilitate further research.

2. Materials and Methods

2.1. Searching and Screening of Microarray Datasets. A search for datasets focusing on the miRNAs and mRNAs related to IPF was performed in the National Center for Biotechnology Information (NCBI) Gene Expression Omnibus (GEO) database (https://www.ncbi.nlm.nih.gov/gds/). Taking miRNA expression as an example, the retrieval strategy used in this study was as follows: {["microRNAs" (MeSH Terms) OR "microRNA" (All Fields)] AND "idiopathic pulmonary fibrosis" (All Fields)}. Datasets derived from IPF clinical patients and containing IPF-related and normal samples were screened for inclusion in this study.

2.2. Identification of DE-miRNAs. We employed the GEO2R online tool (https://www.ncbi.nlm.nih.gov/geo/geo2r/) to directly detect DE-miRNAs between IPF and normal samples in the screened miRNA datasets [30, 31]. Differentially expressed miRNAs were identified by GEO2R by comparing the IPF group with the normal group, setting $|\text{log2FoldChange (FC)}| > 1$ and adjusted (adj) p value < 0.05 as the cut-off values.

2.3. Predicting Downstream Target Genes of DE-miRNAs. The miRNet (https://www.mirnet.ca/) platform, which is an integrative platform integrating miRNAs, functions, and targets, was used for the purpose of estimating the downstream target genes of DE-miRNAs [32–34]. The DE-miRNAs that were downmodulated and upmodulated were entered into the web platform, while the data of target genes of downmodulated and upmodulated DE-miRNAs were downloaded.

2.4. Identification of DE-mRNA and DE-miRNA Target Genes in IPF. The screened IPF-related mRNA datasets were analyzed to enhance the validity of our additional analysis of

the target genes of DE-miRNAs that had been screened. Series matrix files were downloaded from the GEO database. Setting $|\log2FC| > 1$ and adj p value < 0.05 as the cut-off values, DE-mRNAs in IPF were discovered with the aid of the RGui and limma packages [35].

Then, an intersection analysis of DE-mRNAs and predicted target genes of DE-miRNAs was performed for the purpose of identifying the target genes of DE-miRNAs in IPF.

2.5. GO Functional Enrichment and KEGG Pathway Enrichment Analyses. The Enrichr database, a reliable online tool for Gene Set Enrichment Analysis (https://amp.pharm.mssm.edu/Enrichr/), was used to conduct analyses of GO functional enrichment and KEGG pathway enrichment for the target genes [36, 37]. Subsequently, we entered target genes into the web platform for the purpose of obtaining data regarding GO functional enrichment and KEGG pathway enrichment. GO functional analysis comprises three classifications: cellular component (CC), molecular function (MF), and biological process (BP). We set a p value of <0.05 to indicate a statistically significant difference.

2.6. Identification of Active Target Genes of DGBXD and Active Compounds. We used the Traditional Chinese Medicine Systems Pharmacology Database and Analysis Platform (TCMSP; https://old.tcmsp-e.com/tcmsp.php) to obtain the chemical compounds and their corresponding target genes in DGBXD (RA and RAS) [38]. Drug-likeness (DL) ≥ 0.18 and oral bioavailability (OB) $\geq 30\%$ were established as thresholds to identify the active compounds, with reference to previous studies [26, 39]. All human gene symbols were corrected to their official gene symbols with the aid of UniProt Knowledgebase (https://www.uniprot.org/) [40, 41].

2.7. Determination of Target Genes of DGBXD Acting on IPF. The target genes of the active compounds of DGBXD that overlapped with the target genes of DE-miRNAs in IPF were selected as target genes of DGBXD acting on IPF. According to their corresponding miRNAs, a potential miRNA-mRNA regulatory network of DGBXD acting on IPF was established.

2.8. Animal Experiments. We procured C57BL/6 wild-type mice from the Animal Core Facility of Nanjing Medical University (Nanjing Medical University, Nanjing, China). A total of 30 male mice ranging in age from 6 to 8 weeks, weighing 18 to 22 g, were kept in a controlled setting and fed conventional rodent chow, as well as being provided with free access to water. The mice were classified into three groups at random (n = 10 for each group): bleomycin group (Model), control group (Control), and bleomycin + DGBXD group (Treatment). For the purpose of inducing fibrosis, the mice in the model and treatment groups were administered 50 μl of bleomycin (5 mg/kg) (Nippon Kayaku Co., Ltd., Tokyo, Japan), while those in the control group received normal saline (NS) via intratracheal injection, through an endotracheal quantitative microsprayer aerosolizer (Shanghai Yuyan Instruments Co., Ltd., Shanghai, China) [42]. The day after modeling, the control and model groups were intragastrically administered NS, whereas the animals in the treatment group were administered DGBXD once a day for 3 weeks. DGBXD granules were purchased from Jiangyin Tianjiang Pharmaceutical Co., Ltd. (Jiangyin, China) (Table S1). RA and RAS were dissolved with NS at a 5 : 1 ratio. Dosages of DGBXD were set based on their clinical dosages and previous studies [43–45]. The following dosages were used: 4.68 mg/g; RA: 3.90 mg/g, and RAS: 0.78 mg/g (crude drug), calculated according to a body weight of 70 kg for adults using 30 g of RA and 6 g of RAS. Mice were anesthetized and sacrificed on day 21 for further experiments. All of the procedures were approved by the Ethics Committee for Animal Experiments of Nanjing University of Chinese Medicine (A211201).

2.9. Histopathological Analysis. On day 21 following the initial therapy, the mice were euthanized and their lungs were extracted for further examination. A 10% formaldehyde solution was used to fix the lung tissue samples, followed by embedding in paraffin and slicing into 5-μm sections. We applied hematoxylin-eosin (HE) and Masson staining to determine whether the lungs had been injured or changed in terms of their morphological appearance. The Szapiel score and Ashcroft score were used to semiquantify the histopathological changes in a blinded manner [46, 47]. The scoring standards are shown in Tables S2 and S3. The scores were assessed separately by two of the authors.

2.10. RNA Extraction, Reverse Transcription, and Real-Time Quantitative Polymerase Chain Reaction (qRT-PCR). RNAiso Plus (Takara) was used for extracting total RNA from the lung tissues of the mice. PrimeScript™ RT Master Mix (Takara) was employed to reverse-transcribe the isolated RNA into complementary DNA (cDNA). Takara's TB Green® Premix Ex Taq™ II (Takara) was applied to quantify the levels of mRNA expression, with GAPDH expression used as an internal reference. The qRT-PCR was carried out using primers with the following sequences: Olr1: forward: 5′-CAA TTT CCC ATA CCA CCT CCC-3′, reverse: 5′-AGT TCC ATT CTC CCA TAG CCA-3′; Hif1a: forward: 5′-ATT TTG GCA GCG ATG ACA CAG-3′, reverse: 5′-CTT TGG AGT TTC CGA TGA AGG TA-3′; and GAPDH: forward: 5′-GAA CGG GAA GCT CAC TGG-3′, reverse: 5′-GCC TGC TTC ACC ACC TTC T-3′. Guangzhou RiboBio Co., Ltd. (Guangzhou, China), supplied the mir-493 and mir-338 primers, and U6 small nuclear RNA (snRNA) as an internal control. In accordance with the manufacturer's instructions, miRNA qRT-PCR was conducted using the Bulge-loop™ miRNA qRT-PCR Starter Kit (Guangzhou RiboBio Co., Ltd.) [48]. Quantification of data was performed by the comparative $2-\Delta\Delta Ct$ method.

2.11. Statistical Analysis. Some statistical analyses were carried out directly using the bioinformatic tools available with the aid of the websites indicated above. Only miRNAs

Table 1: Target genes of upmodulated DE-miRNAs in IPF.

Target genes	Upregulated DE-miRNAs	Target genes	Upregulated DE-miRNAs
ZNF331	miR-31-5p	CABP4	miR-410-3p
CASKIN2	miR-31-5p	HHIP	miR-410-3p
SPRY4	miR-31-5p	RAB11FIP1	miR-410-3p
FOXD4L1	miR-31-5p	CADM2	miR-410-3p
MAPK4	miR-127-3p	FOS	miR-493-5p
PER3	miR-154-5p	OLR1	miR-493-5p
VSIG2	zmiR-154-5p	CITED2	miR-493-5p miR-493-3p
PTGDR	miR-382-5p	FREM2	miR-493-5p
FAM105 A	miR-382-5p	ID4	miR-432-5p
SYT13	miR-382-5p	KCNK16	miR-432-5p
FABP4	miR-369-5p	MOGAT1	miR-432-5p
GAB1	miR-369-5p miR-409-3p	SEC14L4	miR-432-5p
IFNG	miR-409-3p	PER2	miR-495-3p
EFR3B	miR-409-3p	DLC1	miR-495-3p
SLC26A7	miR-409-3p	GALNT8	miR-495-3p
CCDC38	miR-409-3p miR-410-3p	CCDC141	miR-495-3p
HCAR2	miR-409-3p	LIFR	miR-493-3p
KLF6	miR-410-3p	MAP2	miR-493-3p
CD55	miR-410-3p	FZD4	miR-493-3p
DUSP8	miR-410-3p	GRM3	miR-487b-3p
VEGFA	miR-410-3p miR-495-3p	ADRB1	miR-654-3p
FZD5	miR-410-3p	PKIA	miR-654-3p
ARHGAP29	miR-410-3p	CDKL2	miR-654-3p
SLC25A27	miR-410-3p	PRSS21	miR-654-3p
HEY1	miR-410-3p		

DE-miRNA: differentially expressed microRNA; IPF: idiopathic pulmonary fibrosis.

or mRNAs with $|\log2FC| > 1$ and adj p value < 0.05 were deemed to have statistical significance when differential expression analysis was performed, whether RGui or GEO2R was used. A p value < 0.05 was considered to indicate statistical significance in the GO functional enrichment and KEGG pathway enrichment analyses. GraphPad Prism (version: 8.0.2) and IBM SPSS Statistics (version: 25.0) were employed to conduct the qRT-PCR analyses in this study. One-way ANOVA was performed to conduct statistical analysis on the statistics and data assessment. A p value < 0.05 was considered to indicate statistical significance.

3. Results

3.1. Screened miRNA Datasets and Identified DE-miRNAs. A total of three microarray datasets (GSE13316, GSE27430, and GSE75647) that met the inclusion criteria mentioned above were selected for subsequent analysis. These microarray datasets contained data on IPF and normal samples. The GSE13316 dataset was based on the platform GPL6955, GSE27430 was based on the platform GPL8227, and GSE75647 was based on the platform GPL21199. The three datasets were chosen to filter DE-miRNAs between IPF and normal samples. MiRNAs were discovered directly using GEO2R by designated groups, each of which contained the miRNA expression data. Adj p value < 0.05 and $|\log2FC| > 1$ were set as the cut-off values for detecting DE-miRNAs. Figure 1 shows a volcano plot of the DE-miRNAs.

After removing duplicates, 14 upregulated DE-miRNAs in IPF (miR-127-3p, miR-654-3p, miR-409-3p, miR-487b, miR-495, miR-432, miR-369-5p, miR-410, miR-299-5p, miR-382, miR-409-5p, miR-493, miR-154, miR-31) and six downregulated DE-miRNAs in IPF (miR-30b, miR-326, miR-203, miR-338-3p, miR-375, miR-184) were detected.

3.2. Predicted Downstream Target Genes of DE-miRNAs. When predicting the downstream target genes of DE-miRNAs, we employed the miRNet database because miRNAs have the greatest potential to exert their biological effects by specifically targeting the 3′ untranslated region of mRNAs. The predicted downstream target genes of the upregulated DE-miRNAs numbered 1285 genes (Table S4), whereas those of the downregulated DE-miRNAs numbered 1411 genes (Table S5). We established a network of the upmodulated DE-miRNA-target genes as depicted in Figure 2(a), and one of the downmodulated DE-miRNA-target genes as shown in Figure 2(b).

3.3. Searched mRNA Dataset and Identified DE-mRNAs. The GEO database was searched for the purpose of obtaining datasets containing information about mRNA expression.

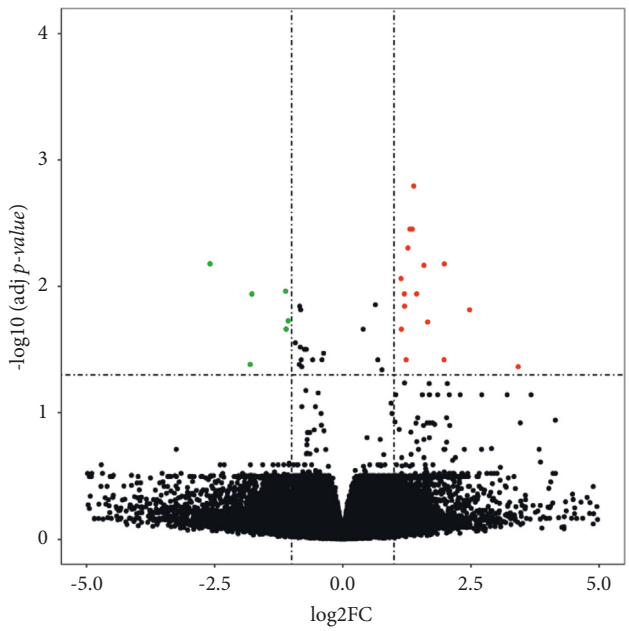

Figure 1: DE-miRNAs between IPF and normal samples. |log2FC| > 1 and adj p value < 0.05 were established as the cut-off values in the identification of DE-miRNAs. Six green dots denote downregulated DE-miRNAs and 16 red dots denote upregulated ones; black dots denote miRNAs without differential expression between IPF and normal samples. Finally, six downregulated DE-miRNAs (miR-30b, miR-326, miR-203, miR-338-3p, miR-375, miR-184) and 14 upregulated DE-miRNAs (miR-127-3p, miR-654-3p, miR-409-3p, miR-487b, miR-495, miR-432, miR-369-5p, miR-410, miR-299-5p, miR-382, miR-409-5p, miR-493, miR-154, miR-31) were identified after removing two duplicate DE-miRNAs.

Datasets based on IPF clinical patients containing data on IPF and normal samples were also included. Finally, one dataset (GSE92592) was chosen for further investigation. The platform GPL11154 served as the foundation for GSE92592.

This dataset was selected for the purpose of determining the DE-mRNAs between IPF and normal samples. A series of matrix files was obtained from the GEO database. Applying RGui and limma package to the analysis of variance, differentially expressed mRNAs were identified. |log2FC| > 1 and adj p value < 0.05 were established as the cut-off values for detecting DE-mRNAs. Finally, we identified 1160 upmodulated DE-mRNAs in IPF (Table S6) and 1427 downmodulated ones (Table S7). Figure 3 shows a volcano plot of the DE-mRNAs.

3.4. Identified DE-miRNA Target Genes in IPF. There is typically a negative correlation between the level of an miRNA and the level of mRNA expression of its target gene. A combined assessment of 1427 downmodulated DE-mRNAs and 1285 predicted target genes of upmodulated DE-miRNAs was carried out in this study. Subsequently, 49 target genes of the upmodulated DE-miRNAs were discovered (Figure 4(a), Table 1). A combined evaluation of 1160 upmodulated DE-mRNAs and 1411 predicted target genes of downmodulated DE-miRNAs was also performed. Subsequently, 53 target genes of downmodulated DE-miRNAs were discovered (Figure 4(b), Table 2).

3.5. GO Functional Enrichment and KEGG Pathway Enrichment. The identified DE-miRNA target genes were subjected to GO functional enrichment and KEGG pathway enrichment analyses, both of which were accomplished using the Enrichr database.

The findings from GO CC analysis demonstrated that the target genes of the upregulated DE-miRNAs were particularly associated with integral components of the plasma membrane, clathrin-coated endocytic vesicle membrane, clathrin-coated endocytic vesicle, clathrin-coated vesicle membrane, and tertiary granule, among others (Figure 5(a)). Meanwhile, the findings from GO MF analysis demonstrated that the target genes of upregulated DE-miRNAs were particularly related to transcription corepressor binding, PDZ domain binding, transcription cofactor binding, G-protein-coupled receptor activity, and Wnt-activated receptor activity, among others (Figure 5(b)). Finally, the findings from GO BP analysis illustrated that the target genes for the upmodulated DE-miRNAs were strongly associated with negative regulation of DNA binding, regulation of adiponectin secretion, heart morphogenesis, vascular endothelial growth factor (VEGF) signaling pathway, and positive regulation of cell migration by the VEGF signaling pathway, among others (Figure 5(c)).

The results obtained from GO CC analysis showed that the target genes of the downregulated DE-miRNAs were particularly associated with platelet alpha granule, platelet alpha granule membrane, nuclear chromosome, filopodium, and dendrite, among others (Figure 5(d)). Meanwhile, the findings from GO MF analysis demonstrated that the target genes of the downregulated DE-miRNAs were particularly linked with transcription factor activity RNA polymerase II core promoter proximal region sequence-specific binding, transcriptional activator activity RNA polymerase II core promoter proximal region sequence-specific binding, VEGF receptor 2 binding, transcriptional activator activity RNA polymerase II transcription regulatory region sequence-specific binding, and metalloendopeptidase activity, among others (Figure 5(e)). Finally, GO BP analysis showed that the target genes of the downregulated DE-miRNAs demonstrated particular links with extracellular matrix organization, positive regulation of gene expression, positive regulation of nucleic acid-templated transcription, negative regulation of neuron apoptotic process, and cellular response to cytokine stimulus, among others (Figure 5(f)).

KEGG pathway enrichment analysis was also conducted on the genes that were targeted by DE-miRNAs. The results showed that the target genes of the upmodulated DE-miRNAs were particularly associated with pathways in cancer, breast cancer, basal cell carcinoma, proteoglycans in cancer, signaling pathways regulating pluripotency of stem cells, rheumatoid arthritis, cyclic adenosine monophosphate (cAMP), interleukin 17 signaling pathway, circadian entrainment, and circadian rhythm, among others

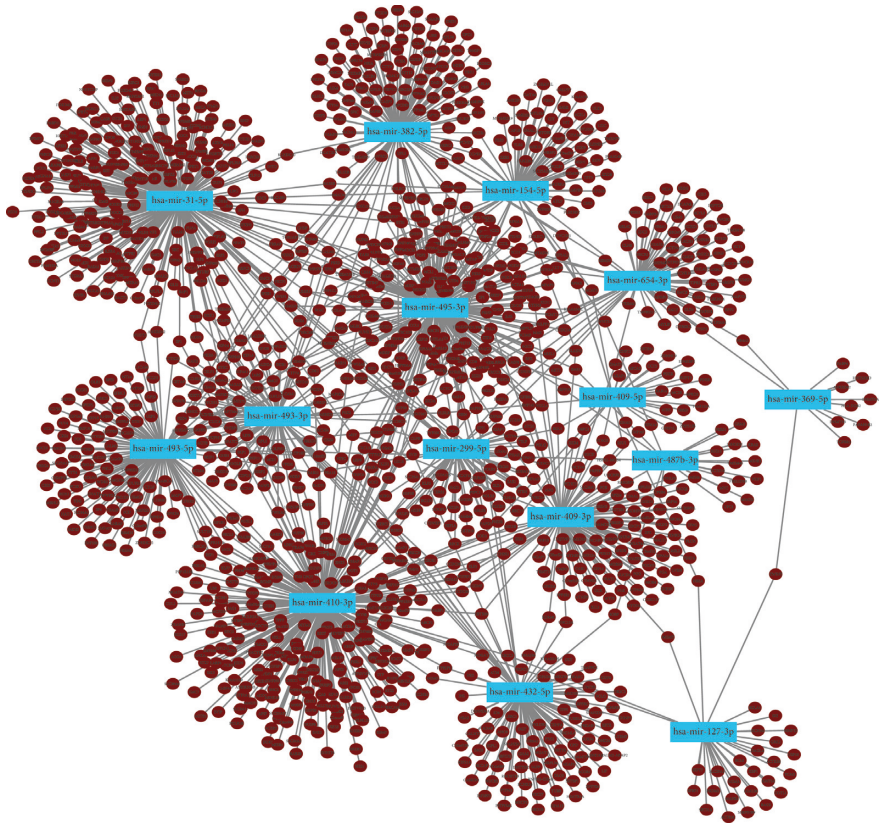

(a)

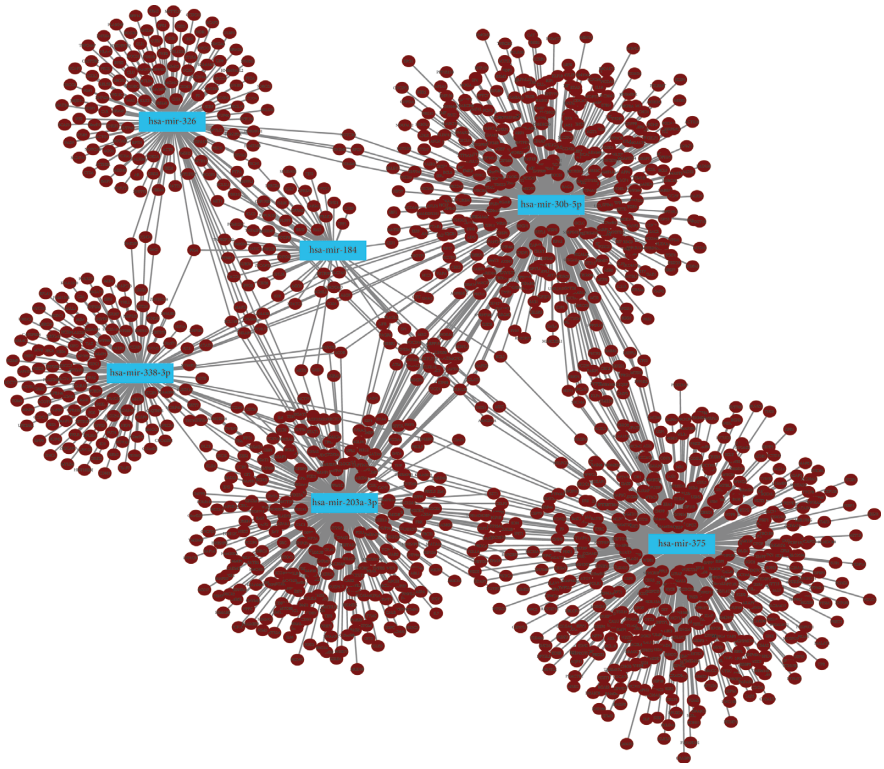

(b)

Figure 2: Predicted downstream target genes of DE-miRNAs. (a) miRNet was used for establishing a network of upmodulated DE-miRNAs and their target genes. Blue rectangles represent 15 upmodulated DE-miRNAs (miR-31 is represented in both miR-31-3p and miR-31-5p in miRNet); brown dots represent target genes. (b) miRNet was used for establishing a network of downmodulated DE-miRNAs and their target genes. Blue rectangles represent six downmodulated DE-miRNAs; brown dots represent target genes.

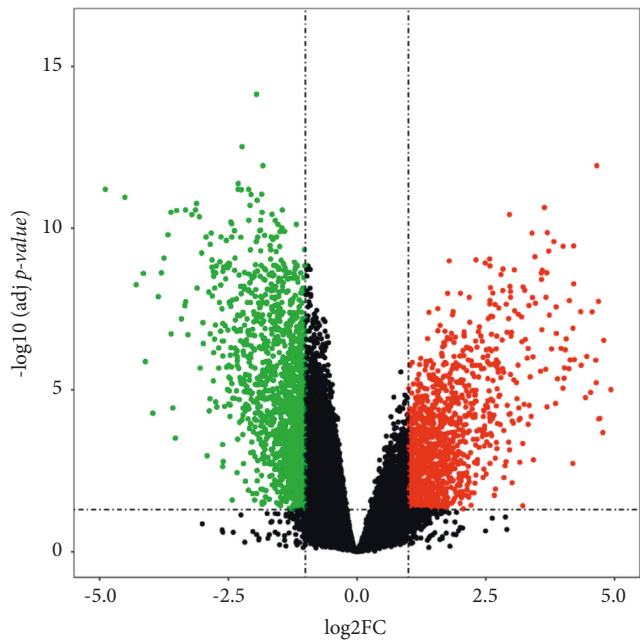

Figure 3: DE-mRNAs between IPF and normal samples. |log2FC| > 1 and adj p value < 0.05 were established as cut-off values for the identification of DE-mRNAs. Green and red dots denote the downmodulated and upmodulated mRNAs in IPF samples; black dots denote mRNAs without differential expression between IPF and normal samples.

(Figure 6(a)). The target genes for the downmodulated DE-miRNAs were found to be particularly associated with miRNAs, central carbon metabolism, transcriptional misregulation, proteoglycans in cancer, bladder cancer, leukocyte transendothelial migration, relaxin signaling pathway, fluid shear stress and atherosclerosis, signaling pathways regulating pluripotency of stem cells, and arrhythmogenic right ventricular cardiomyopathy, among others (Figure 6(b)).

3.6. Identified Active Compounds and Target Genes of DGBXD. This study identified 87 compounds in RA and 125 compounds in RAS, using TCMSP. Among these, 22 active compounds in DGBXD were predicted (20 in RA and 2 in RAS) (Table 3) upon setting the criteria of DL ≥ 0.18 and OB ≥ 30%. TCMSP was also used for determining the target genes for each of these 22 compounds (Table S6). The gene symbols were filtered using UniProt Knowledgebase, with the format "Homo sapiens" being used to identify them. Finally, we acquired a total of 196 active target genes of DGBXD (Table 4).

3.7. Identified Target Genes of DGBXD Acting on IPF. We determined those genes among the 196 active target genes of DGBXD that overlapped with the 49 target genes of upmodulated DE-miRNAs and the 53 target genes of downmodulated DE-miRNAs. This led to identification of the target genes through which DGBXD acts on IPF, namely, six downmodulated genes (Figure 7(a)) and six upmodulated ones (Figure 7(b)).

3.8. Identified Putative miRNA-mRNA Regulatory Network of DGBXD Acting on IPF. On the basis of the identified miRNA and target gene pairs (Tables 1 and 2), the relationship between the miRNAs and target genes of DGBXD through which it acts on IPF was characterized (Table 5) and a putative miRNA-mRNA regulatory network involved in the action of DGBXD on IPF was developed. According to the correlations between the active compounds of DGBXD and its target genes (Table S8), further study should be performed on potential compounds in DGBXD acting on IPF through the miRNA-mRNA regulatory network.

3.9. Experimental Validation of a Bleomycin-Induced IPF Model. To duplicate the establishment of IPF models and determine the therapeutic effects of DGBXD, HE staining was carried out to assess the pathological alterations in the various studied groups. After 21 days, extracellular matrix hyperplasia and injured alveolar structure visibly emerged, with fibroblasts appearing in the model group. On day 21, the alveolar structure was somewhat conserved in the DGBXD treatment group and the pulmonary interstitial hyperplasia was attenuated (Figure 8(a)). Additionally, the Szapiel score was significantly higher than in the control group, whereas the DGBXD treatment group was improved (Figure 8(b)). These results indicated that DGBXD could optimize the structure of the alveoli in bleomycin-induced IPF.

The extent of pulmonary fibrosis was evaluated among the groups using Masson staining. On day 21, a large number of blue-dyed collagen fibers were found in the lung interstitial fluid of the model group. Moreover, on day 21 following treatment, mild pulmonary fibrosis was observed in the DGBXD-treated group (Figure 9(a)). Additionally, the Ashcroft score was significantly higher than in the control group, whereas the DGBXD treatment group was improved (Figure 9(b)).

3.10. Validation of miRNA-mRNA Pairs in the miRNA-mRNA Regulatory Network. We used qRT-PCR to investigate the expression level of mir-493 along with its target gene Olr1, as well as the expression level of mir-338 along with its target gene Hif1a, in lung tissues. In full agreement with the predicted results, the experimental validation demonstrated that mir-493 expression was remarkably elevated in the IPF model group, compared with that in the control group, and considerably attenuated in the DGBXD treatment group compared with that in the model group (Figure 10(a)). Moreover, the mRNA expression of Olr1 was shown to have significantly decreased in the IPF model group compared with that in the control group and to be remarkably elevated in the DGBXD treatment group compared with that in the model group (Figure 10(b))

mir-338 expression was also significantly attenuated in the IPF model group compared with that in the control

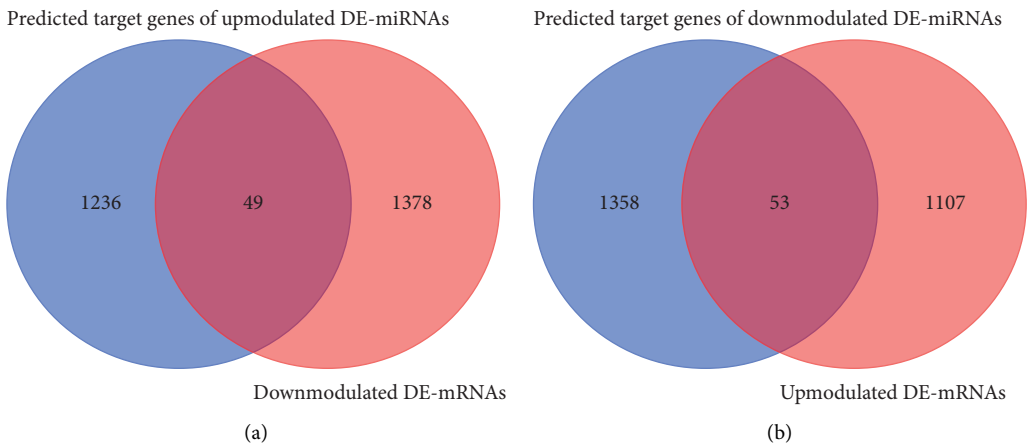

Figure 4: Identified target genes of DE-miRNAs in IPF. (a) The overlap of predicted target genes of upmodulated DE-miRNAs and downmodulated DE-mRNAs. (b) The overlap of predicted target genes of downmodulated DE-miRNAs and upmodulated DE-mRNAs.

Table 2: Target genes of downmodulated DE-miRNAs in IPF.

Target genes	Downregulated DE-miRNAs	Target genes	Downregulated DE-miRNAs
DLX5	miR-203a-3p	CRABP2	miR-375
HTR2A	miR-203a-3p	KCNN4	miR-375
IGFBP5	miR-203a-3p	OTX1	miR-375
MMP1	miR-203a-3p	PDK1	miR-375
MMP10	miR-203a-3p	RAB3B	miR-375
SIX1	miR-203a-3p miR-30b-5p	SOX2	miR-375
TOP2A	miR-203a-3p	CLDN1	miR-375
TP63	miR-203a-3p	CRLF1	miR-375
IL24	miR-203a-3p	ARNTL2	miR-375
GREM1	miR-203a-3p	CHPF	miR-375
PSAT1	miR-203a-3p	SAMD11	miR-375
MRO	miR-203a-3p miR-30b-5p	C1R	miR-326
C15orf48	miR-203a-3p	CLU	miR-326
MSI2	miR-203a-3p	HMGA2	miR-326
SPATA18	miR-203a-3p	MTHFD2	miR-326
ACTC1	miR-30b-5p	CAPN5	miR-338-3p
MYBL2	miR-30b-5p	CDH2	miR-338-3p
RRM2	miR-30b-5p	HIF1A	miR-338-3p
SLC7A5	miR-30b-5p miR-184 miR-338-3p	ITGB3	miR-338-3p
SIX4	miR-30b-5p	MAP1A	miR-338-3p
MARCH4	miR-30b-5p	MMP2	miR-338-3p
TXNDC5	miR-30b-5p	MMP9	miR-338-3p
CTHRC1	miR-30b-5p	PCDH7	miR-338-3p
FAM81 B	miR-30b-5p	NCS1	miR-338-3p
IFNE	miR-30b-5p	FJX1	miR-338-3p
TNFRSF13 C	miR-184	SCARA3	miR-338-3p
CALU	miR-375		

DE-miRNA: differentially expressed microRNA; IPF: idiopathic pulmonary fibrosis.

group and significantly elevated in the DGBXD treatment group compared with that in the model group (Figure 10(c)). Finally, the mRNA expression of Hif1a was shown to be markedly increased in the IPF model group compared with that in the control group and substantially attenuated in the DGBXD treatment group compared with that in the model group (Figure 10(d)).

4. Discussion

IPF is an interstitial disease with UIP as its main pathological manifestation. IPF cannot currently be cured and its prognosis remains poor [49, 50]. Although many related studies have been reported, the mechanism behind the occurrence and development of IPF are still not very clear.

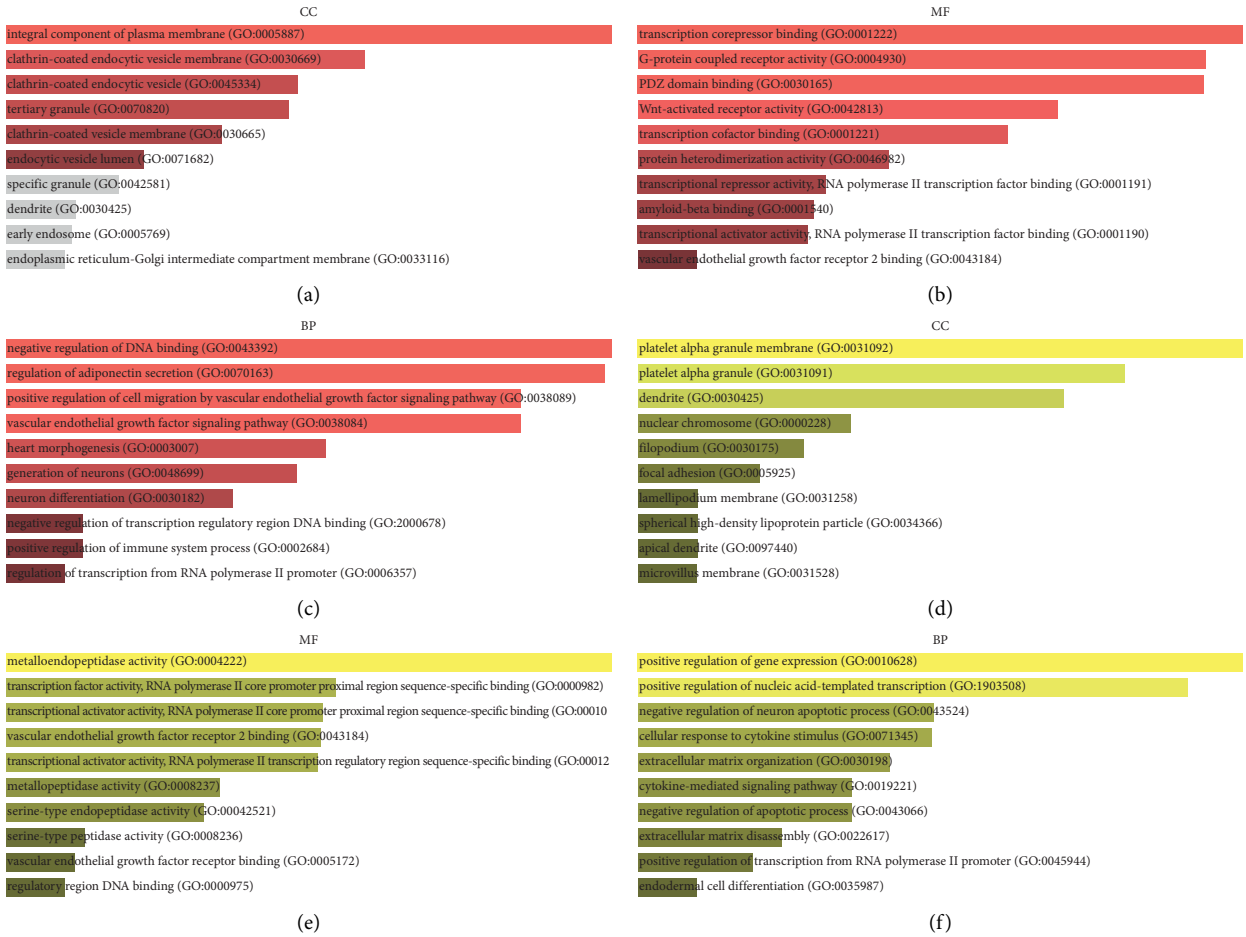

Figure 5: GO functional enrichment of target genes of DE-miRNAs in IPF. (a) The six enriched CC categories of target genes that were downmodulated. (b) The top 10 target genes with high enrichment in MF that were downmodulated. (c) The top 10 enriched BP categories of target genes that were downmodulated. (d) The top 10 target genes with high enrichment in CC that were upmodulated. (e) The top 10 target genes with high enrichment in MF that were upmodulated. (f) The top 10 enriched BP categories of target genes that were upmodulated. Sorted by p value ranking. A darker color reflects a larger p value. A gray band indicates p value > 0.05. The length indicates combined score.

Thus far, studies have shown that epithelial-mesenchymal transition (EMT) and myofibroblast differentiation may be involved in the onset and progression of IPF [51–53]. Moreover, mitochondrial dysfunction and metabolic reprogramming are considered drivers of IPF [54].

Several studies explained the expression and function of miRNA have focused on the functions of miRNAs in cell proliferative ability, apoptosis, migratory function, differentiation, and energy metabolism [15–19]. MiRNAs are also closely related to EMT and myofibroblast differentiation [55–58].

Various studies have demonstrated that miRNA-mRNA regulation performs indispensable functions in the respiratory system. According to the results of an integrative investigation of miRNA-mRNA expression in nonsmall cell lung cancer, miRNAs might be a major modulatory factor regulating basic cellular activities and cell differentiation [59, 60]. Moreover, integrative analysis of miRNA-mRNA expression indicated that miRNA-mRNA expression is associated with the influenza virus [61]. Changes in the expression profiles of miRNA-mRNA in lung tissue in a mouse model also revealed the pathophysiology of bronchopulmonary dysplasia [62].

Recently, a putative IPF-related miRNA-mRNA regulatory network was established [23]. A search of the GEO database was carried out in accordance with previously reported methods, and differential expression analysis was carried out with the aid of miRNA and mRNA microarray datasets. As a result, 14 DE-miRNAs were found to be upmodulated in IPF, whereas six DE-miRNAs were downmodulated. The majority of DE-miRNA expression patterns were in line with those observed in earlier studies. For instance, miR-31 was reported to be considerably upregulated in the serum of IPF patients, compared with the level in healthy controls [63], and the levels of miR-31 expression were found to be positively correlated with the levels of SMAD2/AKT and SMAD6 expression in patients with IPF, while transforming growth factor-β (TGF-β) was found to induce miR-31 levels in A549 cells [64]. The expression levels of miR-410, miR-382, miR-299-5p, miR-369-5p, miR-409-3p, miR-487b, miR-127-3p, miR-493,

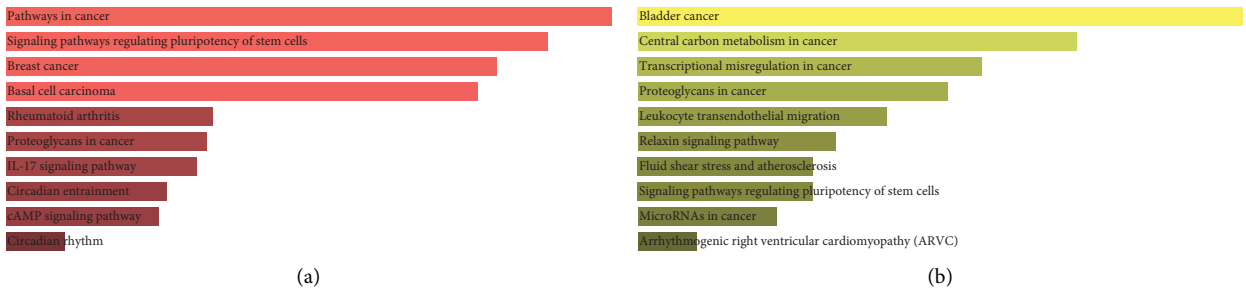

Figure 6: KEGG pathway enrichment of DE-miRNA target genes in IPF. (a) The top 10 target gene pathways with high enrichment that were downmodulated. (b) The top 10 target gene pathways with high enrichment that were upmodulated. Sorted by p value ranking. A darker color reflects a larger p value. The length indicates combined score.

Table 3: Active compounds in DGBXD determined by TCMSP.

Herb	Active compound	Compound id	OB (%)	DL
RA	Mairin	MOL000211	55.38	0.78
RA	Jaranol	MOL000239	50.83	0.29
RA	Hederagenin	MOL000296	36.91	0.75
RA	(3 S, 8 S, 9 S, 10 R, 13 R, 14 S, 17 R)-10, 13-Dimethyl-17-[(2 R, 5 S)-5-propan-2-yloctan-2-yl]-2, 3, 4, 7, 8, 9, 11, 12, 14, 15, 16, 17-dodecahydro-1h-cyclopenta [a] phenanthren-3-ol	MOL000033	36.23	0.78
RA	Isorhamnetin	MOL000354	49.60	0.31
RA	3, 9-di-O-Methylnissolin	MOL000371	53.74	0.48
RA	5′-Hydroxyiso-muronulatol-2′, 5′-di-O-glucoside	MOL000374	41.72	0.69
RA	7-O-Methylisomucronulatol	MOL000378	74.69	0.30
RA	9, 10-Dimethoxypterocarpan-3-O-β-D-glucoside	MOL000379	36.74	0.92
RA	(6aR, 11aR)-9, 10-Dimethoxy-6a, 11a-dihydro-6h-benzofurano [3, 2-c]chromen-3-ol	MOL000380	64.26	0.42
RA	Bifendate	MOL000387	31.10	0.67
RA	Formononetin	MOL000392	69.67	0.21
RA	Isoflavanone	MOL000398	109.99	0.30
RA	Calycosin	MOL000417	47.75	0.24
RA	Kaempferol	MOL000422	41.88	0.24
RA	FA	MOL000433	68.96	0.71
RA	(3R)-3-(2-Hydroxy-3, 4-dimethoxyphenyl)chroman-7-ol	MOL000438	67.67	0.26
RA	Isomucronulatol-7, 2′-di-O-glucosiole	MOL000439	49.28	0.62
RA	1, 7-Dihydroxy-3, 9-dimethoxy pterocarpene	MOL000442	39.05	0.48
RA	Quercetin	MOL000098	46.43	0.28
RAS	Beta-sitosterol	MOL000358	36.91	0.75
RAS	Stigmasterol	MOL000449	43.83	0.76

DGBXD: Danggui Buxue decoction; TCMSP: Traditional Chinese Medicine Systems Pharmacology database and analysis platform; OB: oral bioavailability; DL: drug-likeness; RA: Radix Astragali; RAS: Radix Angelicae Sinensis.

miR-409-5p, and miR-154 are also higher in IPF [65]. Moreover, the expression levels of miR-410 and TGF-β1 are high in lung tissue of fibrosis model rats [66]. Furthermore, the expression of miR-154 is upmodulated in the lungs of individuals experiencing pulmonary fibrosis [67]. TGF-β suppresses the level of miR-184 in A549 cells, elevates miR-184, and ameliorates the viability of A549 cells induced by TGF-β [64]. MiR-338 reduces EMT and delays the development of pulmonary fibrosis [68–70]. Meanwhile, miR-326 modulates the expression of TGF-β1 and alleviates lung fibrosis [71], and miR-326 suppresses the inflammatory response and enhances autophagy in pulmonary fibrosis induced by silica [72]. However, inconsistent results have been reported. One study found that the suppression of miR-495-3p could promote sphingosine-1-phosphate receptor 3 (S1PR3) expression in pulmonary epithelia and that overexpressed miR-495-3p could inhibit the S1PR3/SMAD2/SMAD3 pathway and suppress EMT [73].

After integrating DE-mRNAs and their anticipated target genes, several target genes of DE-miRNAs involved in IPF were obtained, which included 49 target genes for upmodulated DE-miRNAs and 53 target genes for downmodulated ones. Subsequently, GO functional enrichment and pathway analyses were conducted. Pathway enrichment analysis illustrated that the target genes were particularly associated with cancer-related pathways, rheumatoid arthritis, signaling pathways modulating pluripotency of stem cells, central carbon metabolism, miRNAs, transcriptional misregulation, fluid shear stress, and atherosclerosis. These functions and pathways are related to mitochondrial activity and metabolism. For instance, the gene expression programs that establish and maintain specific cell states are controlled

Table 4: Active target genes of DGBXD.

PGR	ADRA2A	OLR1	HAS2	TOP1	TOP2A
NCOA2	SLC6A2	HTR3A	GSTP1	RAF1	ABCG2
PTGS1	SLC6A3	ADRA2C	AHR	SOD1	NFE2L2
PTGS2	AKR1B1	ADRA1D	PSMD3	HIF1A	NQO1
HSP90AA1	PLAU	CHRM5	SLC2A4	RUNX1T1	PARP1
KCNH2	LTA4H	OPRD1	NR1I3	HSPA5	COL3A1
DRD1	MAOB	RXRB	INSRR	ERBB2	CXCL11
CHRM3	MAOA	KDR	DIO1	ACACA	CXCL2
CHRM1	CTRB1	MET	PPP3CA	CAV1	DCAF5
SCN5A	ADRB1	PKIA	GSTM1	MYC	CHEK2
CHRM4	NOS2	IL4	GSTM2	F3	CLDN4
ADRA1A	AR	ATP5F1B	AKR1C3	GJA1	PPARA
CHRM2	ESR2	ND6	SLPI	IL1B	HSF1
ADRA1B	DPP4	HSD3B2	MMP3	CCL2	CRP
ADRB2	CDK2	HSD3B1	EGFR	PTGER3	CXCL10
CHRNA2	CHEK1	IKBKB	VEGFA	IL8RA	CHUK
SLC6A4	PRSS1	AKT1	CCND1	PRKCB	SPP1
OPRM1	CALM1	TNFSF15	BCL2L1	BIRC5	RUNX2
GABRA1	GRIA2	AHSA1	FOS	DUOX2	RASSF1
BCL2	ADH1B	MAPK8	CDKN1A	NOS3	E2F1
BAX	LYZD1	MMP1	EIF6	HSPB1	E2F2
CASP9	ESR1	STAT1	MMP2	SULT1E1	ACPP
JUN	PPARG	CDK1	MMP9	MGAM	CTSD
CASP3	MAPK14	HMOX1	MAPK1	IL2	IGFBP3
CASP8	GSK3B	CYP3A4	IL10RB	CCNB1	IGF2
PRKCA	CCNA2	CYP1A2	EGF	PLAT	CD40LG
PON1	PYGM	CYP1A1	RB1	THBD	IRF1
MAP2	PPARD	ICAM1	IL6	SERPINE1	ERBB3
NR3C2	F7	SELE	TP63	COL1A1	PCOLCE
ADH1C	HTR	VCAM1	ELK1	IFNGR1	NPEPPS
IGHG1	ACHE	NR1I2	NFKBIA	IL1A	HK2
RXRA	RELA	CYP1B1	POR	MPO	RASA1
NCOA1	NCF1	ALOX5	ODC1		

DGBXD: Danggui Buxue decoction.

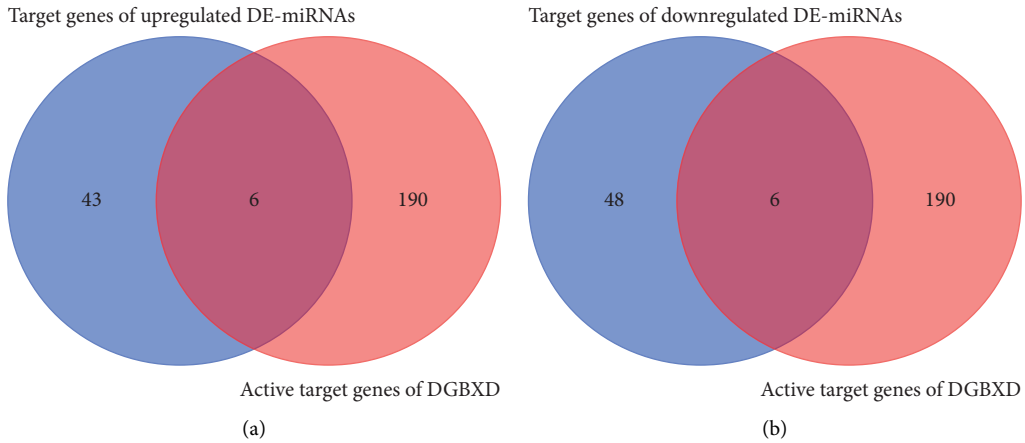

Figure 7: Identified target genes of DGBXD acting on IPF. (a) The overlap of the 196 active target genes of DGBXD with the 49 target genes of upregulated DE-miRNAs was determined, which identified six downregulated target genes of DGBXD acting on IPF. (b) The overlap of the 196 active target genes of DGBXD with the 53 target genes of downregulated DE-miRNAs was determined, which identified six upregulated target genes of DGBXD acting on IPF.

by thousands of transcription factors, cofactors, and chromatin regulators, whose misregulation can cause a broad range of diseases [74]. Metabolic reprogramming in tumors is closely related to autophagy and mitophagy [75]. Intestinal microbiota metabolism is associated with atherosclerosis [76]. The role of cancer stem cell metabolism in carcinogenesis is a major focus in cancer research [77]. Mitochondrial dysfunction is associated with the initiation and

Table 5: Target genes of DGBXD acting on IPF and corresponding miRNA.

Target genes	Corresponding miRNA	
Downregulated target genes	PKIA	miR-654-3p
	FOS	miR-493-5p
	ADRB1	miR-654-3p
	VEGFA	miR-410-3p
		miR-495-3p
	MAP2	miR-493-3p
	OLR1	miR-493-5p
Upregulated target genes	MMP2	miR-338-3p
	TOP2A	miR-203a-3p
	HIF1A	miR-338-3p
	MMP1	miR-203a-3p
	TP63	miR-203a-3p
	MMP9	miR-338-3p

DGBXD: Danggui Buxue decoction; IPF: idiopathic pulmonary fibrosis; miRNA: microRNA.

progression of atherosclerosis by elevating the production of reactive oxygen species and mitochondrial oxidative stress damage, mitochondrial dynamics dysfunction, and energy supply [78]. MiRNAs involved in mitochondrial metabolism, mitochondrial oxidative phosphorylation, electron transport chain components, lipid metabolism, and metabolic disorders are very important and closely related to mitochondrial dynamics and cancer [79]. The inhibition of dynamin-related protein 1 (DRP1) and mitochondrial fission attenuates inflammatory response in fibroblast-like synoviocytes of rheumatoid arthritis [80]. Mitochondrial fission activity is associated with high proliferation and invasiveness in some cancer cells and with self-renewal and resistance to differentiation in some stem cells [81]. Mitochondrial dynamics and dysfunction are related to mitochondrial DNA defects, excessive fission, mitochondrial retrograde signaling, and cancer progression [82]. These functions and pathways mentioned above are related to mitochondrial activity and metabolism, which suggests that the target genes of DE-miRNAs in IPF are also related to mitochondrial function and metabolism.

Some research reports have demonstrated that TCM can exert effects in regulating miRNA, mitochondrial function, and metabolism. For example, by regulating miRNA, TCM can promote liver regeneration in rat models of acute liver failure, ameliorate cyclosporin A-induced chronic nephrotoxicity, and treat coronary heart disease [20–22]. TCM has also been reported to attenuate myocardial ischemia/reperfusion injury by preserving mitochondrial function [83]. Studies have also shown that TCM can treat cardiovascular disease by protecting mitochondrial function [84]. Furthermore, metabolic reprogramming in TCM treatment of hypertension has received increasing attention [85], and metabolic reprogramming by TCM is also important for effective cancer therapy [86].

DGBXD, a TCM formulation, was first described by Li Dongyuan in the differentiation of endogenous and exogenous disorders (Nei Wai Shang Bian Huo Lun in Chinese) in 1247 CE. This herbal formula contains RA and RAS. DGBXD consists of the combination of herbs of 30 g of RA and 6 g of RAS [24]. According to TCM theory, DGBXD can be used for nourishing qi and enriching blood [87]. DGBXD can improve lung, spleen, and kidney deficiency, strengthen the blood circulation to remove blood stasis, and make qi flourishing stasis, in line with the pathological mechanism of IPF, which is also considered to be related to mitochondria and energy metabolism in modern medicine [88, 89].

A systematic review of RA and RAS in the treatment of IPF was previously performed, which confirmed their effectiveness and safety in IPF patients [25]. Network pharmacology studies were also carried out, clarifying the multipathway, multitarget, and multicomponent mechanism by which RA and RAS act in the treatment of IPF [26, 27]. These studies also provided a basis for in-depth study of the use of DGBXD to treat IPF.

Using a network pharmacology approach, 196 target genes of DGBXD, as well as 22 active compounds, were obtained in this study. The 196 active target genes of DGBXD were intersected with the target genes for DE-miRNAs, out of which 49 were upmodulated and 53 were downmodulated in IPF, resulting in the identification of six downmodulated and six upmodulated target genes of DGBXD that play certain roles in IPF. Some of these genes were associated with mitochondrial function and metabolism. Mitochondrial dysfunction is closely related to nuclear factor-κB and oxidized low-density-lipoprotein receptor 1 (OLR1) in atrial tissue during atrial fibrillation [90]. The association of OLR1 with angiotensin II type 1 receptor (AT1R) plays a crucial role in regulating mitochondrial quality control [91]. Mitochondrial dysfunction and metabolism are also closely related to hypoxia inducible factor-1α (HIF1A), mitochondrial dysfunction represses HIF1A protein synthesis, and mitochondrial defect and stabilization of HIF1A act synergistically to activate glycolysis [92, 93].

Following the analysis of the miRNA and target gene pairs mentioned above, it was discovered that there is a correlation between the miRNA and target genes of DGBXD that act on IPF. Thus, in this study, a putative miRNA-mRNA regulatory network of DGBXD acting on IPF was proposed, which includes miR-654-3p-PKIA/ADRB1, miR-493-5p-FOS/OLR1, miR-410-3p/miR-495-3p-VEGFA, and miR-493-3p-MAP2 of upregulated miRNA and downregulated gene modulatory network; miR-203a-3p-TOP2A/MMP1/TP63 and miR-338-3p-MMP2/HIF1A/MMP9 of downregulated miRNA and upregulated gene modulatory network. With regard to regulatory networks, few reports on them in human diseases have been published, and IPF-related issues have received little attention. For instance, the overexpression of secreted protein acidic and rich in cysteine (SPARC) reduces vascular endothelial growth factor-A (VEGFA) expression in NB1691 neuroblastoma cells via miR-410; in addition, the overexpression of SPARC combined with miR-410 was demonstrated to be more effective at alleviating angiogenesis, whereas the administration of miR-410 blockers attenuated the suppression of VEGFA mediated by SPARC in NB1691 cells [94]. A DNA methyltransferase inhibitor, 5-AzaC, has also been shown to increase miR-495 expression, while decreasing the

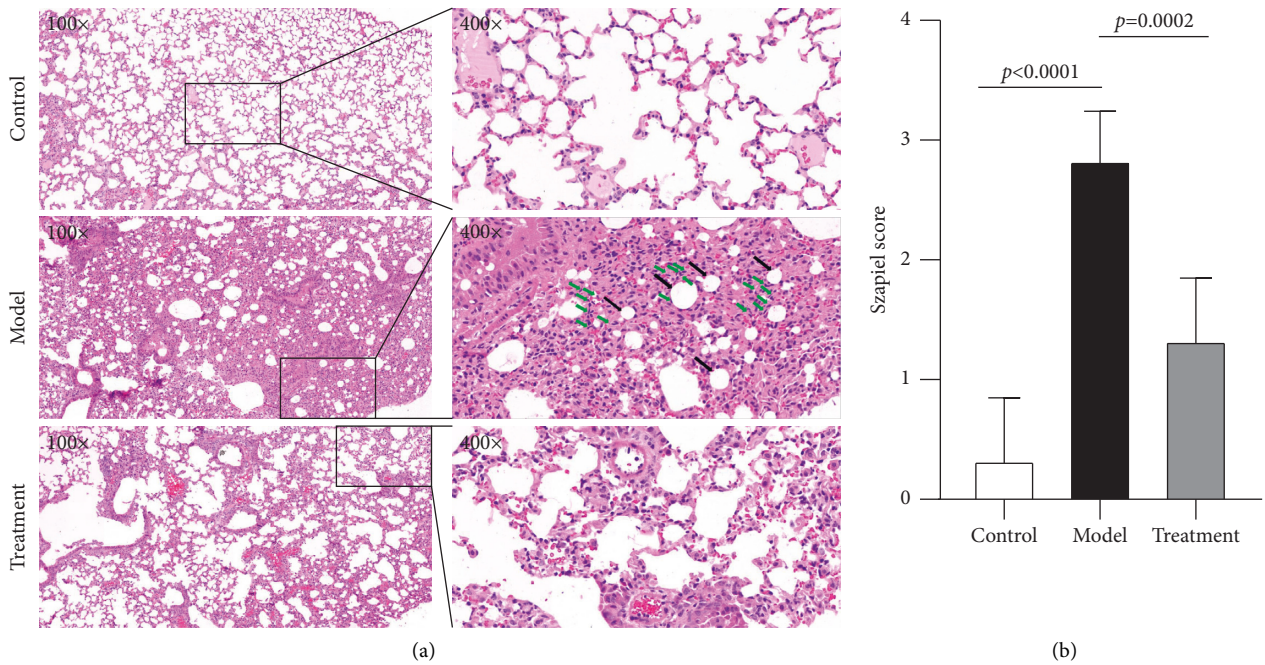

Figure 8: HE staining of lung samples. (a) On day 21, extracellular matrix proliferation and injured alveolar structure emerged visibly (black arrow), while fibroblasts (green arrow) appeared in the model group. The DGBXD treatment group exhibited slight preservation of alveolar structure and suppression of pulmonary interstitial hyperplasia on day 21. (b) Assessment by the Szapiel score. The Szapiel score was significantly higher than in the control group, whereas the DGBXD treatment group was improved.

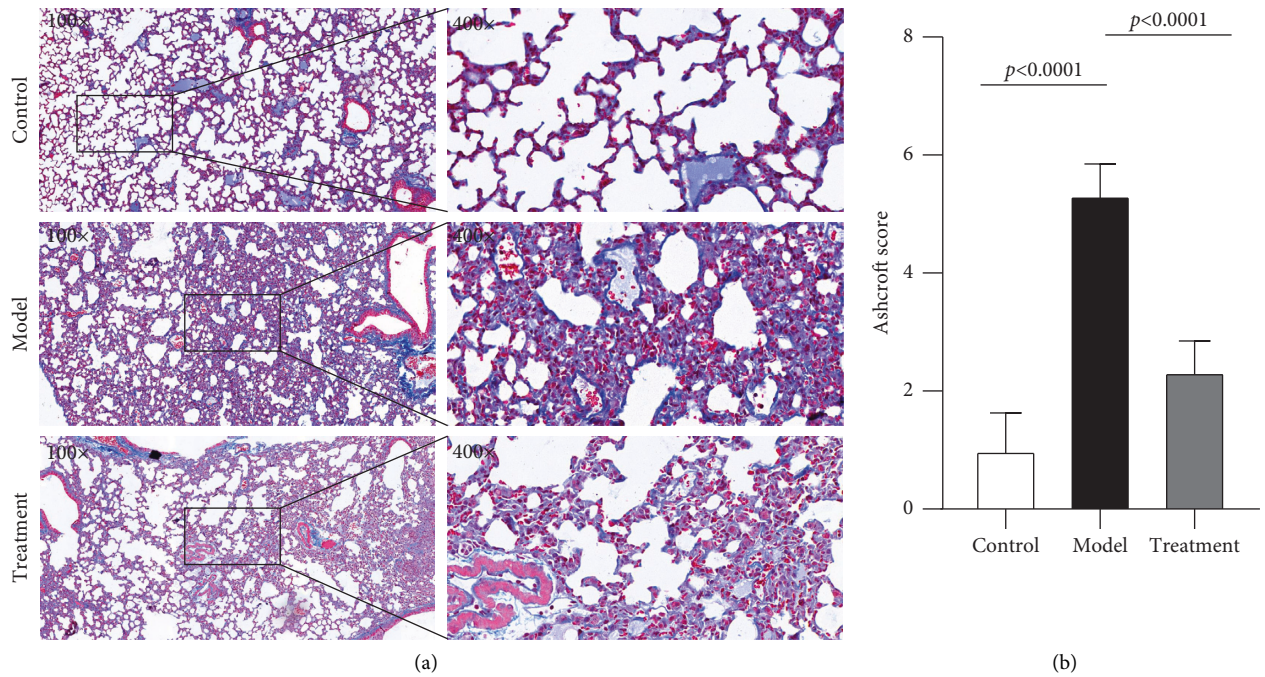

Figure 9: Masson staining of lung samples. (a) On day 21, a large number of blue-dyed collagen fibers were observed in the interstitial lung fluid of the model group. On day 21, mild lung fibrosis was observed in the DGBXD treatment groups. (b) Assessment by the Ashcroft score. The Ashcroft score was significantly higher than in the control group, whereas the DGBXD treatment group was improved.

expression of its target gene signal transducer and activator of transcription 3 (STAT3), as well as the expression of its downstream target VEGF. These anticancer characteristics of 5-AzaC have also been confirmed in breast cancer cells [95]. In the initiation and progression of nasopharyngeal carcinoma, miR-338-3p inhibits migratory and proliferative abilities by targeting HIF1A directly, which could represent a novel therapeutic target [96]. These studies may have

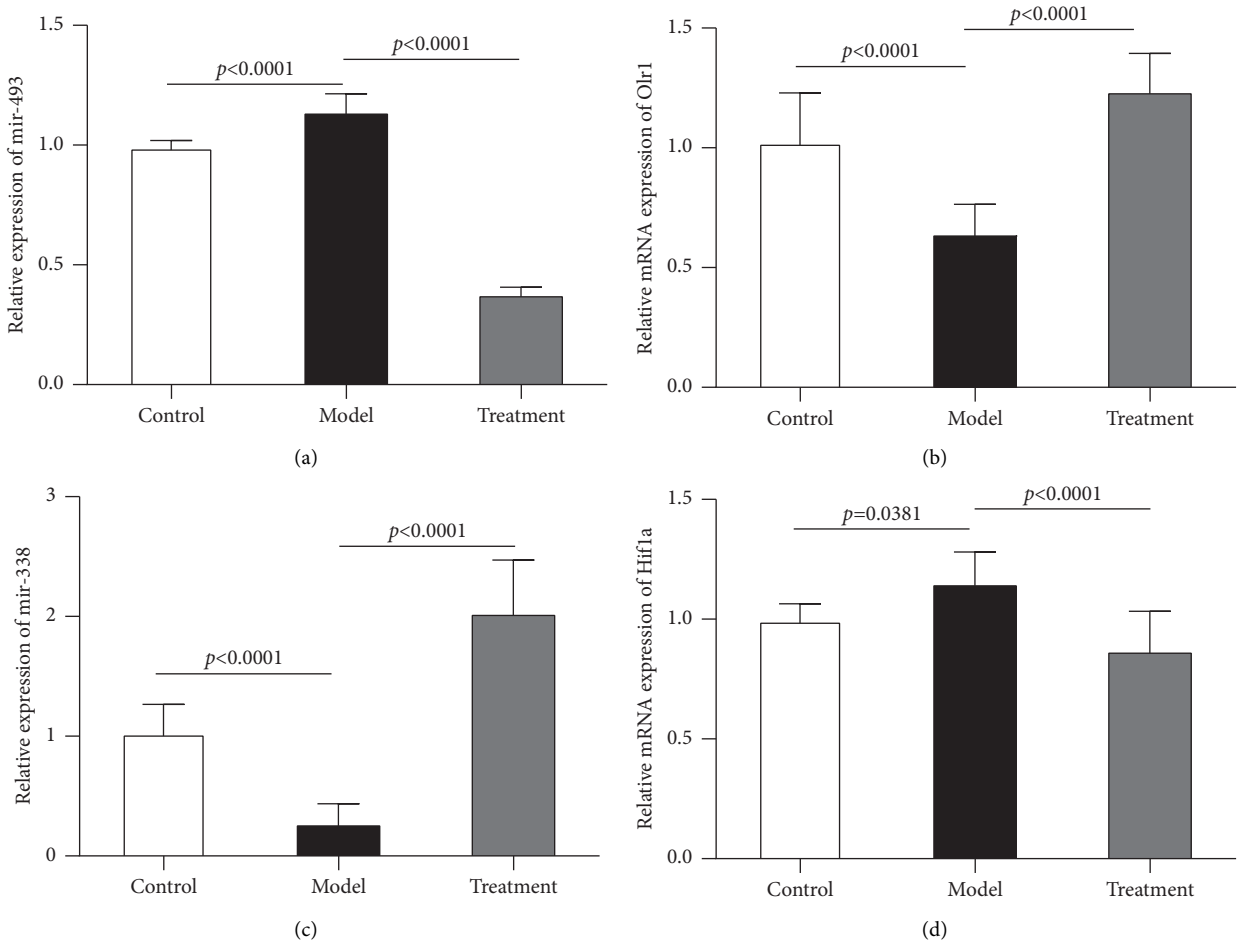

Figure 10: Validation of miRNA-mRNA pairs using qRT-PCR. (a) Substantial elevation in mir-493 expression level was observed in the model group in contrast with that in the control group. Nevertheless, considerable attenuation in mir-493 expression was observed in the treatment group compared with that in the model group. (b) The mRNA expression of *Olr1* was dramatically attenuated in the model group in comparison with that in the control group, whereas it was substantially elevated in the treatment group compared with that in the model group, with a statistically significant difference. (c) mir-338 expression was shown to undergo significant attenuation in the model group compared with that in the control group, while being substantially elevated in the treatment group compared with that in the model group. (d) The Hif1a mRNA expression was found to be substantially elevated in the model group compared with that in the control group, while being substantially reduced in the treatment group compared with that in the model group.

identified the potential targets for treating related diseases. In particular, the miRNA-mRNA regulatory network of DGBXD acting on IPF warrants further research, with the aim of verifying the related potential mechanism. The majority of the miRNA-mRNA pairs included in the network established in this study and possibly leading to the pathophysiology of IPF have not previously been explored, so studies of them are required to investigate and discover novel disease processes and treatment targets.

On the basis of previous animal model studies of the action of DGBXD on IPF, the dosage of DGBXD used and the effect of DGBXD in bleomycin-induced IPF animal model are corroborative [97–101]. Then, a bleomycin-induced IPF mouse model was duplicated, and the dosage of DGBXD intragastrically administered was calculated according to a body weight of 70 kg for adults using 30 g of RA and 6 g of RAS. Finally, the results of HE staining and Masson staining of lung sections confirmed the therapeutic effects of DGBXD. These results are consistent with previous animal model studies on IPF, and DGBXD clearly has an effect in bleomycin-induced IPF mice, which provides a basis for further mechanistic research.

After we replicated the IPF model for treatment with DGBXD, we primarily performed qRT-PCR validation of the abovementioned miRNA-mRNA pairs. Not unnaturally, genes associated with mitochondrial function and metabolism could be investigated for the first time. The expression level of mir-493 along with its target gene *Olr1* and the expression level of miR-338 along with its target gene Hif1a were explored in lung tissues by qRT-PCR. mir-493 expression was substantially upmodulated in IPF groups, whereas the gene Olr1 was downregulated, and mir-338 expression was substantially downmodulated in the IPF group along with the upregulation of Hif1a. In addition, mir-493 expression was remarkably attenuated in the DGBXD groups along with an increase in Olr1, whereas mir-

338 expression was considerably elevated in the DGBXD groups along with a decrease in Hif1a. These validation results are consistent with the regulatory network that we established, which is very important and meaningful. These miRNA-mRNA pairs associated with mitochondrial dysfunction and metabolic reprogramming could thus be prioritized for further investigation in basic research. According to the active compounds previously obtained, an HIF1A-associated compound is quercetin, and an OLR1-associated compound is isorhamnetin, which can provide a reference regarding the mechanism by which DGBXD acts on IPF through the miRNA-mRNA regulatory network.

Although a putative miRNA-mRNA regulatory network of DGBXD acting on IPF has been developed in this study, this work had several limitations. First, the IPF-related miRNA and mRNA microarray datasets used were mainly from the GEO database, whereas the other databases have less-relevant datasets. The number and sample size of the microarray datasets included in this study may thus have been insufficient, although we collected miRNA and mRNA microarray datasets as comprehensively as possible from the GEO database. Nonetheless, each dataset contains raw data from relevant clinical studies and a single dataset can display all of the obtained miRNA- or mRNA-related information, and these microarray datasets are also complete and reliable. Second, employing TCMSP, we successfully identified the active chemicals as well as the target genes in RA and RAS. However, the data collection method was not exhaustive and the criteria for screening for active chemicals could potentially have led to bias, but TCMSP is currently the most-extensive accessible database and most of the common active chemicals and target genes in RA and RAS in the network database can be identified in TCMSP. In fact, part of the active chemicals and target genes in RA and RAS may be missed including some active chemicals through quality control index of RA and RAS in Chinese Pharmacopoeia. Therefore, although we established the potential miRNA-mRNA regulatory network through the network database, some of the miRNA-mRNA pairs may have been missed for the above reasons. However, our purpose in this study was to find potential miRNA-mRNA pairs involved in DGBXD acting on IPF from the predictions and then perform validation. Overall, the established miRNA-mRNA regulatory network of DGBXD acting on IPF in this study is still reliable and significant, especially the experimentally validated miRNA-mRNA pairs. Finally, because we further validated the gene expression and miRNA-mRNA pairs in the regulatory network using an IPF mouse model, the validated miRNA-mRNA pairs for specific deep mechanisms require further investigation. In addition, further clinical research is required to validate the regulatory network, as well as its relationships to clinical efficacy and prognosis.

5. Conclusion

This study revealed a potential mechanism of involvement of miRNA-mRNA modulatory axes in the pathogenic mechanisms of IPF. It also developed a putative IPF-related miRNA-mRNA regulatory network through which DGBXD ameliorates IPF. Finally, relevant miRNA-mRNA pairs were experimentally verified to facilitate further research, and potential compounds in DGBXD acting on IPF through the miRNA-mRNA regulatory network can now also be further studied.

Data Availability

Data can be obtained from the corresponding author upon written request.

Conflicts of Interest

The authors declare that they have no conflicts of interest.

Authors' Contributions

HZ Zhang, Xue Wang, and YC Shi contributed equally to this work. HZ Zhang, WL Jiang, and YF Zhang conceived and designed the study and wrote the manuscript. HZ Zhang, QQ Xia, WL Jiang, and YF Zhang were responsible for data collation and performed the data analysis. HZ Zhang, Xue Wang, YC Shi, MY Liu, and YF Zhang performed the experiments. WL Jiang and YF Zhang performed supervision and project administration. HZ Zhang, Xue Wang, YC Shi, MY Liu, and YF Zhang revised the manuscript. All authors read and approved the final manuscript.

Acknowledgments

The authors thank Liwen Bianji (Edanz) (www.liwenbianji.cn) for editing the language of a draft of this manuscript. The authors express their gratitude to the researchers who previously shared microarray datasets, as well as to the producers of the web resource platforms and data processing software used in this research. This work was supported by Research Grants of Jiangyin Hospital of Traditional Chinese Medicine (202013 to WL Jiang, 202014 to YF Zhang) and Grants from the Wuxi Health Commission's Scientific Research Project (M202154 to YF Zhang, T202130 to WL Jiang).

Supplementary Materials

Table S1: DGBXD granules. Table S2: Szapiel score system. Table S3: Ashcroft score system. Table S4: predicted target genes of upregulated DE-miRNAs (n = 1285). Table S5: predicted target genes of downregulated DE-miRNAs (n = 1411). Table S6: upregulated DE-mRNAs (n = 1160). Table S7: downregulated DE-mRNAs (n = 1427). Table S8: corresponding gene symbols of RA and RAS. (*Supplementary Materials*)

References

[1] G. Raghu, M. Remy-Jardin, J. L. Myers et al., "Diagnosis of idiopathic pulmonary fibrosis An official ATS/ERS/JRS/ALAT clinical practice guideline," *American Journal of Respiratory and Critical Care Medicine*, vol. 198, no. 5, pp. e44–e68, 2018.

[2] G. Sheng, P. Chen, Y. Wei et al., "Viral infection increases the risk of idiopathic pulmonary fibrosis," *Chest*, vol. 157, no. 5, pp. 1175–1187, 2020.

[3] V. Navaratnam, K. M. Fleming, J. West et al., "The rising incidence of idiopathic pulmonary fibrosis in the UK," *Thorax*, vol. 66, no. 6, pp. 462–467, 2011.

[4] J. Hutchinson, A. Fogarty, R. Hubbard, and T. McKeever, "Global incidence and mortality of idiopathic pulmonary fibrosis: a systematic review," *European Respiratory Journal*, vol. 46, no. 3, pp. 795–806, 2015.

[5] H. Huang, X. Peng, and C. Zhong, "Idiopathic pulmonary fibrosis: the current status of its epidemiology, diagnosis, and treatment in China," *Intractable and Rare Diseases Research*, vol. 2, no. 3, pp. 88–93, 2013.

[6] S. Cerri, M. Monari, A. Guerrieri et al., "Real-life comparison of pirfenidone and nintedanib in patients with idiopathic pulmonary fibrosis: a 24-month assessment," *Respiratory Medicine*, vol. 159, Article ID 105803, 2019.

[7] C. Aravena, G. Labarca, C. Venegas, A. Arenas, and G. Rada, "Pirfenidone for idiopathic pulmonary fibrosis: a systematic review and meta-analysis," *PLoS One*, vol. 10, no. 8, Article ID e0136160, 2015.

[8] C. J. Ryerson, M. Kolb, L. Richeldi et al., "Effects of nintedanib in patients with idiopathic pulmonary fibrosis by GAP stage," *ERJ Open Research*, vol. 5, no. 2, 2019.

[9] Q. Wu, Y. Zhou, F.-c. Feng, and X.-m. Zhou, "Effectiveness and safety of Chinese medicine for idiopathic pulmonary fibrosis: a systematic review and meta-analysis," *Chinese Journal of Integrative Medicine*, vol. 25, no. 10, pp. 778–784, 2019.

[10] K. Ji, J. Ma, L. Wang, N. Li, S. Dong, and L. Shi, "Efficacy and safety of traditional Chinese medicine in idiopathic pulmonary fibrosis: a meta-analysis," *Evidence-based Complementary and Alternative Medicine*, vol. 2020, Article ID 1752387, 11 pages, 2020.

[11] H. J. Kim, D. Perlman, and R. Tomic, "Natural history of idiopathic pulmonary fibrosis," *Respiratory Medicine*, vol. 109, no. 6, pp. 661–670, 2015.

[12] M. Baker, "MicroRNAs as biomarkers," *Nature*, vol. 464, 2010.

[13] D. P. Bartel, "Metazoan MicroRNAs," *Cell*, vol. 173, no. 1, pp. 20–51, 2018.

[14] M. S. Ebert and P. A. Sharp, "Roles for microRNAs in conferring robustness to biological processes," *Cell*, vol. 149, no. 3, pp. 515–524, 2012.

[15] Q. Fu, Z. Lu, X. Fu, S. Ma, and X. Lu, "MicroRNA 27b promotes cardiac fibrosis by targeting the FBW7/Snail pathway," *Aging*, vol. 11, no. 24, pp. 11865–11879, 2019.

[16] H. Tu, D. Chen, C. Cai et al., "microRNA-143-3p attenuated development of hepatic fibrosis in autoimmune hepatitis through regulation of TAK1 phosphorylation," *Journal of Cellular and Molecular Medicine*, vol. 24, no. 2, pp. 1256–1267, 2020.

[17] N. Kuse, K. Kamio, A. Azuma et al., "Exosome-derived microRNA-22 ameliorates pulmonary fibrosis by regulating fibroblast-to-myofibroblast differentiation in vitro and in vivo," *Journal of Nippon Medical School*, vol. 87, no. 3, pp. 118–128, 2020.

[18] W. J. Dai, J. Qiu, J. Sun et al., "Downregulation of microRNA-9 reduces inflammatory response and fibroblast proliferation in mice with idiopathic pulmonary fibrosis through the ANO1-mediated TGF-β-Smad3 pathway," *Journal of Cellular Physiology*, vol. 234, no. 3, pp. 2552–2565, 2019.

[19] H. Bahudhanapati, J. Tan, J. A. Dutta et al., "MicroRNA-144-3p targets relaxin/insulin-like family peptide receptor 1 (RXFP1) expression in lung fibroblasts from patients with idiopathic pulmonary fibrosis," *Journal of Biological Chemistry*, vol. 294, no. 13, pp. 5008–5022, 2019.

[20] T. Wang, N. Wang, R. Zhang et al., "Jie-du-hua-yu granules promote liver regeneration in rat models of acute liver failure: miRNA-mRNA expression analysis," *Evidence-based Complementary and Alternative Medicine*, vol. 2020, pp. 1–11, 2020.

[21] C. Han, Y.-h. Jiang, W. Li, and Y. Liu, "Astragalus membranaceus and Salvia miltiorrhiza ameliorates cyclosporin A-induced chronic nephrotoxicity through the gut-kidney axis," *Journal of Ethnopharmacology*, vol. 269, Article ID 113768, 2021.

[22] F. Lin, H.-W. Chen, G.-A. Zhao et al., "Advances in research on the circRNA-miRNA-mRNA network in coronary heart disease treated with traditional Chinese medicine," *Evidence-based Complementary and Alternative Medicine*, vol. 2020, pp. 1–10, 2020.

[23] Y.-F. Zhang, L.-N. Gu, J. Qi et al., "Construction of potential idiopathic pulmonary fibrosis related microRNA and messenger RNA regulatory network," *Chinese Medical Journal*, vol. 134, no. 5, pp. 584–586, 2021.

[24] H. Q. Lin, A. G. W. Gong, H. Y. Wang et al., "Danggui Buxue tang (Astragali Radix and Angelicae sinensis Radix) for menopausal symptoms: a review," *Journal of Ethnopharmacology*, vol. 199, pp. 205–210, 2017.

[25] Y. Zhang, L. Gu, Q. Xia, L. Tian, J. Qi, and M. Cao, "Radix Astragali and Radix Angelicae sinensis in the treatment of idiopathic pulmonary fibrosis: a systematic review and meta-analysis," *Frontiers in Pharmacology*, vol. 11, p. 415, 2020.

[26] Y. Zhang, W. Jiang, Q. Xia, J. Qi, and M. Cao, "Pharmacological mechanism of Astragalus and Angelica in the treatment of idiopathic pulmonary fibrosis based on network pharmacology," *European Journal of Integrative Medicine*, vol. 32, Article ID 101003, 2019.

[27] Y. Zhang, L. Gu, J. PuYang et al., "Systems bioinformatic approach to determine the pharmacological mechanisms of Radix Astragali and Radix Angelicae sinensis in idiopathic pulmonary fibrosis," *Pharmacognosy Magazine*, vol. 17, no. 76, pp. 708–718, 2021.

[28] T. S. Ye, N. Xiang, Q. Yao, and Y. W. Zhang, "Danggui Buxue decoction protects renal function in rats with early diabetic nephropathy via miRNA-21 regulates autophagy," *Lishizhen Medicine and Materia Medica Research*, vol. 30, no. 02, pp. 282–286, 2019.

[29] Y. F. Peng, Y. Q. Zhao, Y. W. Zhang, W. Ai, and Y. Y. Yue, "Qi Gui Recipe alleviates bleomycin-induced pulmonary fibrosis in rats by intervening TGF-β/Smad signaling pathway through inhibiting miR-21," *Lishizhen Medicine and Materia Medica Research*, vol. 29, no. 09, pp. 2212–2216, 2018.

[30] G. K. Smyth, "Linear models and empirical bayes methods for assessing differential expression in microarray experiments," *Statistical Applications in Genetics and Molecular Biology*, vol. 3, no. 1, pp. 1–25, 2004.

[31] S. Davis and P. S. Meltzer, "GEOquery: a bridge between the gene expression Omnibus (GEO) and BioConductor," *Bioinformatics*, vol. 23, no. 14, pp. 1846-1847, 2007.

[32] Y. Fan, K. Siklenka, S. K. Arora, P. Ribeiro, S. Kimmins, and J. Xia, "miRNet - dissecting miRNA-target interactions and functional associations through network-based visual

analysis," *Nucleic Acids Research*, vol. 44, no. W1, pp. W135–W141, 2016.

[33] Y. Fan, M. Habib, and J. Xia, "Xeno-miRNet: a comprehensive database and analytics platform to explore xeno-miRNAs and their potential targets," *PeerJ*, vol. 6, Article ID e5650, 2018.

[34] Y. Fan and J. Xia, "miRNet-functional analysis and visual exploration of miRNA-target interactions in a network context," *Methods in Molecular Biology*, vol. 1819, pp. 215–233, 2018.

[35] M. E. Ritchie, B. Phipson, D. Wu et al., "Limma powers differential expression analyses for RNA-sequencing and microarray studies," *Nucleic Acids Research*, vol. 43, no. 7, p. e47, 2015.

[36] E. Y. Chen, C. M. Tan, Y. Kou et al., "Enrichr: interactive and collaborative HTML5 gene list enrichment analysis tool," *BMC Bioinformatics*, vol. 14, no. 1, p. 128, 2013.

[37] M. V. Kuleshov, M. R. Jones, A. D. Rouillard et al., "Enrichr: a comprehensive gene set enrichment analysis web server 2016 update," *Nucleic Acids Research*, vol. 44, no. W1, pp. W90–W97, 2016.

[38] J. Ru, P. Li, J. Wang et al., "TCMSP: a database of systems pharmacology for drug discovery from herbal medicines," *Journal of Cheminformatics*, vol. 6, no. 1, p. 13, 2014.

[39] Q. Xia, M. Liu, H. Li, L. Tian, J. Qi, and Y. Zhang, "Network pharmacology strategy to investigate the pharmacological mechanism of HuangQiXiXin decoction on cough variant asthma and evidence-based medicine approach validation," *Evidence-based Complementary and Alternative Medicine*, vol. 2020, Article ID 3829092, 15 pages, 2020.

[40] T. UniProt Consortium, "UniProt: the universal protein knowledgebase," *Nucleic Acids Research*, vol. 46, no. 5, p. 2699, 2018.

[41] W. Jiang, Y. Zhang, M. Liu et al., "A network pharmacology approach to explore the mechanism of Kangguan decoction in the treatment of coronavirus disease 2019 with preliminary verification," *TMR Integrative Medicine*, vol. 5, Article ID e21025, 2021.

[42] P. Gu, D. Wang, J. Zhang et al., "Protective function of interleukin-22 in pulmonary fibrosis," *Clinical and Translational Medicine*, vol. 11, no. 8, p. e509, 2021.

[43] T. T. X. Dong, K. J. Zhao, Q. T. Gao et al., "Chemical and biological assessment of a Chinese herbal decoction containing Radix Astragali and Radix Angelicae Sinensis: determination of drug ratio in having optimized properties," *Journal of Agricultural and Food Chemistry*, vol. 54, no. 7, pp. 2767–2774, 2006.

[44] L.-P. Zhou, K.-Y. Wong, H.-T. Yeung et al., "Bone protective effects of Danggui Buxue tang alone and in combination with tamoxifen or raloxifene in vivo and in vitro," *Frontiers in Pharmacology*, vol. 9, p. 779, 2018.

[45] S. Y. Xu, R. L. Bian, and X. Chen, *Experimental Methodology of Pharmacology*, People's Medical Publishing House, Beijing, China, 2002.

[46] S. V. Szapiel, N. A. Elson, J. D. Fulmer, G. W. Hunninghake, and R. G. Crystal, "Bleomycin-induced interstitial pulmonary disease in the nude, athymic mouse," *American Review of Respiratory Disease*, vol. 120, no. 4, pp. 893–899, 1979.

[47] T. Ashcroft, J. M. Simpson, and V. Timbrell, "Simple method of estimating severity of pulmonary fibrosis on a numerical scale," *Journal of Clinical Pathology*, vol. 41, no. 4, pp. 467–470, 1988.

[48] Y. Zhang, W. Jiang, Q. Xia et al., "Construction of a potential microRNA and messenger RNA regulatory network of acute lung injury in mice," *Scientific Reports*, vol. 12, no. 1, p. 777, 2022.

[49] J. Behr, A. Günther, F. Bonella et al., "German guideline for idiopathic pulmonary fibrosis—update on pharmacological therapies 2017," *Pneumologie*, vol. 72, no. 02, pp. 155–168, 2018.

[50] C. C. Thomson, A. Duggal, T. Bice, D. J. Lederer, K. C. Wilson, and G. Raghu, "2018 clinical practice guideline summary for practicing clinicians: diagnosis of idiopathic pulmonary fibrosis," *Annals of the American Thoracic Society*, vol. 16, no. 3, pp. 285–290, 2019.

[51] Y. Sakuma, "Epithelial-to-mesenchymal transition and its role inEGFR-mutant lung adenocarcinoma and idiopathic pulmonary fibrosis," *Pathology International*, vol. 67, no. 8, pp. 379–388, 2017.

[52] F. Salton, M. Volpe, and M. Confalonieri, "Epithelial-mesenchymal transition in the pathogenesis of idiopathic pulmonary fibrosis," *Medicina*, vol. 55, no. 4, p. 83, 2019.

[53] A. A. Gibb, M. P. Lazaropoulos, and J. W. Elrod, "Myofibroblasts and fibrosis," *Circulation Research*, vol. 127, no. 3, pp. 427–447, 2020.

[54] M. Bueno, J. Calyeca, M. Rojas, and A. L. Mora, "Mitochondria dysfunction and metabolic reprogramming as drivers of idiopathic pulmonary fibrosis," *Redox Biology*, vol. 33, Article ID 101509, 2020.

[55] S. P. Kabekkodu, D. Adiga, P. V. Jishnu, V. K. Varghese, K. Satyamoorthy, and S. P. Kabekkodu, "Role of miRNA clusters in epithelial to mesenchymal transition in cancer," *Frontiers in Bioscience*, vol. 12, no. 1, pp. 48–78, 2020.

[56] Z. Liu, X. Liang, X. Li et al., "MiRNA-21 functions in ionizing radiation-induced epithelium-to-mesenchymal transition (EMT) by downregulating PTEN," *Toxicology Research*, vol. 8, no. 3, pp. 328–340, 2019.

[57] C. Wang, H. Cao, S. Gu, C. Shi, X. Chen, and X. Han, "Expression analysis of microRNAs and mRNAs in myofibroblast differentiation of lung resident mesenchymal stem cells," *Differentiation*, vol. 112, pp. 10–16, 2020.

[58] P. Wei, Y. Xie, P. W. Abel et al., "Transforming growth factor (TGF)-β1-induced miR-133a inhibits myofibroblast differentiation and pulmonary fibrosis," *Cell Death and Disease*, vol. 10, no. 9, p. 670, 2019.

[59] R. Ma, C. Wang, J. Wang, D. Wang, and J. Xu, "miRNA-mRNA interaction network in non-small cell lung cancer," *Interdisciplinary Sciences: Computational Life Sciences*, vol. 8, no. 3, pp. 209–219, 2016.

[60] A. Najafi, M. Tavallaei, and S. M. Hosseini, "A systems biology approach for miRNA-mRNA expression patterns analysis in non-small cell lung cancer," *Cancer Biomarkers*, vol. 16, no. 1, pp. 31–45, 2016.

[61] L. Gao, J. Gao, Y. Liang et al., "Integration analysis of a miRNA-mRNA expression in A549 cells infected with a novel H3N2 swine influenza virus and the 2009 H1N1 pandemic influenza virus," *Infection, Genetics and Evolution*, vol. 74, Article ID 103922, 2019.

[62] J. Wang, J. Yin, X. Wang et al., "Changing expression profiles of mRNA, lncRNA, circRNA, and miRNA in lung tissue reveal the pathophysiological of bronchopulmonary dysplasia (BPD) in mouse model," *Journal of Cellular Biochemistry*, vol. 120, no. 6, pp. 9369–9380, 2019.

[63] G. Yang, L. Yang, W. Wang, J. Wang, J. Wang, and Z. Xu, "Discovery and validation of extracellular/circulating microRNAs during idiopathic pulmonary fibrosis disease progression," *Gene*, vol. 562, no. 1, pp. 138–144, 2015.

[64] C.-J. Wang, B.-B. Li, Y.-J. Tan, G.-M. Zhang, G.-L. Cheng, and Y.-S. Ren, "MicroRNA-31/184 is involved in transforming growth factor-β-induced apoptosis in A549 human alveolar adenocarcinoma cells," *Life Sciences*, vol. 242, Article ID 117205, 2020.

[65] J. Milosevic, K. Pandit, M. Magister et al., "Profibrotic role of miR-154 in pulmonary fibrosis," *American Journal of Respiratory Cell and Molecular Biology*, vol. 47, no. 6, pp. 879–887, 2012.

[66] H. Liu, Y. He, Z. Jiang, S. Shen, J. Mei, and M. Tang, "Prodigiosin alleviates pulmonary fibrosis through inhibiting miRNA-410 and TGF-β1/ADAMTS-1 signaling pathway," *Cellular Physiology and Biochemistry*, vol. 49, no. 2, pp. 501–511, 2018.

[67] B. C. Bernardo, S. S. Nguyen, X.-M. Gao et al., "Inhibition of miR-154 protects against cardiac dysfunction and fibrosis in a mouse model of pressure overload," *Scientific Reports*, vol. 6, no. 1, Article ID 22442, 2016.

[68] H. Zhang, X. Liu, S. Chen et al., "Tectorigenin inhibits the in vitro proliferation and enhances miR-338* expression of pulmonary fibroblasts in rats with idiopathic pulmonary fibrosis," *Journal of Ethnopharmacology*, vol. 131, no. 1, pp. 165–173, 2010.

[69] Y. Zhuang, J. Dai, Y. Wang et al., "MiR-338* targeting smoothened to inhibit pulmonary fibrosis by epithelial-mesenchymal transition," *American Journal of Tourism Research*, vol. 8, no. 7, pp. 3206–3213, 2016.

[70] Y. Zhuang, J. Dai, Y. Wang et al., "MiR-338* suppresses fibrotic pathogenesis in pulmonary fibrosis through targeting LPA1," *American Journal of Tourism Research*, vol. 8, no. 7, pp. 3197–3205, 2016.

[71] S. Das, M. Kumar, V. Negi et al., "MicroRNA-326 regulates profibrotic functions of transforming growth factor-β in pulmonary fibrosis," *American Journal of Respiratory Cell and Molecular Biology*, vol. 50, no. 5, pp. 882–892, 2014.

[72] T. Xu, W. Yan, Q. Wu et al., "MiR-326 inhibits inflammation and promotes autophagy in silica-induced pulmonary fibrosis through targeting TNFSF14 and PTBP1," *Chemical Research in Toxicology*, vol. 32, no. 11, pp. 2192–2203, 2019.

[73] L. Gong, X. Wu, X. Li et al., "S1PR3 deficiency alleviates radiation-induced pulmonary fibrosis through the regulation of epithelial-mesenchymal transition by targeting miR-495-3p," *Journal of Cellular Physiology*, vol. 235, no. 3, pp. 2310–2324, 2020.

[74] T. I. Lee and R. A. Young, "Transcriptional regulation and its misregulation in disease," *Cell*, vol. 152, no. 6, pp. 1237–1251, 2013.

[75] F. Ferro, S. Servais, P. Besson, S. Roger, J.-F. Dumas, and L. Brisson, "Autophagy and mitophagy in cancer metabolic remodelling," *Seminars in Cell and Developmental Biology*, vol. 98, pp. 129–138, 2020.

[76] T.-X. Liu, H.-T. Niu, and S.-Y. Zhang, "Intestinal microbiota metabolism and atherosclerosis," *Chinese Medical Journal*, vol. 128, no. 20, pp. 2805–2811, 2015.

[77] M. Peiris-Pagès, U. E. Martinez-Outschoorn, R. G. Pestell, F. Sotgia, and M. P. Lisanti, "Cancer stem cell metabolism," *Breast Cancer Research*, vol. 18, no. 1, p. 55, 2016.

[78] W. Peng, G. Cai, Y. Xia et al., "Mitochondrial dysfunction in atherosclerosis," *DNA and Cell Biology*, vol. 38, no. 7, pp. 597–606, 2019.

[79] F. V. Duarte, C. M. Palmeira, and A. P. Rolo, "The emerging role of MitomiRs in the pathophysiology of human disease," *Advances in Experimental Medicine and Biology*, vol. 888, pp. 123–154, 2015.

[80] X. Wang, Z. Chen, X. Fan et al., "Inhibition of DNM1L and mitochondrial fission attenuates inflammatory response in fibroblast-like synoviocytes of rheumatoid arthritis," *Journal of Cellular and Molecular Medicine*, vol. 24, no. 2, pp. 1516–1528, 2020.

[81] H. Chen and D. C. Chan, "Mitochondrial dynamics in regulating the unique phenotypes of cancer and stem cells," *Cell Metabolism*, vol. 26, no. 1, pp. 39–48, 2017.

[82] S. Srinivasan, M. Guha, A. Kashina, and N. G. Avadhani, "Mitochondrial dysfunction and mitochondrial dynamics-The cancer connection," *Biochimica et Biophysica Acta (BBA)—Bioenergetics*, vol. 1858, no. 8, pp. 602–614, 2017.

[83] X. Li, J. Liu, L. Lin et al., "Traditional Chinese medicine shuang shen ning xin attenuates myocardial ischemia/reperfusion injury by preserving of mitochondrial function," *Evidence-based Complementary and Alternative Medicine*, vol. 2014, pp. 1–10, 2014.

[84] L. Zhu, Z. Chen, K. Han et al., "Correlation between mitochondrial dysfunction, cardiovascular diseases, and traditional Chinese medicine," *Evidence-based Complementary and Alternative Medicine*, vol. 2020, pp. 1–11, 2020.

[85] M. Yang and L. Lao, "Emerging applications of metabolomics in traditional Chinese medicine treating hypertension: biomarkers, pathways and more," *Frontiers in Pharmacology*, vol. 10, p. 158, 2019.

[86] S. Wang, J.-L. Fu, H.-F. Hao, Y.-N. Jiao, P.-P. Li, and S.-Y. Han, "Metabolic reprogramming by traditional Chinese medicine and its role in effective cancer therapy," *Pharmacological Research*, vol. 170, Article ID 105728, 2021.

[87] A. G. Gong, L. M. Zhang, C. T. Lam et al., "Polysaccharide of Danggui Buxue tang, an ancient Chinese herbal decoction, induces expression of pro-inflammatory cytokines possibly via activation of NFκB signaling in cultured RAW 264.7 cells," *Phytotherapy Research*, vol. 31, no. 2, pp. 274–283, 2017.

[88] K. K. L. Kwan, Y. Huang, K. W. Leung, T. T. X. Dong, and K. W. K. Tsim, "Danggui Buxue tang, a Chinese herbal decoction containing Astragali Radix and Angelicae sinensis radix, modulates mitochondrial bioenergetics in cultured cardiomyoblasts," *Frontiers in Pharmacology*, vol. 10, p. 614, 2019.

[89] A. Gong, K. Lau, L. Zhang, H. Lin, T. Dong, and K. Tsim, "Danggui Buxue tang, Chinese herbal decoction containing Astragali Radix and Angelicae sinensis radix, induces production of nitric oxide in endothelial cells: signaling mediated by phosphorylation of endothelial nitric oxide synthase," *Planta Medica*, vol. 82, no. 05, pp. 418–423, 2016.

[90] A. Bukowska, L. Schild, G. Keilhoff et al., "Mitochondrial dysfunction and redox signaling in atrial tachyarrhythmia," *Experimental Biology and Medicine*, vol. 233, no. 5, pp. 558–574, 2008.

[91] Y. Uchikado, Y. Ikeda, Y. Sasaki, M. Iwabayashi, Y. Akasaki, and M. Ohishi, "Association of lectin-like oxidized low-density lipoprotein receptor-1 with angiotensin II type 1 receptor impacts mitochondrial quality control, offering promise for the treatment of vascular senescence," *Frontiers in Cardiovascular Medicine*, vol. 8, Article ID 788655, 2021.

[92] C.-C. Hsu, C.-H. Wang, L.-C. Wu et al., "Mitochondrial dysfunction represses HIF-1α protein synthesis through AMPK activation in human hepatoma HepG2 cells," *Biochimica et Biophysica Acta (BBA)—General Subjects*, vol. 1830, no. 10, pp. 4743–4751, 2013.

[93] A. Garedew and S. Moncada, "Mitochondrial dysfunction and HIF1α stabilization in inflammation," *Journal of Cell Science*, vol. 121, no. 20, pp. 3468–3475, 2008.

[94] J. Boyineni, S. Tanpure, M. Gnanamony et al., "SPARC overexpression combined with radiation retards angiogenesis by suppressing VEGF-A via miR-410 in human neuroblastoma cells," *International Journal of Oncology*, vol. 49, no. 4, pp. 1394–1406, 2016.

[95] Y. Chen, D. Luo, W. Tian, Z. Li, and X. Zhang, "Demethylation of miR-495 inhibits cell proliferation, migration and promotes apoptosis by targeting STAT-3 in breast cancer," *Oncology Reports*, vol. 37, no. 6, pp. 3581–3589, 2017.

[96] Y. Shan, X. Li, B. You, S. Shi, Q. Zhang, and Y. You, "MicroRNA-338 inhibits migration and proliferation by targeting hypoxia-induced factor 1α in nasopharyngeal carcinoma," *Oncology Reports*, vol. 34, no. 4, pp. 1943–1952, 2015.

[97] C. Zhao, H. Li, X. Liu et al., "Dissecting the underlying pharmaceutical mechanism of Danggui Buxue decoction acting on idiopathic pulmonary fibrosis with network pharmacology," *Traditional Medicine Research*, vol. 5, no. 4, 2020.

[98] J. Wang, H. Wang, F. Fang et al., "Danggui Buxue tang ameliorates bleomycin-induced pulmonary fibrosis by suppressing the TLR4/NLRP3 signaling pathway in rats," *Evidence-based Complementary and Alternative Medicine*, vol. 2021, pp. 1–13, 2021.

[99] J. Wang, C. Fang, S. Wang et al., "Danggui Buxue Tang ameliorates bleomycin-induced pulmonary fibrosis in rats through inhibiting transforming growth factor-beta1/Smad3/plasminogen activator inhibitor-1 signaling pathway," *Journal of Traditional Chinese Medicine*, vol. 40, no. 2, pp. 236–244, 2020.

[100] J. Gao, L.-j. Feng, Y. Huang et al., "Total glucosides of Danggui Buxue Tang attenuates bleomycin-induced pulmonary fibrosis via inhibition of extracellular matrix remodelling," *Journal of Pharmacy and Pharmacology*, vol. 64, no. 6, pp. 811–820, 2012.

[101] P. Zhao, W.-C. Zhou, D.-L. Li et al., "Total glucosides of Danggui Buxue tang attenuate BLM-induced pulmonary fibrosis via regulating oxidative stress by inhibiting NOX4," *Oxidative Medicine and Cellular Longevity*, vol. 2015, Article ID 645814, 10 pages, 2015.

Hindawi
Evidence-Based Complementary and Alternative Medicine
Volume 2022, Article ID 3182220, 11 pages
https://doi.org/10.1155/2022/3182220

Research Article

Electroacupuncture Ameliorates Tibial Fracture-Induced Cognitive Dysfunction by Elevating α7nAChR Expression and Suppressing Mast Cell Degranulation in the Hippocampus of Rats

Yudi Zhou,[1,2] **Cheng Hu**,[3] **Chenlu Mao**,[2] **Sha Li**,[2] **Yaomei Cui**,[2] **and Yanning Qian**[1]

[1]*Department of Anesthesiology, The First Affiliated Hospital of Nanjing Medical University, Nanjing, China*
[2]*Department of Anesthesiology, Jiangsu Province Hospital of Chinese Medicine, Affiliated Hospital of Nanjing University of Chinese Medicine, Nanjing, Jiangsu, China*
[3]*Affiliated Hospital of Nanjing University of Chinese Medicine, Nanjing, Jiangsu, China*

Correspondence should be addressed to Yanning Qian; yanning_qian@163.com

Received 28 January 2022; Revised 24 February 2022; Accepted 16 March 2022; Published 12 April 2022

Academic Editor: Jun Jiang

Intracerebral neuroinflammation, closely related to brain mast cell (MC) activation, performs an integral function in the pathogenic process of postoperative cognitive dysfunction (POCD). In addition to regulating cognitive activities, the alpha-7-nicotinic acetylcholine receptor (α7nAChR) engages in the progression of cognitive deficiency. In this research, we aimed to investigate how electroacupuncture (EA) affects the cognitive function in rats after tibial fracture surgery to determine whether the underlying mechanism involves the inhibition of hippocampal MC degranulation via α7nAChR. A rat model of tibial fracture surgery for inducing POCD was developed and subjected to treatment with EA or the α7nAChR antagonist α-bungarotoxin (α-BGT) and the α7nAChR agonist PHA-543613. The spatial memory tasks in the Morris Water Maze (MWM) test showed that both EA and PHA-543613-treated rats performed significantly better than untreated rats, with reduced escape latency and increased frequency of passage through the platform. However, EA and PHA-543613 intervention decreased the protein and mRNA levels of High-mobility group box-1(HMGB-1) and proinflammatory cytokines tumor necrosis factor-α (TNF-α), interleukin-1β (IL-1β) in the serum and hippocampus, respectively, by upregulating α7nAChR in the hippocampus. Furthermore, EA and PHA-543613 pretreatment reduced the number of activated MCs and suppressed neuronal apoptosis after tibial fracture surgery in the hippocampal CA1 regions, which was reversed by α-BGT. The findings indicated that EA pretreatment ameliorated POCD after tibial fracture surgery in rats by inhibiting brain MC activation and neuroinflammation mediated by the α7nAChR-dependent cholinergic anti-inflammatory system.

1. Introduction

Postoperative cognitive dysfunction (POCD), which encompasses acute delirium and long-term cognitive dysfunction, is a prevalent side effect among aged patients who have undergone a surgical operation, especially after major elective surgeries such as cardiac surgery and hip fracture repair[1, 2]. In patients aged more than 65 years old, the incidence of POCD is considerably higher at 10–20%, which is also associated with a 30-day mortality of 7–10% [3].Given the high rate of mortality in older patients with cognitive dysfunction, it has become a major health challenge owing to the rapid increase in the aging population [4]. Therefore, it is vital to investigate possible preventative or therapeutic strategies for POCD.

The mechanisms underlying POCD pathogenesis have not been comprehensively elucidated. Increasing evidence suggests that neuroinflammation plays an instrumental role in the progression of cognitive dysfunction [5]. A previous study revealed a mechanistic association between neuroinflammation and postoperative cognitive dysfunction in animal model [6]. The hippocampus is closely related to

cognitive function, and numerous studies have reported that hippocampal neuroinflammation is involved in neurocognitive disorder [7, 8]. Therefore, the inhibition of neuroinflammation may be a possible treatment strategy against cognitive dysfunction, at least to a certain extent. Cholinergic anti-inflammatory pathways perform integral function in modulating inflammation. These pathways are mainly characterized by the interactions between the alpha-7 nicotinic acetylcholine receptors (α7nAChR) on immune cells and the vagus nerve, which result in the suppression of proinflammatory cytokine release, thereby preventing excessive inflammation [9, 10]. Activation of α7nAChR exerts significant anti-inflammatory effects on neuroinflammation. α7nAChR reduces neuroinflammation, thereby serving as a potential therapeutic target [11, 12].

Acupuncture is a traditional Chinese medicine (TCM) therapeutic technique that includes the insertion of sharp, tiny needles into particular sites on the body to reestablish normal homeostasis and heal various illnesses [13]. Electroacupuncture (EA), which combines electrical stimulation and acupuncture, is effective in reducing cognitive impairment as well as increasing learning and memory function in both animal and human studies [14, 15]. Earlier research has indicated that EA pretreatment has a protective effect against cerebral ischemic injury [16, 17]. Acupuncture reduces cognitive impairments by activating the α7nAChR-mediated anti-inflammatory pathways [18]. These studies suggest that EA therapy upregulates α7nAChR, which in turn exerts beneficial effects against neurocognitive disorder.

The interplay between glial cells and neurons has been the subject of several postoperative delirium-focused investigations; however, only a limited number of studies have examined the role of brain mast cells (MCs) in cognitive disturbance. The "first responders" to neuroinflammation are precisely the MCs in the brain. An increase in the activation of MCs, accompanied by the activation of astrocytes, the release of inflammatory mediators, and the progression of cognitive impairments has been observed postoperatively [19]. Activated MCs led to inflammation of the central nervous system (CNS) and cognitive defects [20]. Furthermore, brain MCs are involved in the proinflammatory effects of high-mobility group box-1 (HMGB-1) on the CNS. Additionally, HMGB-1 caused an increase in the activation of brain MCs in the hippocampal CA1 area, resulting in a disruption of the blood–brain barrier [21]. Nevertheless, the effects of EA activation on brain MCs, as well as the possible function of α7nAChRs, have only been described in a few studies. Therefore, in the present study, we hypothesized that EA pretreatment suppressed the production of proinflammatory cytokines and the activation of MCs in the hippocampus through α7nAChRs. We tested this hypothesis in adult rats with tibial fracture.

2. Materials and Methods

2.1. Animals. One hundred and twenty adult male Sprague–Dawley rats (250–300 g in weight) were obtained from the Experimental Animal Center of Nanjing University of TCM (Nanjing, Jiangsu, China). All animal care and experimental protocols abided by the US National Institutes of Health's Guide for the Care and Use of Laboratory Animals.

2.2. Groups and Drug Treatment. Figure 1 depicts a schematic representation of the experimental procedures. To assess the mechanism of α7nAChR in inhibiting MCs activation and the cognitive improvement induced by EA pretreatment after tibial fracture surgery, 120 rats were classified into five groups in a random manner, namely control (rats did not undergo surgery), operation (tibial fracture surgery, Op), EA + Op, alpha-bungarotoxin (α-BGT)+EA + Op, and PHA-543613+Op groups. For the rats belong to the EA + Op group, EA was administered for 5 consecutive days and subjected to additional surgical intervention 1 day following the final EA pretreatment. Each group was further classified into two subgroups based on the two-time points that they were selected (1 and 3 days postoperatively) (Figures 1(a) and 1(b)).

2.3. Tibial Fracture Surgery. POCD model was induced by tibial fracture surgery as reported previously [20]. Briefly, rats were anesthetized using isoflurane (2.1%), and buprenorphine (0.1 mg/kg). They were subcutaneously injected to induce analgesia. Following the loss of the righting reflex, open tibial fracture surgery of the left posterior paw was conducted in aseptic conditions, with intramedullary fixation. The left posterior paws of the surgical animals were shaved, followed by disinfection using povidone-iodine before being used. A 7-mm G pin was introduced into the intramedullary canal by performing a median incision, followed by the removal of the periosteum and the performing of the osteotomy. Eventually, the wound area was irrigated, and the skin was subjected to suturing. For the animals belong to the control group, no surgical intervention was provided. However, equivalent dosages of isoflurane (2.1%) and buprenorphine (0.1 mg/kg) were administered. During surgery, the temperature was continued to maintain at $37 \pm 0.5^{\circ}$C with the heating blanket.

2.4. EA Pretreatment. The Baihui acupoint (GV 20) was selected for EA pretreatment in view of the fact that it lies at the point where the sagittal midline, as well as the line connecting the two ears [17]. Specifically, the rats were anesthetized, and stimulation of the GV20 was performed for half an hour at a 2/15 Hz frequency and 1 mA intensity with the aid of an electronic acupuncture treatment device (Model No. SDZ-V, Suzhou Medical Appliances Co., Ltd., Suzhou, China). A tibial fracture surgery was performed 1 day following the final EA treatment on the rats, which had been exposed to EA for a total of 5 consecutive days prior to the operation.

2.5. Intracerebroventricular Cannula Implantation. After being anesthetized, rats were placed in the stereotaxic device (RWD, Shenzhen, China) for the purpose of injecting medicines into the intracerebroventricular region. The

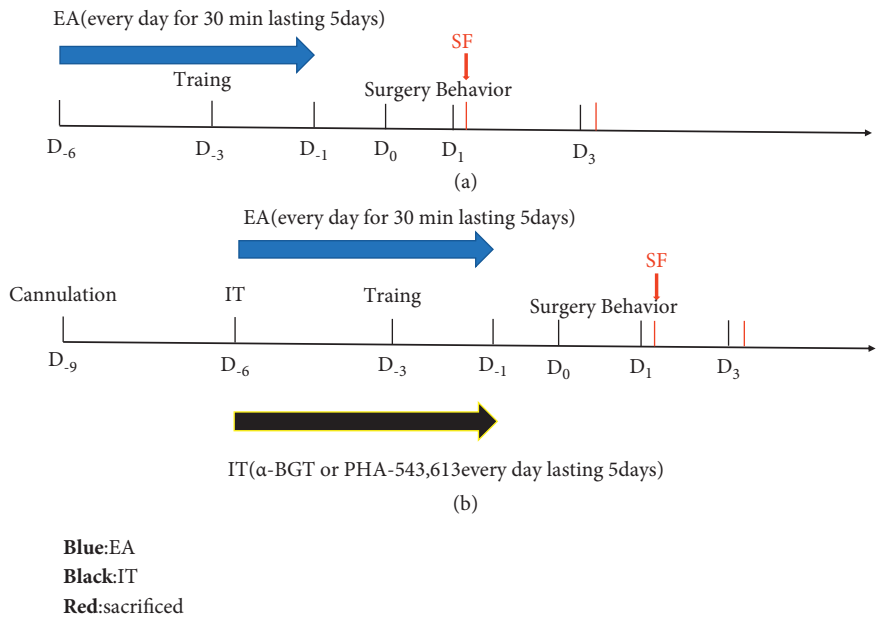

Figure 1: The schematic diagram for experimental procedures. (a) EA pretreatment for consecutive 5 days and tibial fracture surgery 24 h after the last EA treatment; the rats were sacrificed after the Morris water maze test on day 1 and 3 postoperatively. (b) Rats in the α-BGT + EA + Op group received intracerebroventricular injection of α-BGT (0.5 μg/kg dissolved in saline 10 μl,203980, Sigma, USA) for 30 min before the onset of EA for 5 days; rats in the PHA-543613+Op group received intraperitoneal injection of PHA-543613 (1.0 mg/kg dissolved in saline 1 ml, PZ0135, Sigma, USA) once a day for 5 days [22]. Rats were sacrificed after the Morris water maze test on day 1 and 3 postoperatively.

below-mentioned precise locations were used to insert a guiding cannula with 21-gauge stainless steel into the right lateral ventricle: 3.7 mm ventral, 1.5 mm right lateral, and 0.8 mm posterior to the bregma. Subsequently, the guiding cannula was fastened with dental cement and affixed to the skull with stainless steel screws that were implanted surgically. In the course of their recovery period of at least 3 days, the rats were kept separately for subsequent use in the following experiments. The guide cannula was checked daily to keep rats familiarized with the investigators. For the purpose of administering the drug solution at the desired pace, a 29-gauge injector cannula that had been attached to a microsyringe pump via a PE-20 tubing was loaded using the solution at a rate of 0.5 μL/min.

2.6. Morris Water Maze Test. As described in an earlier study [23], training of the rats was conducted on the Morris water maze four times a day for 3 days prior to surgery, and their cognitive performance was assessed on days one and three postoperatively. The navigation positioning assessment was the first of these tests. We positioned a platform that was transparent within any of the four quadrants and the top of the platform was set at 1 centimeter under the water surface. A platform was set up in the farthest quadrant from the rats, and they can discover and climb on top of it. The length of this period was reported as the escape latency. If the rat fails to locate the platform, the escape delay was subjected to a measurement at 90 seconds. The average escape latency of each rat was calculated by means of taking the mean of the four quadrants. The space exploration assessment was the second of the three tests. Then, we removed the platform from the pool and placed the rats in water in the opposite quadrant of the former test quadrant. The evaluator monitored each rat's swimming pattern for 90 seconds and counted the number of times the rats crossed over the initial platform location (platform crossing number).

2.7. Eenzyme-linked Immunosorbent Assay (ELISA). We harvested blood samples from the femoral veins of rats on days 1 and 3 postoperatively. After centrifuging blood at 3000 revolutions per minute for 15 minutes at a temperature of 4°C, the supernatant was extracted and kept at a freezing temperature of −80°C. The levels of TNF-α, IL-1β, and HMGB-1 in serum were assessed with the aid of enzyme-linked immunosorbent assay (ELISA) kits (Huamei bio, China).

2.8. qRT-PCR. TRIzol reagent (Invitrogen, USA) was employed for the purpose of extracting total RNA from hippocampi, and the extracted RNA was subsequently reverse-transcribed with the aid of the Transcription First Strand cDNA Synthesis Kit (Roche, Switzerland). Real-time polymerase chain reaction (PCR) amplification was performed based on an ABI7500 Real-time PCR Detection System (Foster City, CA, USA) with SYBR Green master mix (Applied Biosystems, USA). The GAPDH gene control values were employed to normalize the relative mRNA levels and were derived by means of the comparative cycle threshold technique.

Listed below is a list of primer sequences:

TNF-α: forward, 5′-CCGAGATGTGGAACTGGCA-GAG-3′;

reverse, 5′-CCACGAGCAGGAATGAGAAGAGG-3′.

IL-1β: forward, 5′-CAGCTTTCGACAGTGAGGAGA-3′;

reverse, 5′-TTGTCGAGATGCTGCTGTGA-3′.

HMGB-1: forward, 5′-AAGGCTGACAAGGCTC GTTATGAA-3′;

reverse, 5′-ATGCGGATTGGGCTGGTTTCTT-3′,

GAPDH: forward, 5′-AGTGCCAGCCTCGTCT-CATA-3';

reverse, 5′-GGTAACCAGGCGTCCGATAC-3′.

2.9. Western Blotting Analysis of α7nAChR. The extraction of hippocampal proteins was performed with the assistance of ice-cold RIPA lysis buffer (Beyotime, Shanghai, China), which includes a protease inhibitor (Beyotime, Shanghai, China) and a phosphatase inhibitor (Boster, Wuhan, China). As previously reported, we employed the Western blot technique to assess the expression of the α7nAChR subunit [22]. The membranes were incubated with primary antibodies against rabbit α7nAChR (Abcam, ab216485, 1 : 1000) and against mouse β-actin (Boster, Wuhan, China, BM0627, 1 : 500) then incubated with homologous secondary antibodies. Enhanced chemiluminescence (Bio-Rad) was employed with the goal of visualizing the protein bands on the membranes. Subsequently, the Image Lab program (Bio-Rad, Richmond, CA, USA) was used to scan the protein bands in each group and determine their relative density in each group. With the aid of the NIH Image J program (Bethesda, MD, USA), we successfully determined the intensity of the bands.

2.10. Toluidine Blue Staining and Cell Counting. Hippocampal sections collected from different groups were stained with 0.05% toluidine blue (TB). Subsequently, the slides were immersed in TB solution for 30 min, followed by rinse twice using distilled water, desiccation using a sequence of increasing dosages of ethanol, and placing in butyl acetate ester. The samples were embedded in the Eukitt® mounting medium under coverslips and left to air-dry throughout the night. Listed below were the degranulation criteria: a shape that has been warped, fuzzy appearance, the disappearance of purple stains, and numerous granules seen in the proximity of the cells. A light microscope (Leica Microsystems, Wetzlar, Germany) was used to visualize the CA1 region of three slices of each rat at 200× magnification (high-power field), yielding a total of 15 images per rat. The NIH Image J program (Bethesda, MD, USA) was employed to obtain the number of MC for each image (0.74-mm^2 frame), which were then averaged and transformed into cells/mm^2. Notably, the researcher performed the MCs counting in a blinded manner.

2.11. TUNEL Staining. We conducted quantitative terminal deoxynucleotidyl transferase dUTP Nick end labeling (TUNEL) staining as reported earlier for detecting the apoptosis of neuronal cells in the hippocampal tissue [22]. An optical microscope (Leica Microsystems, Wetzlar, Germany) was utilized to visualize the CA1 region of three slices of each rat, yielding a total of 15 images per rat being taken at 200× magnification (high-power field). Subsequently, the NIH Image J program (Bethesda, MD, USA) was employed for the purpose of determining the proportion of apoptotic cells in each image (0.74 mm^2 frame), which was subsequently averaged before conversion to cells/mm^2. Similarly, the researcher performed this procedure in a blinded manner.

3. Statistical Analysis

The GraphPad Prism software (version 5, GraphPad Software, San Diego, CA) was employed to perform analyses of statistical data. The results were presented as the mean ± standard error of the mean (SEM). The analyses of data were conducted by one-way or two-way analysis of variance (ANOVA), followed by the Newman–Keuls posthoc test wherever appropriate. The criterion for determining statistical significance was set at $P < 0.05$.

4. Results

4.1. EA Improved Tibial Fracture-induced Cognitive Impairment. To investigate the impacts of EA, α-BGT, and PHA-543613 pretreatment on the memory and learning function of rats undergoing surgery for tibial fracture, we employed the Morris water maze to validate the findings on days 1 and 3 following a surgical operation. As illustrated in Figures 2(a) and 2(b), on days 1 and 3 following surgery, the rats in the Op group exhibited a considerably longer escape latency time ($P < 0.01$) as well as a substantially reduced number of platform crossings ($P < 0.01$) in contrast with the control rats. Such results indicate that tibial fracture surgery can damage the memory and learning function of adult rats postoperatively. In the EA- and PHA-543613-treated groups, the latency time was substantially shortened, and the platform crossing number was considerably elevated in contrast with the Op group (day 1: $P < 0.05$, day 3: $P < 0.05$). As opposed to the rats in the EA subgroup, the rats who received EA+α-BGT displayed longer latency time as well as lower platform crossing numbers(day 3: $P < 0.05$). However, no differences were identified between the EA and EA+α-BGT groups (day 1: $P > 0.05$).

4.2. EA Attenuated Neuroinflammation and Peripheral Inflammation in a Rat after Tibial Fracture Surgery. The proinflammatory cytokines levels in the serum of rats, such as IL-1β, HMGB-1, and TNF-α, were assessed after tibial fracture surgery on days 1 and 3. In the Op group, the IL-1β, HMGB-1, and TNF-α levels were substantially elevated as opposed to those in the control group (day 1: $P < 0.01$, day 3: $P < 0.01$). Their concentrations were significantly down-regulated in both EA and PHA-543613 groups in contrast with the Op group (day 1: $P < 0.05$, day 3: $P < 0.05$). Moreover, the expression levels of these proinflammatory markers were elevated in the EA+α-BGT as opposed to the

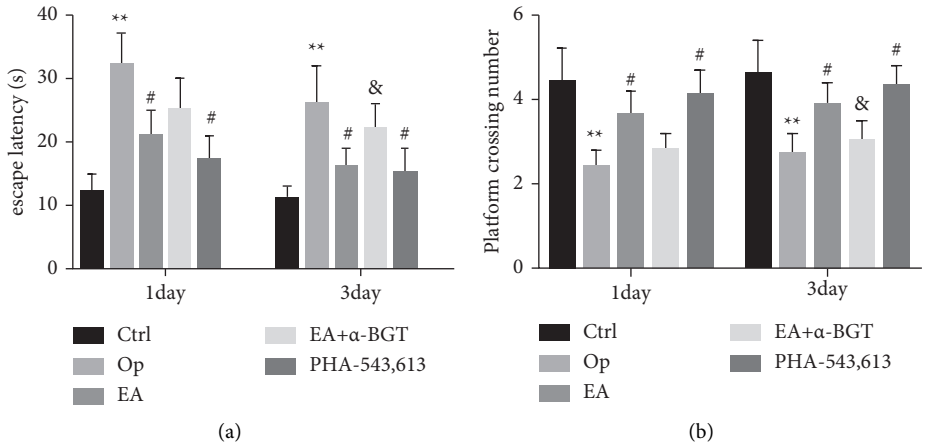

Figure 2: EA improved tibial fracture-induced cognitive impairment (a) The escape latency in rats was measured using the Morris water maze test 1 and 3 days after tibial fracture surgery. (b) The number of crossing the platform was measured using the Morris water maze 1 and 3 days after tibial fracture surgery. Graphs show the mean ± S.E.M. ($n = 12$). $^{**}P < 0.01$ versus the control group; $^{\#}P < 0.05$ versus the Op group; $^{\&}P < 0.05$ versus the EA group.

EA group (day 1: $P < 0.05$, day 3: $P < 0.05$). Nonetheless, they did not differ obviously from those of the Op group (Figures 3(a)–3(c)).

For the purpose of assessing the influence of EA on neuroinflammation, we performed qRT-PCR to determine the expression levels of *IL-1β, HMGB-1*, and *TNF-α* mRNA in the hippocampus of rats. Data analysis revealed that the expression levels of *IL-1β, HMGB-1*, and *TNF-α* mRNA in the Op group were elevated postoperatively (day 1: $P < 0.01$, day 3: $P < 0.01$) in contrast with those in the control group. Moreover, the expression levels of hippocampal *IL-1β, HMGB-1*, and *TNF-α* mRNA were remarkably inhibited in the EA- and PHA-543613-treated groups compared with the Op group at the same time points (day 1: $P < 0.05$, day 3: $P < 0.05$). The expression levels of *IL-1β, HMGB-1*, and *TNF-α* were considerably elevated in the EA+α-BGT group compared with the EA group (day 1: $P < 0.05$, day 3: $P < 0.05$). No significant difference was identified in the expression levels of *IL-1β, HMGB-1*, and *TNF-α* mRNA on days 1 and 3 postoperatively between the Op and EA+α-BGT groups ($P > 0.05$) (Figures 3(e) and 3(f)). Therefore, EA downregulated expression levels of *IL-1β, HMGB-1*, and *TNF-α* in the serum and hippocampus postoperatively, indicating that it can improve cognitive function by decreasing the levels of these inflammatory cytokines.

4.3. EA Inhibited MC Degranulation Associated with α7nAChR Activation in the Hippocampus. Brain MCs were quantified in TB-stained sections. The count of MCs in the hippocampal CA1 area in the Op group was remarkably elevated on day 1 ($P < 0.01$) and day 3 ($P < 0.01$) postoperatively as opposed to that in the controls. The count of MCs in the EA- and PHA-543613-treated groups decreased when compared with that in the Op group (day 1: $P < 0.05$, day 3: $P < 0.05$). A considerable difference was observed in the count of MCs between the EA and EA+α-BGT groups (day 1: $P < 0.05$, day 3: $P < 0.05$) (Figures 4(a) and 4(b)).

An investigation on the protein expression levels of the α7nAChR in the hippocampus was carried out using Western blotting. The levels of α7nAChR protein were substantially reduced in the hippocampus of the Op group as opposed to the controls on days 1 and 3 postoperatively ($P < 0.01$). Nonetheless, the expression levels of the hippocampal α7nAChR protein in the EA- and PHA-543613-treated groups were remarkably elevated on day 1 and 3 postoperatively ($P < 0.05$), substantially lowered in the EA+α-BGT group relative to the EA group ($P < 0.01$) and significantly elevated in the PHA-543613 group ($P < 0.01$). Furthermore, the protein expression level of α7nAChR on days 1 and 3 postoperatively between the Op and EA+α-BGT groups was found to have no significant differences ($P > 0.05$) (Figure 4(c)–4(d)). According to these findings, it was hypothesized that α7nAChR activation was involved in the prevention of MCs degranulation related to the anti-POCD role of EA.

4.4. EA Inhibited Tibial Fracture-Induced Apoptosis in the Hippocampus. On days 1 and 3 following surgery, the count of TUNEL-positive cells within the hippocampus CA1 region was remarkably elevated in the Op group in contrast with that in the control group ($P < 0.01$) and reduced in the groups treated with EA- and PHA-543613 (day 1: $P < 0.05$, day 3: $P < 0.05$). When comparing the EA and EA+α- BGT groups, significant differences were observed in the count of TUNEL-positive cells (day 1: $P < 0.05$, day 3: $P < 0.05$). The above data revealed that pretreatment with EA reduced apoptosis in the hippocampus following tibial fracture surgical procedure and that the protective function of EA pretreatment was reversed by the α7nAChR antagonist α-BGT (Figures 5(a) and 5(b)).

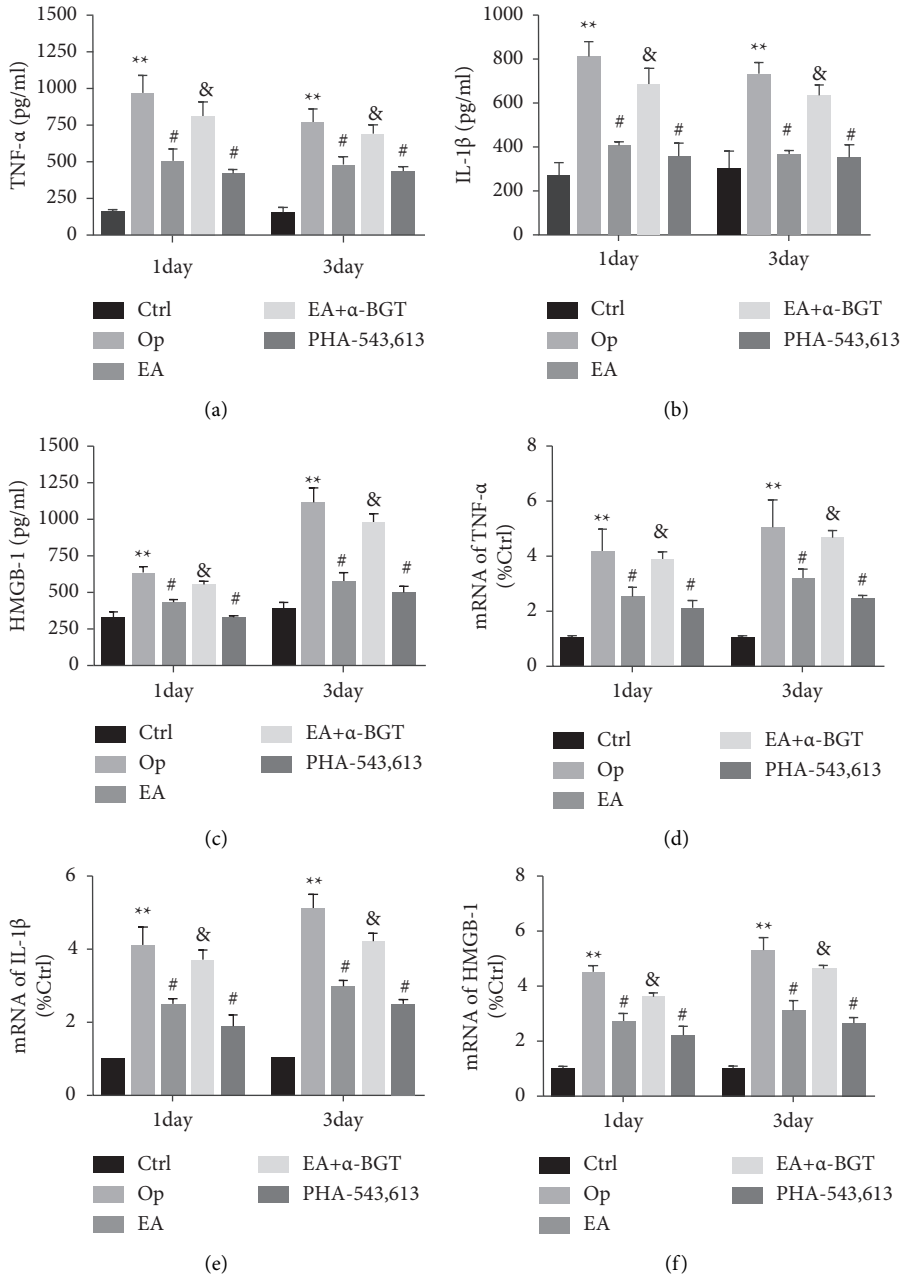

Figure 3: EA attenuated neuroinflammation and peripheral inflammation in rats after tibial fracture surgery. The serum TNF-α, IL-1β, and HMGB-1 levels were measured using ELISA on day 1 and 3 postoperatively (a–c). The mRNA expression of TNF-α, IL-1β, and HMGB-1 in the hippocampus on day 1 and 3 postoperatively was determined using real-time PCR (d–f). Graphs show the mean ± S.E.M. ($n = 6$). $^{**}P < 0.01$ versus the control group; $^{\#}P < 0.05$ versus the Op group; $^{\&}P < 0.05$ versus the EA group.

5. Discussion

MCs play a pivotal role in the pathophysiology of CNS-related diseases such as stroke, neurodegenerative disease, brain tumors, and traumatic brain injury [24]. Furthermore, the production of MC activation-dependent inflammatory mediators augments neuroinflammation. In this study, we demonstrated that brain MCs were involved in tibial fracture-induced cognitive impairment and that EA-activated cholinergic neuroimmune interaction via α7nAChRs on brain MCs, which perform an integral function in controlling neuroinflammation and peripheral inflammation. Additionally, EA pretreatment improved tibial fracture-induced cognitive impairment in rats.

A previous study suggested that tibial fracture surgery could effectively simulate the conditions of POCD in rats [25]. The Morris water maze test is a frequently utilized tool to assess spatial memory and learning in mice, and it is a highly reliable method of cognitive assessment [26]. In this study, the escape platform was stable during the test. The hippocampus-dependent spatial reference memory and learning function were assessed in the rats. Our results

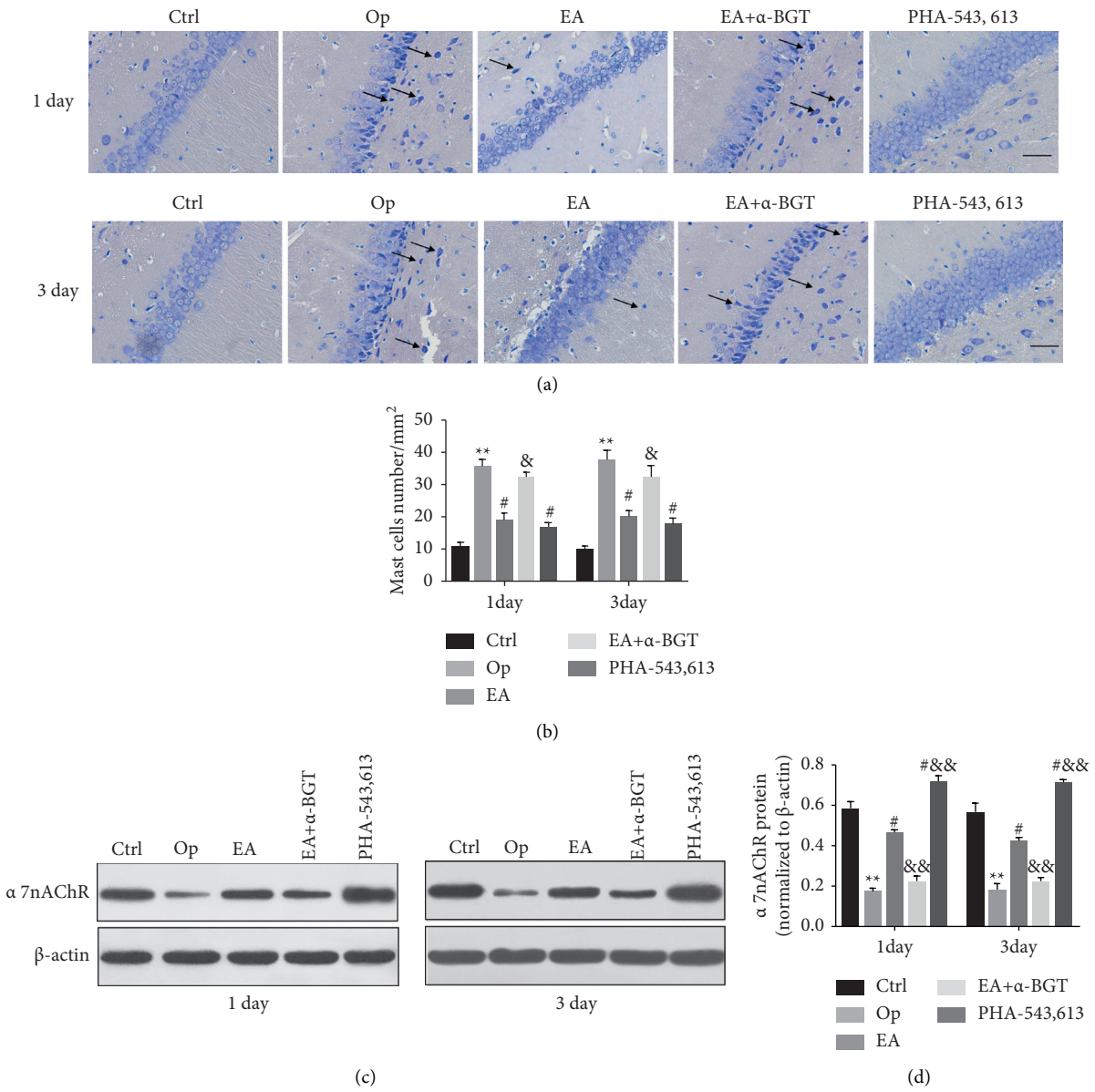

Figure 4: EA inhibited MC degranulation associated with α7nAChR activation in the hippocampus. Hippocampal sections (10 μm) were prepared 1 and 3 days after surgery. (a) Brain mast cells were stained with toluidine blue (TB). (b) Quantification of mast cells in the hippocampal CA1 region on day 1 and 3 postoperatively. (c) Western blot analysis of α7nAChR protein expression in the hippocampus on day 1 and 3 postoperatively. (d) Quantified and normalized to β-actin levels. Graphs show the mean ± S.E.M. ($n = 4$). $^{**}P < 0.01$ versus the control group; $^{\#}P < 0.05$ versus the Op group; and $^{\&\&}P < 0.01$ or $^{\&}P < 0.05$versus the EA group, scale bar = 25 μm.

demonstrated that the cognitive ability of rats was decreased postoperatively; however, pretreatment using EA or the α7nAChR agonist PHA-543613 partially reversed cognitive impairment, whereas the effect of EA on cognitive improvement was partially reversed by α-BGT, a selective α7nAChR antagonist. This indicated that cognitive dysfunction was induced successfully in our animal model and that α7nAChR might mediate the cognitive improvement induced by EA in rats after tibial fracture surgery.

Sustained neuroinflammation is implicated in the progression of cognitive impairment [27]. Increasing evidence suggests that postoperative trauma causes central and systemic inflammation, resulting in cognitive dysfunction. Proinflammatory cytokines, such as IL-1β and TNF-α, contribute to the initiation of neuroinflammation. Studies have reported that high levels of IL-1β and TNF-α in plasma and brain tissues are associated with POCD [28, 29]. According to recent studies, high levels of HMGB-1 were associated with postoperative impairment of memory function in rats [30, 31]. Our results suggested that on days 1 and 3 following surgery, the levels of mRNA expression of *HMGB-1, IL-1β,* and *TNF-α* in the hippocampus, and these proinflammatory cytokines in the serum significantly increased compared to those in the control group. Nonetheless, pretreatment with EA or the α7nAChR agonist PHA-543613 reversed the surgery-induced increase in

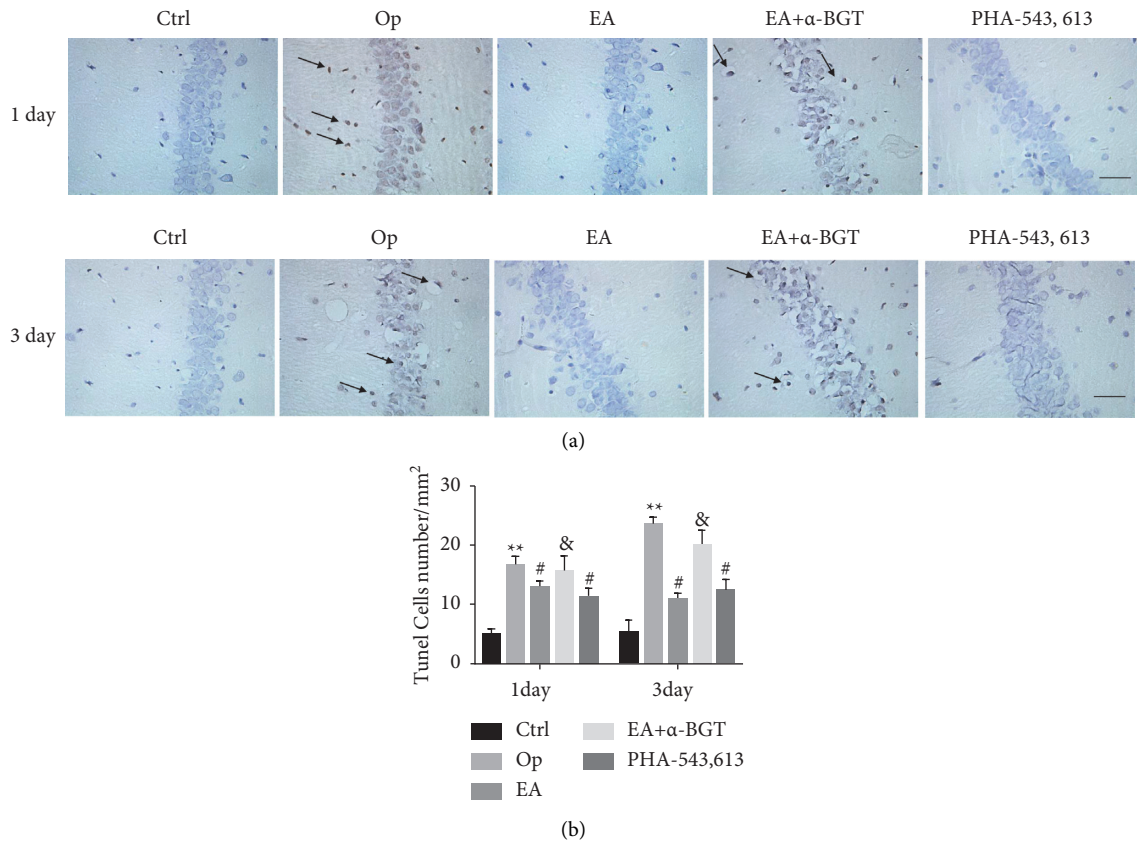

Figure 5: EA inhibited tibial fracture-induced apoptosis in the hippocampus. Hippocampal sections (10 μm) were prepared 1 and 3 days after surgery. (a) The apoptosis of neuronal cells was detected using TUNEL. (b) Quantification of apoptotic cells in the hippocampal CA1 region on day 1 and 3 postoperatively. Graphs show the mean ± S.E.M ($n = 4$). $^{**}P < 0.01$ versus the control group; $^{\#}P < 0.05$ versus the Op group; $^{\&}P < 0.05$ versus the EA group; scale bar = 25 μm.

HMGB-1, IL-1β, and TNF-α production. Furthermore, rats administered α-BGT did not show any anti-inflammatory benefits after receiving EA as a pretreatment. These findings indicated that α7nAChR might mediate decreased systemic and central inflammation induced by EA.

α7nAChR is a cholinergic-dependent signaling molecule that is implicated in various CNS disorders, such as Alzheimer's disease, schizophrenia, anxiety, depression, and Parkinson's disease [32]. α7nAChR is strongly expressed in the brain, particularly in the hippocampus. Furthermore, inhibition of α7nAChR by an α7nAChR antagonist exacerbated cognitive disorders in postoperative mice under general anesthesia [33]. However, trauma-induced neuroinflammation is prevented by preoperative treatment with α7nAChR agonists, thus ameliorating cognitive decline [34]. PHA-543613 is a selective α7nAChR agonist. A previous study demonstrated that pretreatment with PHA-543613 successfully reversed scopolamine-induced cognitive decline [12]. These findings suggested that cholinergic dysfunction is a pathogenic mechanism underlying POCD, which was in agreement with our findings that hippocampal α7nAChR protein levels were reduced in rats following tibial fracture surgery on days 1 and 3. Our study also demonstrated that EA and PHA-543613 pretreatment had a similar effect in reversing the reduction in α7AChR expression in rats postoperatively. In contrast, the increase in α7AChR protein expression induced by EA was reversed by the selective α7nAChR antagonist α-BGT. These findings suggested that α7nAChR activation is a critical mediator of the neuroprotective effects of EA.

In neurodegenerative disorders, MC activity is an early sign that often precedes neuroinflammation and neuronal death [35]. Once activated, brain MCs can rapidly release inflammatory chemicals that activate microglia, induce apoptosis of neurons, and disrupt the blood–brain barrier, thereby playing a critical role in the pathogenesis of neuroinflammation [36]. A recent study reported that α7nAChR might serve as an immunomodulator and perform a distinct function in MCs. Additionally, mucosal MCs (MMCs) were shown to be the primary cause of disease in a food allergy model. Moreover, the cholinergic neuroimmune interactions facilitated by α7nAChRs on MMCs were found to be critical for modulating pathological immune activation and restoring intestinal homeostasis [37]. In our study, EA and PHA-543613 pretreatment significantly lowered the proportion of activated MCs in the hippocampus; however, α-BGT reversed the EA-induced inhibition of activated MC to a certain extent. These findings indicate that EA inhibits hippocampal MC activation through α7nAChR.

Apoptosis, which is a form of programmed cell death, performs an instrumental function in neurodegenerative diseases [38]. A previous study illustrated that EA at GV29 and GV20 in rats significantly decreased the rate of neuronal apoptosis in the hippocampus, thereby effectively alleviating cognitive impairment [39]. In our study, we found a small number of TUNEL-positive neuronal cells in the EA- and PHA-543613-treated groups as opposed to the surgery group. Apoptosis was not inhibited by EA pretreatment in rats suffering from tibial fractures who were administered α-BGT. Therefore, we hypothesized that cholinergic signaling is essential in the neuroprotective effects of EA on anti-apoptosis.

To the best of our knowledge, the present study is the first to examine the immune-regulatory effects of EA at the Baihui (GV20) acupoint based on the inherent correlation between brain MCs and α7nAChR after tibial fracture surgery. However, there are some limitations in our study. First, we performed adult rats of POCD model in this study, aged rats of tibial fracture surgery should be further investigated. Second, in the future, mice with MC gene deletion or α7nAChR knockout could be used to further confirm the mechanism of EA in hippocampal MC α7nAChR improvement in mice after tibial fracture surgery. Third, not only Baihui (GV20) acupoint, but other acupoints should be studied. Finally, in recent years, acupuncture combined with ancient classical formulas medicine have been widely used in the treatment of chronic and critical diseases; so, in the follow up research, we will investigate the influence of EA combined with ancient classical formulas on the inherent correlation between brain MCs and α7nAChR after tibial fracture surgery.

In conclusion, the present study demonstrated that EA significantly ameliorated surgery-induced cognitive impairment by inhibiting the activation of brain MCs and neuroinflammation mediated by the α7nAChR-dependent cholinergic anti-inflammatory system.

Abbreviations

MC:	Mast cell
POCD:	Postoperative cognitive dysfunction
α7nAChR:	Alpha-7-nicotinic acetylcholine receptor
EA:	Electroacupuncture
α-BGT:	Alpha-bungarotoxin
MWM:	Morris water maze
TNF-α:	Tumor necrosis factor-α
IL-1β:	Interleukin-1β
HMGB-1:	High-mobility group box-1
TCM:	Traditional Chinese medicine
CNS:	Central nervous system
NIH:	National Institutes of Health
ELISA:	Enzyme-linked immunosorbent assay
RT-PCR:	Real-time polymerase chain reaction
TB:	Toluidine blue
TUNEL:	Terminal-deoxynucleotidyl transferase dUTP nick end labeling
MMCs:	Mucosal mast cells.

Data Availability

The data used to support the findings of this study were included in the article. All the authors declare that all the data in the manuscript were obtained by our experiments and the data are true and effective in the manuscript. The datasets used in the present manuscript are available from the corresponding author on reasonable request.

Conflicts of Interest

The authors have declared that they have no competing interests.

Authors' Contributions

Yanning Qian designed the study and was in charge of the funds. Yudi Zhou performed the experiment, Chenlu Mao, Sha Li, and Yaomei Cui provided help to the experiment. Cheng Hu was responsible for statistical analysis and Yudi Zhou wrote the manuscript. All authors read and approved the final manuscript.

Acknowledgments

The present study was supported by the Jiangsu Province Hospital of Chinese Medicine No. Y17017 (to Yudi Zhou).

References

[1] T. J. Avelino-Silva, F. Campora, J. A. E. Curiati, and W., Jacob-Filho, "Association between delirium superimposed on dementia and mortality in hospitalized older adults: a prospective cohort study," *PLoS Medicine*, vol. 14, no. 3, p. e1002264, 2017.

[2] Z. Jin, J. Hu, and D. Ma, "Postoperative delirium: perioperative assessment, risk reduction, and management," *British Journal of Anaesthesia*, vol. 125, no. 4, pp. 492–504, 2020.

[3] L. A. Daiello, A. M. Racine, and E. R. Marcantonio, "Postoperative delirium and postoperative cognitive dysfunction: overlap and divergence," *Anesthesiology*, vol. 131, no. 3, pp. 477–491, 2019.

[4] L. Evered, B. Silbert, and D. S. Knopman, "Recommendations for the nomenclature of cognitive changes associated with anaesthesia and surgery-2018," *British Journal of Anaesthesia*, vol. 121, no. 5, pp. 1005–1012, 2018.

[5] S. Subramaniyan and N. Terrando, "Neuroinflammation and perioperative neurocognitive disorders," *Anesthesia & Analgesia*, vol. 128, no. 4, pp. 781–788, 2019.

[6] X. Feng, Y. Uchida, and L. Koch, "Exercise prevents enhanced postoperative neuroinflammation and cognitive decline and rectifies the gut microbiome in a rat model of metabolic syndrome," *Frontiers in Immunology*, vol. 8, no. 11, p. 1768, 2017.

[7] Q. Liu, Y. M. Sun, and H. Huang, "Sirtuin 3 protects against anesthesia/surgery-induced cognitive decline in aged mice by suppressing hippocampal neuroinflammation," *Journal of Neuroinflammation*, vol. 18, no. 1, pp. 41–46, 2021.

[8] P. P. Feng, P. Deng, and L. H. Liu, "Electroacupuncture alleviates postoperative cognitive dysfunction in aged rats by inhibiting hippocampal neuroinflammation activated via microglia/TLRs pathway," *Evidence-based Complementary*

and Alternative Medicine, vol. 2017, Article ID 6421260, 10 pages, 2017.

[9] M. G. Frasch, M. Szynkaruk, and A. P. Prout, "Decreased neuroinflammation correlates to higher vagus nerve activity fluctuations in near-term ovine fetuses: a case for the afferent cholinergic anti-inflammatory pathway?" *Neuroinflammation*, vol. 13, no. 1, pp. 103–108, 2016.

[10] C. Song, J. Shi, and J. Xu, "Post-transcriptional regulation of α7 nAChR expression by miR-98-5p modulates cognition and neuroinflammation in an animal model of Alzheimer's disease," *Federation of American Societies for Experimental Biology Journal*, vol. 35, no. 6, Article ID e21658, 2021.

[11] S. Adigh-Eteghad, M. Talebi, and J. Mahmoudi, "Selective activation of α7 nicotinic acetylcholine receptor by PHA-543613 improves Aβ25-35-mediated cognitive deficits in mice," *Neuroscience*, vol. 298, pp. 81–93, 2015.

[12] N. Bruszt, Z. K. Bali, S. A. Tadepalli, L. V. Nagy, and I. Hernádi, "Potentiation of cognitive enhancer effects of Alzheimer's disease medication memantine by alpha7 nicotinic acetylcholine receptor agonist PHA-543613 in the Morris water maze task," *Psychopharmacology (Berl)*, vol. 238, no. 11, pp. 3273–3281, 2021.

[13] L. Zhao, J. Chen, and C. Z. Liu, "A review of acupoint specificity research in China: status quo and prospects," *Evidence-based Complementary and Alternative Medicine*, vol. 2012, Article ID 543943, 16 pages, 2012.

[14] L. Sun, Y. Yong, and P. Wei, "Electroacupuncture ameliorates postoperative cognitive dysfunction and associated neuroinflammation via NLRP3 signal inhibition in aged mice," *CNS Neuroscience and Therapeutics*, vol. 28, no. 3, pp. 390–400, 2022.

[15] P. R. Liu, Y. Zhou, Y. Zhang, and S. Diao, "Electroacupuncture alleviates surgery-induced cognitive dysfunction by increasing α7-nAChR expression and inhibiting inflammatory pathway in aged rats," *Neuroscience Letters*, vol. 6596 pages, 2017.

[16] Z. Q. Wu, S. Y. Cui, L. Zhu, and Z. Q. Zou, "Study on the mechanism of mTOR-mediated autophagy during electroacupuncture pretreatment against cerebral ischemic injury," *Evidence-based Complementary and Alternative Medicine*, vol. 2016, Article ID 9121597, 8 pages, 2016.

[17] C. Mao, C. Hu, and Y. Zhou, "Electroacupuncture pretreatment against cerebral ischemia/reperfusion injury through mitophagy," *Evidence-based Complementary and Alternative Medicine*, vol. 2020, Article ID 7486041, 9 pages, 2020.

[18] Y. Cao and L. W. L. T. Lin, "Acupuncture attenuates cognitive deficits through α7nAChR mediated anti-inflammatory pathway in chronic cerebral hypoperfusion rats," *Life Sciences*, vol. 266, Article ID 118732, 2021.

[19] X. Zhang, H. Yao, and Q. Qian, "Cerebral mast cells participate in postoperative cognitive dysfunction by promoting astrocyte activation," *Cellular Physiology and Biochemistry*, vol. 40, no. 1-2, pp. 104–116, 2016.

[20] S. Zhang, H. Dong, X. Zhang, N. Li, J. Sun, and Y. Qian, "Cerebral mast cells contribute to postoperative cognitive dysfunction by promoting blood–brain barrier disruption," *Behavioural Brain Research*, vol. 298, pp. 158–166, 2016.

[21] Q. Q. Qian, X. Zhang, and Y. W. Wang, "Pro-inflammatory role of high-mobility group box-1 on brain mast cells via the RAGE/NF-κB pathway," *Journal of Neurochemistry*, vol. 151, no. 5, pp. 595–607, 2019.

[22] Q. Wang, F. Wang, and X. Li, "Electroacupuncture pretreatment attenuates cerebral ischemic injury through α7 nicotinic acetylcholine receptor-mediated inhibition of high-mobility group box 1 release in rats," *Journal of Neuroinflammation*, vol. 9, no. 24, pp. 26–29, 2012.

[23] R. Morris, "Developments of a water-maze procedure for studying spatial learning in the rat," *Journal of Neuroscience Methods*, vol. 11, no. 1, pp. 47–60, 1984.

[24] S. D. Skaper, L. Facci, M. Zusso, and P. Giusti, "Neuroinflammation, mast cells, and glia: dangerous liaisons," *The Neuroscientist*, vol. 23, no. 5, pp. 478–498, 2019.

[25] X. Feng, V. Degos, and L. G. Koch, "Surgery results in exaggerated and persistent cognitive decline in a rat model of the Metabolic Syndrome," *Anesthesiology*, vol. 118, no. 5, pp. 1098–1105, 2013.

[26] C. V. Vorhees and M. T. Williams, "Morris water maze: procedures for assessing spatial and related forms of learning and memory," *Nature Protocols*, vol. 1, no. 2, pp. 848–858, 2006.

[27] K. T. Granger and J. H. Barnett, "Postoperative cognitive dysfunction: an acute approach for the development of novel treatments for neuroinflammation," *Drug Discovery Today*, vol. 2, pp. 1111–1114, 2021.

[28] M. Cibelli and A. R. F. N. Terrando, "Role of interleukin-1beta in postoperative cognitive dysfunction," *Annals of Neurology*, vol. 68, no. 3, pp. 360–368, 2016.

[29] N. Terrando, C. Monaco, and D. Ma, "Tumor necrosis factor-alpha triggers a cytokine cascade yielding postoperative cognitive decline," *Proceedings of the National Academy of Sciences of the United States of America*, vol. 107, no. 47, pp. 18–22, 2010.

[30] F. Lin, W. Shan, Y. Zheng, L. Pan, and Z. Zuo, "Toll-like receptor 2 activation and up-regulation by high mobility group box-1 contribute to post-operative neuroinflammation and cognitive dysfunction in mice," *Journal of Neurochemistry*, vol. 158, no. 2, pp. 328–341, 2021.

[31] M. Yu, H. Huang, S. Dong, H. Sha, W. Wei, and C. Liu, "High mobility group box-1 mediates hippocampal inflammation and contributes to cognitive deficits in high-fat high-fructose diet-induced obese rats," *Brain, Behavior, and Immunity*, vol. 82, pp. 167–177, 2019.

[32] A. Taly, P. J. Corringer, D. Guedin, and P. Changeux, "Nicotinic receptors: allosteric transitions and therapeutic targets in the nervous system," *Nature Reviews Drug Discovery*, vol. 8, no. 9, pp. 733–750, 2009.

[33] N. Terrando, L. I. Eriksson, and J. K. Ryu, "Resolving postoperative neuroinflammation and cognitive decline," *Annals of Neurology*, vol. 70, no. 6, pp. 986–995, 2011.

[34] F. J. Kong, L. L. Ma, H. H. Zhang, and J. Q. Zhou, "Alpha 7 nicotinic acetylcholine receptor agonist GTS-21 mitigates isoflurane-induced cognitive impairment in aged rats," *Journal of Surgical Research*, vol. 194, no. 1, pp. 255–261, 2015.

[35] R. Silver and J. P. Curley, "Mast cells on the mind: new insights and opportunities," *Trends in Neurosciences I*, vol. 36, no. 9, pp. 513–521, 2013.

[36] D. Kempuraj, S. Mentor, and R. Thangavel, "Mast cells in stress, pain, blood-brain barrier, neuroinflammation and alzheimer's disease," *Frontiers in Cellular Neuroscience*, vol. 13, no. 54, 2019.

[37] T. Yamamoto, T. Kodama, and J. Lee, "Anti-allergic role of cholinergic neuronal pathway via α7 nicotinic ACh receptors

on mucosal mast cells in a murine food allergy model," *PLoS One*, vol. 9, no. 1, Article ID e85888, 2014.

[38] M. Obulesu and M. J. Lakshmi, "Apoptosis in Alzheimer's disease: an understanding of the physiology, pathology and therapeutic avenues," *Neurochemical Research*, vol. 39, no. 12, pp. 2301–2312, 2014.

[39] X. He, S. Zhao, and W. You, "Neuroprotective effects of electroacupuncture preventive treatment in senescence-accelerated mouse prone 8 mice," *Chinese Journal of Integrative Medicine*, vol. 24, no. 2, pp. 133–139, 2018.

Hindawi
Evidence-Based Complementary and Alternative Medicine
Volume 2022, Article ID 1079803, 11 pages
https://doi.org/10.1155/2022/1079803

Research Article

Effects of Erchen Decoction on Oxidative Stress-Related Cytochrome P450 Metabolites of Arachidonic Acid in Dyslipidemic Mice with Phlegm-Dampness Retention Syndrome: A Randomized, Controlled Trial on the Correspondence between Prescription and Syndrome

Jing Chen,[1] **Chao Ye**,[2] **Zheng Yang**,[3] **Pinhui Li**,[4] **Hongfei Wu**,[2] **Bing Xu**,[5] **Shan Zhang**,[3] **and Xiaolin Xue**[3]

[1]*Preventive Treatment of Disease Department, The Third Affiliated Hospital, Beijing University of Chinese Medicine, Beijing 100029, China*
[2]*Orthopedics Department, Dongzhimen Hospital, Beijing University of Chinese Medicine, Beijing 100700, China*
[3]*School of Traditional Chinese Medicine, Beijing University of Chinese Medicine, Beijing 100029, China*
[4]*Cardiovascular Department, Hainan Provincial Hospital of Traditional Chinese Medicine, Haikou, Hainan, China*
[5]*Traditional Chinese Medicine Department, Tibetology Research Center of Beijing Tibetan Medicine Hospital, Beijing, China*

Correspondence should be addressed to Xiaolin Xue; xuexiaolinbucm@163.com

Received 9 January 2022; Accepted 28 February 2022; Published 29 March 2022

Academic Editor: Jun Jiang

Phlegm-dampness retention (PDR) syndrome is one of the main syndromes of dyslipidemia. This study investigated the effects of Erchen decoction (ECD) on concentrations of two oxidative stress-related cytochrome P450 (CYP450) metabolites of arachidonic acid—14,15-dihydroxyeicosatrienoic acid (14,15-DHET) and 20-hydroxyeicosatetraenoic acid (20-HETE)—in mice with dyslipidemia and phlegm-dampness retention (PDR) syndrome ($n = 5$ C57BL/6J mice and $n = 30$ apolipoprotein E knockout mice). Murine models of the disease and syndrome were established using multifactor stimulation. Then, all mice were assigned to normal, model, low- (L-), medium- (M-), or high- (H-) dose ECD groups or to a control or an unmatched prescription-syndrome (unmatched P-S) group; five mice were included in each group. Dose formulations were administered by oral gavage for 30 days to animals in the corresponding groups. We detected and analyzed hematoxylin and eosin (HE) staining characteristics of the mouse aorta and serum total cholesterol (TC), low-density lipoprotein cholesterol (LDL-C), peroxynitrite ($ONOO^-$), 14,15-DHET, and 20-HETE concentrations in each group. TC and LDL-C concentrations significantly decreased in the M-ECD versus control group ($P < 0.05$); however, the TC and LDL-C concentrations were not significantly different in the unmatched P-S versus model group ($P > 0.05$). After treatment in the P-S correspondence groups (L-ECD, M-ECD, and H-ECD groups), the concentration of $ONOO^-$ decreased to different degrees in each group. Among these groups, the concentration of $ONOO^-$ significantly decreased in the L-ECD, M-ECD, and H-ECD groups versus the model group ($P < 0.05$). However, the concentration of $ONOO^-$ was not significantly different in the unmatched P-S versus the model group ($P > 0.05$). From the perspective of aortic HE staining, the P-S group experienced an improved endothelium structure after treatment. 14,15-DHET concentrations significantly increased in the normal, M-ECD, and H-ECD groups versus the model group; in the H-ECD versus the L-ECD group; and in the H-ECD versus the control group (all $P < 0.05$) to various extents after different doses of the prescription. 20-HETE concentrations pronouncedly decreased in the M-ECD versus normal group; in the M- and H-ECD groups versus the model group; in the M-ECD versus the L-ECD group; in the M-ECD versus the control group; and in the M-ECD versus the unmatched P-S ($P < 0.05$). However, the concentrations of 14,15-DHET and 20-HETE in the model group were not significantly different from those of the unmatched P-S ($P > 0.05$). In this study, ECD reversed blood lipid indexes and ameliorated oxidative stress-related metabolites, elevating serum 14,15-DHET and lowering serum 20-HETE in mice with dyslipidemia and PDR syndrome via CYP450 pathways of arachidonic acid metabolism. The efficacy of ECD relies on correspondence between the prescription and the syndrome. These findings

scientifically validate the treatment according to traditional Chinese medicine syndrome differentiation. ECD can strengthen the protective effect on the vascular endothelium by driving out pathogenic factors and strengthening healthy resistance. Its efficacy may be related to the adjustment of the polarization state of macrophages.

1. Introduction

Dyslipidemia has become more prevalent among Chinese adults during recent years as a result of better living conditions [1]. The condition may elevate serum oxygen free radical levels and exacerbate the inflammatory response, leading to vascular endothelial cell damage [2] that damage in turn has close associations with cardiocerebrovascular diseases, such as coronary atherosclerotic heart disease and cerebral infarction [3]. Macrophage recruitment around endothelial cells is essential during vascular endothelial cell damage and is an early cause of plaque formation [4].

Traditional Chinese medicine (TCM) treatments have multitarget, multipathway, and multidimensional features. The efficacy of TCM in treating dyslipidemia has been demonstrated [5]. Herbs used in TCM herbs contain various active components, and their properties are often categorized according to TCM theory into four natures (hot, warm, cool, and cold), five flavors (salty, sweet, sour, spicy, and bitter), and medical actions of ascending, descending, floating, and sinking. The selection of proper herbs for patients boils down to an accurate diagnosis of TCM syndromes, which underlies the efficacy of TCM treatment. The characteristics of phlegm-dampness retention (PDR) syndrome, which is frequently diagnosed in patients with dyslipidemia, have been the focus of exploration in our study series.

One important mechanism of endothelial dysfunction is the enhancement of oxidative stress. Excess nitric oxide (NO) can combine with superoxide to form peroxynitrite ($ONOO^-$). $ONOO^-$ causes oxidative stress and tissue damage in the vascular endothelium through protein oxidation or nitration. Our research group previously found that the serum concentration of $ONOO^-$ increased in patients with dyslipidemia and PDR syndrome; in fact, its concentration can reflect the degree of PDR syndrome [6]. This research showed that enhanced oxidative stress is a characteristic of PDR syndrome with dyslipidemia. Therefore, studying the PDR syndrome and dyslipidemia by assessing the characteristics of oxidative stress is feasible.

Macrophages, including M1 and M2 subtypes [7], are critical for vascular endothelial injury in dyslipidemia. M1 macrophages are responsible for inflammatory factor release to fuel inflammation, inducing vascular endothelial cell damage [8]; conversely, M2 macrophages generate anti-inflammatory mediators involved in angiogenesis and tissue growth, thus limiting the severity of inflammation [9]. The two functionally antagonistic phenotypes can be transformed into each other under various stimulations; this transformation is consistent with the struggle between or waxing and waning of healthy qi (energy) and pathogenic factors during the onset and progression of diseases and syndromes, as described in TCM theory. In a previous study series, we established murine models of dyslipidemia with PDR syndrome and spleen–kidney yang deficiency (SKYD) syndrome using multifactor stimulation that can mimic the core physiopathological process of the disease and simulate the critical pathogenesis of the syndrome. RNA sequencing of endothelial macrophages has revealed that increased levels of CYP450 metabolites of arachidonic acid are a predominant feature of dyslipidemia with PDR [10]. CYP450 pathways are one pathway that drives arachidonic acid metabolism [11], and the metabolites may impair endothelial cell function through oxidative stress. The molecules 14,15-dihydroxyeicosatrienoic acid (14,15-DHET) and 20-hydroxyeicosatetraenoic acid (20-HETE) are critical downstream molecules in the CYP450 pathway of arachidonic acid metabolism [12].

Prescription-syndrome (P-S) correspondence often uses counterevidence for the prescription-syndrome relationship from drugs, formulas, treatment strategies, and prescription disciplines; in P-S, formulas must be prescribed for the syndrome and adjusted with the syndrome. The molecular changes that occur during matched P-S treatment can be the material basis of the syndrome. Erchen decoction (ECD) is a classic TCM formula for PDR syndrome described in *Prescriptions of Peaceful Benevolent Dispensary* [13]; it is a matched prescription for PDR with dyslipidemia because the prescription discipline conforms to the syndrome pathogenesis. However, whether the blood lipid index, aortic endothelial structure, serum ONOO-, CYP450 metabolites, 14,15-DHET, or 20-HETE can be altered by treatment remains unknown. Therefore, we explored the effects of ECD on these variables in mice with dyslipidemia and PDR syndrome.

In this study, we used apolipoprotein E knockout (ApoE-/-) mice to generate models of dyslipidemia with PDR or SKYD for matched and unmatched prescription-syndrome experiments. ECD was used as the intervention to explore its effect on the serum total cholesterol (TC), low-density lipoprotein cholesterol (LDL-C), $ONOO^-$, 14,15-DHET, and 20-HETE levels. The objectives of this study are threefold: (1) to investigate whether ECD affected oxidative stress-related molecules in dyslipidemia with PDR syndrome via CYP450 pathways of arachidonic acid metabolism; (2) to scientifically validate the treatment according to TCM syndrome differentiation from the perspective of prescription-syndrome correspondence; and (3) to speculate about the correlation of the efficacy of ECD with macrophage polarization according to characteristic changes in CYP450 metabolites of arachidonic acid as a key player in dyslipidemia with PDR syndrome.

2. Materials and Methods

Figure 1 presents an overview of the study's materials and methods, described in full as follows.

2.1. Experimental Animals. The animals featured in the research included 30 ApoE-/- mice; all were male, were 6 weeks old, and had a body mass of approximately 20 (±5) g. In addition, five C57BL/6J mice of the same strain were used; all were male, were 6 weeks old, and had a body mass of approximately 20 (±5) g. All animals were raised in the Beijing Changyang Xishan Farm; the license number for the use of experimental animals is SCXK (jing) 2019-0008. The rearing environment incorporated a room temperature of 21–25°C, 50%–70% humidity, and 12 h of alternating light and shade.

All procedures in this study followed the *NIH Guide for the Care and Use of Laboratory Animals* (revised 2011). This study was approved by the Medical and Experimental Animal Ethics Committee of Beijing University of Chinese Medicine (approval no. BUCM-4-2021090102-3098; Beijing, China).

2.2. Drugs and Preparations. Erchen decoction is composed of six kinds of Chinese herbal medicine: pinelliae praeparata (fabanxia), 15 g; poria (fuling), 15 g; pericarpium citri reticulatae (chenpi), 10 g; glycyrrhizae radix et rhizoma (zhigancao), 6 g; zingiberis rhizoma recens (shengjiang), 10 g; and mume fructus (wumei), 3 g.

All Chinese herbal medicines were provided by The Third Affiliated Hospital, Beijing University of Chinese Medicine. The Chinese herbal medicine decoction was prepared according to the conventional TCM decoction method: (1) all herbs were placed into a saucepan (porcelain) with 500 mL of water; (2) after the herbs were soaked for 30 min, they were boiled over high heat; (3) the heat was reduced to low and the decoction simmered for 20 min; (4) the liquid was poured out; (5) water was added again, brought to a boil over high heat, then reduced to low heat and simmered for 15 min; (6) concentrate the two solutions by putting them together.

Atorvastatin calcium tablets were used as a positive control (Meidaxin, 10 mg/tablet; Qilu Pharmaceutical (Hainan) Co., Ltd.; batch no. 6949384100644).

2.3. Reagents and Instruments. The following kits were used in the study: mouse 14,15-DHET ELISA kit (Shanghai Lianshuo Biological Technology Co., Ltd); mouse 20-HETE ELISA kit (Shanghai Lianshuo Biological Technology Co., Ltd); $ONOO^-$ kit (Shanghai Lianshuo Biological Technology Co., Ltd); LDL-C kit (Nanjing Jiancheng Bioengineering Research Institute Co., Ltd); and TC kit (Nanjing Jiancheng Bioengineering Research Institute Co., Ltd).

The experimental modeling feed involved a dyslipidemia feed formula that consisted of 63.6% basal feed, 15% lard, 20% sucrose, 1.2% cholesterol, and 0.2% sodium cholate. The feed was provided by the Beijing Keaoxieli Feed Co.

Propylthiouracil (Ruji, 5 g/tablet) was obtained from Shanghai Ruji Biotechnology Co., Ltd. (batch no. 210720).

2.4. Modeling, Grouping, and Intervention Methods. Modeling involved 30 ApoE-/- mice and five C57BL/6J mice of the same strain that were adaptively fed for seven days. C57BL/6J mice were used for the normal group, and ApoE-/- mice were used for the model group. Using the random number table method, the 30 mice were divided: 25 were used to model PDR syndrome and dyslipidemia, and five were used to model SKYD syndrome and dyslipidemia. The 25 ApoE-/- mice with PDR syndrome and dyslipidemia were randomly selected and fed a high-fat diet for four weeks (weeks 1–4). The five ApoE-/- mice with SKYD syndrome and dyslipidemia were randomly selected and given 0.1% propylthiouracil by gavage at a dose of 10 mg/kg/d during weeks 1–4 and high-fat chow for two weeks during weeks 5 and 6.

Grouping, after successful modeling, involved random assignment into the normal group (Nor group, $n = 5$), model group (Mod group, $n = 5$), low-dose Erchen decoction group (L-ECD group, $n = 5$), medium-dose Erchen decoction group (M-ECD group, $n = 5$), high-dose Erchen decoction group ((H-ECD group, $n = 5$), control drug group ($n = 5$) and unmatched prescription-syndrome group (unmatched P-S group, $n = 5$)

Intervention methods involved an L-ECD group, an M-ECD group, and an H-ECD group that were gavaged with Erchen decoction dosages of 4.45, 8.90, and 17.8 g/kg/d, respectively. The control group was gavaged with an atorvastatin calcium dosage of 1.5 mg/kg/d, and the unmatched P-S group was gavaged with an Erchen decoction dosage of 8.90 g/kg/d. The 8.90 g/kg/d dosage in mice is equivalent to a 60 kg dose in adult humans, according to the human-mouse dose conversion method described in *Research Methodology of Pharmacology of Traditional Chinese Medicine*. The normal group and the model group were given the same dose of normal saline by gavage. All groups were given continuous gavage for four weeks (Figure 2).

2.5. Serum Sample and Aorta Sample Collection. For serum samples, after all groups were given continuous gavage for four weeks, and mice were fasted without water for 18 h before sampling and anesthesia was used for execution. Whole blood samples were taken from the animals in all groups; the samples were placed in conventional serum tubes and centrifuged at 3,000 rpm for 15 min to separate the serum. The resulting separate samples were immediately stored in a refrigerator at −80°C.

Samples of the aortic tissues from mice in the normal, model, L-ECD, M-ECD, and H-ECD groups were taken.

2.6. Detection of Content in Serum. For 14,15-DHET and 20-HETE determination, the 14,15-DHET and 20-HETE contents in the serum samples were measured by ELISA. The optical density was measured at a wavelength of 450 nm by an enzyme labeling instrument, and the concentration was calculated according to the standard curve.

For $ONOO^-$ determination, the $ONOO^-$ content in the serum samples was measured by biochemical methods, and

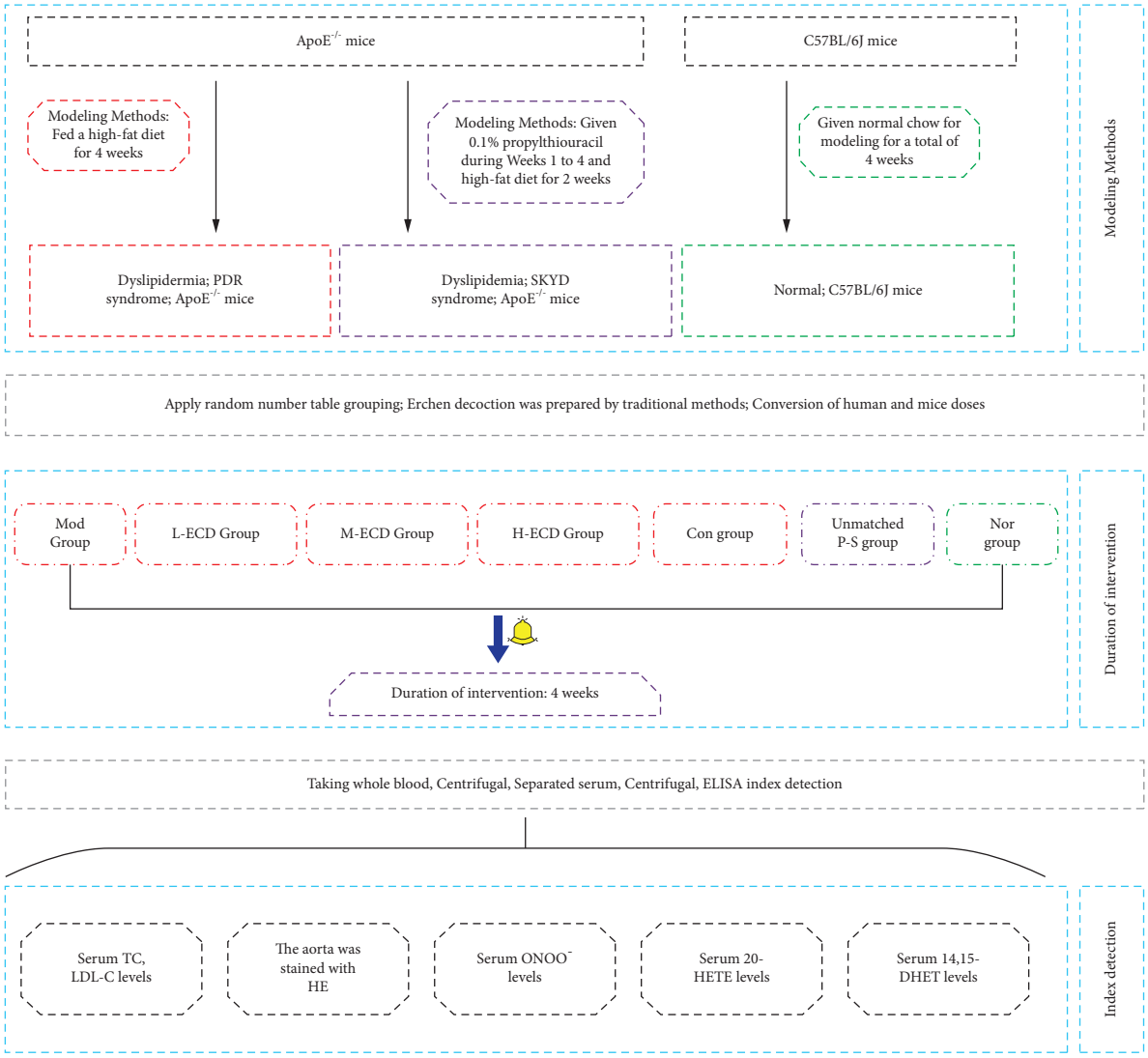

Figure 1: Research flowchart.

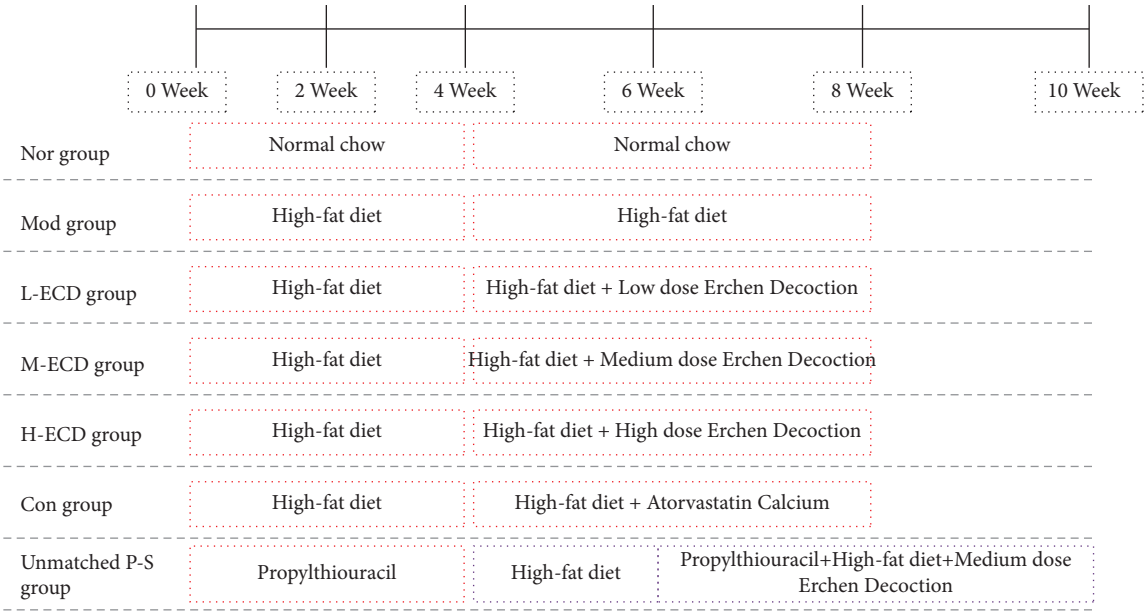

Figure 2: Animal modeling, grouping, and intervention flowchart.

the concentration was calculated according to the spectrophotometer findings.

For TC determination, the TC content in serum was quantified by enzyme labeling colorimetry with a kit. The optical density was measured at a wavelength of 510 nm with a microplate reader, and the concentration was calculated according to the formula.

For LDL-C determination, the LDL-C content in serum was quantified by enzyme labeling colorimetry with a kit. The optical density was measured at a wavelength of 546 nm with a microplate reader, and the concentration was calculated according to the formula.

2.7. Aortic Histopathology. The specimens were placed in 10% neutral formalin and fixed at room temperature for 24 h. Freshly prepared 4% formaldehyde was fixed at room temperature for 48 h and then placed into paraffin-embedded sections. The specimens were cut into 4 mm thick sections and stained with hematoxylin and eosin to observe the morphological characteristics of the vascular endothelium. Photos were taken after dyeing, and an optical microscope (AE41; Motic) equipped with a digital scanner (Panoramic MIDI; 3DHISTECH) was used to record the images of stained sections.

2.8. Statistical Methods. Animal-specific data were statistically processed using SPSS (version 19.0) statistical software. The measurement data were expressed as the mean ± the standard deviation. A one-way analysis of variance with randomized group design was used for comparisons between groups. Fisher's least significant difference test was used for two-way comparisons if the data variance was the same; Tamhane's test was used for two-way comparisons if the variance was not the same. Differences were considered statistically significant at $P < 0.05$. The test level was $\alpha = 0.05$, and the confidence interval for parameter estimation was 95%.

3. Results

In total, 30 ApoE-/- mice and five C57BL/6J mice of the same strain without deletion were used in the experiment. Therefore, data from 35 mice contributed to the analysis of results.

3.1. Effects of Different Concentrations of Erchen Decoction on Serum TC and LDL-C Concentrations in Mice with PDR and Dyslipidemia (Figure 3). After 30 days of gavage in the normal, model, L-ECD, M-ECD, H-ECD, control, and unmatched P-S groups, significant differences were noted in the serum concentration of TC ($P < 0.05$). After treatment of the P-S correspondence groups, the concentration of TC decreased to different degrees. When the serum TC concentrations were compared between groups, the L-ECD, M-ECD, H-ECD, and control group levels were all lower than those of the model group ($P < 0.05$). There was no significant difference between the concentrations in the unmatched P-S group and the model group ($P > 0.05$) (see Supplementary Material Table 1).

After 30 days of gavage in the normal, model, L-ECD, M-ECD, H-ECD, control, and unmatched P-S groups, significant differences were noted in the serum concentration of LDL-C ($P < 0.05$). After treatment of the P-S correspondence groups, the serum LDL-C concentrations were compared. When compared between groups, the concentration in the L-ECD group was lower than that of the model group ($P < 0.05$). There was no significant difference between the concentrations in the unmatched P-S group and the model group ($P > 0.05$) (see Supplementary Material Table 2).

3.2. Effects of Different Concentrations of Erchen Decoction on Serum $ONOO^-$ Concentration in Mice with PDR and Dyslipidemia (Figure 4). After 30 days of gavage in the normal, model, L-ECD, M-ECD, H-ECD, control, and unmatched P-S groups, significant differences were noted in the serum concentration of $ONOO^-$ ($P < 0.05$). After treatment of P-S correspondence groups, the concentration of $ONOO^-$ decreased to different degrees. When the serum $ONOO^-$ concentrations were compared between groups, the concentrations in the L-ECD, M-ECD, and H-ECD groups were all lower than the concentrations in the model group ($P < 0.05$). There was no significant difference between the concentrations in the unmatched P-S group and the model group ($P > 0.05$) (see Supplementary Material Table 3).

3.3. Effects of Different Concentrations of Erchen Decoction on Pathological Staining of Aorta in Mice with PDR and Dyslipidemia (Figure 5). Hematoxylin and eosin staining was performed on the aorta samples from mice in the normal, model, L-ECD, M-ECD, and H-ECD groups. No obvious lipid deposition or lipid stripes were found in any group; this result was in line with the characteristics of dyslipidemia models. The aortic endothelium of mice in the normal group was continuous and complete; in addition, the structure was clear, and there was no stenosis in the vascular lumen. The aortic endothelium of mice in the model group was continuous and complete, with a little irregular thickening, an unclear structure, local rupture, and inflammatory cell infiltration. The endothelium of mice in the L-ECD group showed little inflammatory cell infiltration and local fracture. The aortic endothelium of mice in the M-ECD and H-ECD groups was continuous and complete. In addition, the endothelial structure was clearer than that of the model group; the surface was smooth; and the intima, media, and adventitia were clearly displayed.

3.4. Effects of Different Concentrations of Erchen Decoction on Serum 14,15-DHET Concentration in Mice with PDR and Dyslipidemia (Figure 6). After 30 days of gavage in the normal, model, L-ECD, M-ECD, H-ECD, control, and unmatched P-S groups, significant differences were noted in the serum concentration of 14,15-DHET ($P < 0.05$). After treatment in the L-ECD, M-ECD, and H-ECD groups, the concentration of

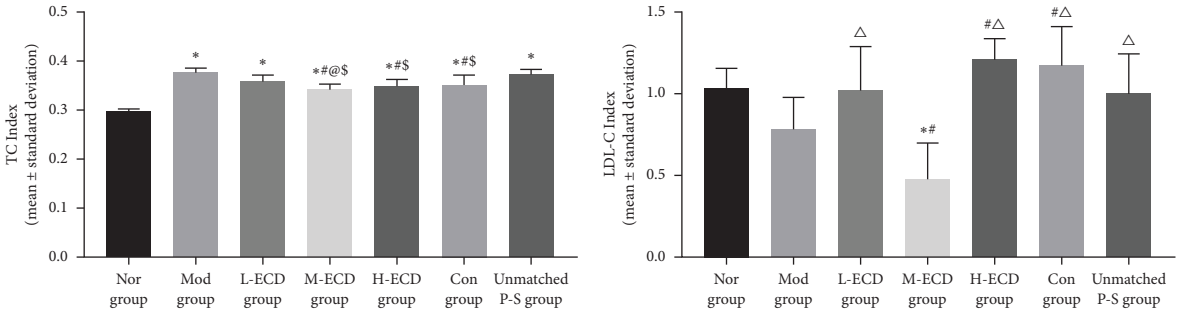

Figure 3: Effects of different concentrations of Erchen decoction on serum TC and LDL-C concentrations in mice with dyslipidemia and phlegm-dampness retention (PDR) syndrome. $^{*}P < 0.05$ as compared to the Nor group. $^{\#}P < 0.05$ as compared to the Mod group. $^{@}P < 0.05$ as compared to the L-ECD group. $^{\Delta}P < 0.05$ as compared to the M-ECD group. $^{\$}P < 0.05$ as compared to the unmatched P-S group.

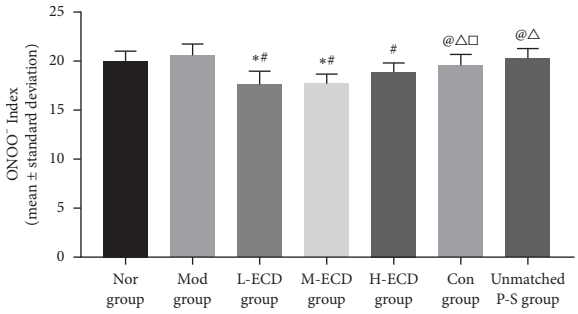

Figure 4: Effects of different concentrations of Erchen decoction on serum $ONOO^{-}$ concentration in mice with dyslipidemia phlegm-dampness retention (PDR) syndrome. $^{*}P < 0.05$ as compared to the Nor group. $^{\#}P < 0.05$ as compared to the Mod group. $^{@}P < 0.05$ as compared to the L-ECD group. $^{\Delta}P < 0.05$ as compared to the M-ECD group. $^{\square}P < 0.05$ as compared to the H-ECD group.

14,15-DHET increased to different degrees. When the serum 14,15-DHET concentrations were compared between groups, the levels in the normal, M-ECD, and H-ECD groups were all higher than those of the model group ($P < 0.05$); the concentration in the H-ECD group was significantly higher than that of the L-ECD group and the control group ($P < 0.05$). There was no significant difference between the concentrations in the unmatched P-S group and the model group ($P > 0.05$) (see Supplementary Material Table 4).

3.5. Effects of Different Concentrations of Erchen Decoction on Serum 20-HETE Concentration in Mice with PDR of Dyslipidemia (Figure 6). After 30 days of gavage in the normal, model, L-ECD, M-ECD, H-ECD, control, and unmatched P-S groups, significant differences were noted in the serum concentration of 20-HETE ($P < 0.05$). After treatment in the L-ECD, M-ECD, and H-ECD groups, the concentration of 20-HETE decreased to different degrees. When the serum 20-HETE concentrations were compared between groups, the levels in the normal, model, L-ECD, control, and unmatched P-S groups were all higher than the level of the M-ECD group ($P < 0.05$); the concentration in the H-ECD group was significantly lower than that of the control group ($P < 0.05$). There was no significant difference between the concentrations in the unmatched P-S group and model group ($P > 0.05$) (see Supplementary Material Table 5).

4. Discussion

Dyslipidemia can lead to endothelial dysfunction, which is a risk for cardiovascular diseases and an early step in the clinical manifestations of atherosclerosis [14]. Severe atherosclerosis is often found in patients with coronary heart disease and dyslipidemia [15]. Gained experience in TCM treatment has proven the efficacy of TCM formulas for dyslipidemia. However, accurate syndrome diagnosis is essential to ensure the therapeutic effects of TCM in this disease.

Macrophages are a pivotal determinant of vascular endothelial injury and are indispensable for the formation of atherosclerosis [16]. We previously conducted transcriptome analysis of endothelial macrophages from mice with dyslipidemia and PDR or SKYD to identify differentially expressed genes (DEGs) in the two syndromes; we then performed Gene Ontology enrichment analysis for the identified DEGs. We found that CYP450 pathways of arachidonic acid metabolism were the primary biological process enriched in these DEGs and that dyslipidemia with PDR was often characterized by increased levels of CYP450 metabolites of arachidonic acid.

Metabolism of arachidonic acid into epoxyeicosatrienoic acid (EET) and 20-hydroxyeicosatetraenoic acid (20-HETE) by CYP450 epoxygenase [17] are associated with oxidative stress. CYP450-mediated arachidonic acid metabolism has been proven to be a feasible target in the treatment of cardiovascular diseases [18], so we explored the characteristics of dyslipidemia with PDR from this aspect. EETs are active endogenous molecules that protect against apoptosis, inflammation, and oxidation [19]; however, they are unstable in the body and are readily metabolized into dihydroxyeicosatrienoic acid by soluble epoxide hydrolase [20]. Because 14,15-EET is the most abundant EET regioisomer, we measured its concentrations to reflect EET levels [21]. Higher 20-HETE levels may aggravate oxidative stress and vascular endothelial dysfunction. Much evidence has shown that enhancing EET biosynthesis while inhibiting EET hydrolysis [22] and 20-HETE biosynthesis can ameliorate endothelial dysfunction [23].

ECD is a classic TCM formula historically recorded as a treatment for phlegm and fluid retention or as a standard treatment for phlegm. It exerts spleen-strengthening,

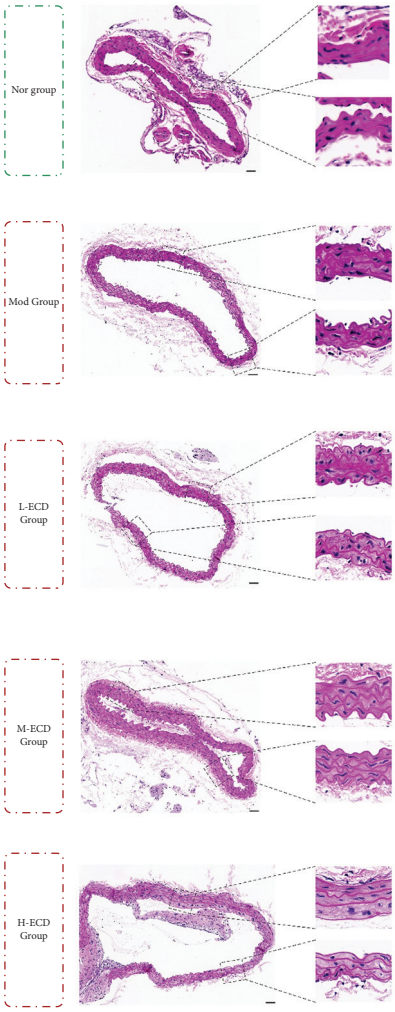

Figure 5: The aorta was stained with hematoxylin and eosin.

phlegm-dispelling, and spleen–stomach qi-promoting effects that correspond to the characteristics of dyslipidemia with PDR. ECD has been applied frequently in dyslipidemia treatment [24]. The treatment has been shown to alleviate inflammation in mice with hyperlipidemia [25] and to improve lipid metabolism in rats on high-fat diets [26]. However, the effects of ECD on CYP450 pathways of arachidonic acid metabolism in dyslipidemia with PDR remain uncertain and are worth additional exploration.

Prescription-syndrome correspondence is a sophisticated approach for syndrome studies. It stresses that a matched formula can be prescribed only when the syndrome is confirmed, which offers an effective theoretical basis for the objectification of TCM syndromes. Prescription-syndrome correspondence can be evidenced by an adequate response to the representative TCM formula after treatment. Upon counterevidence for prescription-syndrome relationships, the recovery of key indicators rescued by the formula can be considered the potential material basis of the syndrome. Therefore, prescription-syndrome correspondence is a critical method for elucidating potential syndrome pathogenesis.

TC and LDL-C are the main indicators of blood lipid. The concentrations of TC and LDL-C in P-S correspondence's M-ECD group were lower than those in the control group. These results showed that ECD can improve blood lipid indicators of dyslipidemia, which was consistent with previous research conclusions [26]. Hematoxylin and eosin staining showed that no lipid deposition was present in the vascular endothelium of the animal model of the disease and syndrome, which illustrated that the model was in line with the characteristics of dyslipidemia. A comparison of the model group with the ECD groups showed that ECD can improve the structure of the vascular endothelium.

$ONOO^-$ has strong oxidizing characteristics. It promotes the release of inflammatory factors through protein oxidation [27]. It causes oxidative stress and tissue injury in the vascular endothelium, which aggravates the endothelial injury. The damage is induced by promoting the aggregation of oxidized LDL, resulting in dysfunction of the cell membrane, structural damage to the cell membrane, and the formation of foam cells [28]. After treatment with ECD, the concentration of $ONOO^-$ decreased to different degrees in each group. The results showed that Erchen decoction can reverse the oxidative stress index of dyslipidemia phlegm turbidity suppression syndrome. The corresponding prescriptions and syndromes showed that the enhancement of oxidative stress was a characteristic of PDR syndrome with dyslipidemia, and this determination was consistent with previous research by our group. The current study also explored the ways in which ECD reversed the effect of oxidative stress.

14,15-EET is generated from arachidonic acid metabolism and functions as a bioactive mediator [29]. 14,15-DHET, a stable metabolite of 14,15-EET, reflects EET concentrations in the circulation. The metabolite helps improve vascular endothelial function by increasing eNOS protein expression. Our results showed that 14,15-DHET concentrations significantly increased in matched P-S groups, indicating that ECD offers protection to the vascular endothelium in dyslipidemia with PDR by elevating serum 14,15-DHET. According to TCM prescription disciplines, spleen-strengthening and damp-clearing properties of *Poria cocos* perfectly correspond to endogenous phlegm-damp generation as a result of dysfunction of the spleen, which governs transportation and transformation in transporting body fluids to the entire body. Chinese plums can produce saliva and clear dryness to alleviate damage to body fluids from other drugs. Ginger can warm the spleen and stomach and dispel cold. Its warm property helps remove phlegm and strengthen spleen–stomach qi to promote transportation, also clearing phlegm. As such, TCM theory explains the potential mechanisms for the protective effect of ECD on the vascular endothelium (i.e., strengthening healthy resistance).

Our previous research on serum metabolomics of patients with PDR syndrome and dyslipidemia showed the following: the main feature of the disease syndrome is that the accumulation of harmful metabolites leads to the enhancement of oxidative stress and damage to the vascular endothelium. Increased endothelial damage caused by increased oxidative stress is a characteristic of dyslipidemia with PDR syndrome. Therefore, changes in oxidative stress-

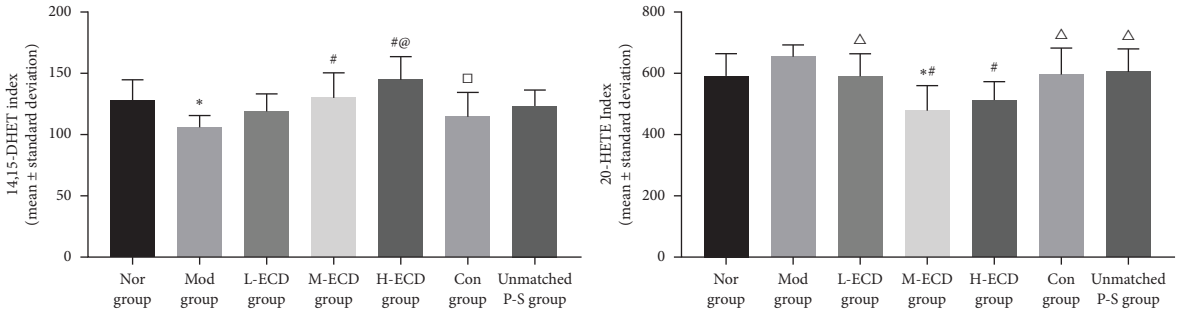

Figure 6: Effects of different concentrations of Erchen decoction on serum 14,15-DHET and 20-HETE concentrations in mice with dyslipidemia and phlegm-dampness retention (PDR) syndrome. $^{*}P < 0.05$ as compared to the Nor group. $^{\#}P < 0.05$ as compared to the Mod group. $^{@}P < 0.05$ as compared to the L-ECD group. $^{\Delta}P < 0.05$ as compared to the M-ECD group. $^{\square}P < 0.05$ as compared to the H-ECD group.

related noxious factors in mice with PDR syndrome and dyslipidemia after treatment can help explain the possible material basis of the syndrome. In our previous studies, we reported that dyslipidemia with PDR is characterized by endothelial damage induced by the accumulation of harmful metabolites, and we observed that those metabolites were altered after treatment; this finding gave insights into the possible material basis behind the syndrome pathogenesis [30].

20-HETE is a significant metabolite of arachidonic acid that is critical for the occurrence and progression of cardiovascular diseases. It is a potent vasoconstrictor that fuels vascular inflammation by increasing adhesion molecules and inflammatory cytokines induced by endothelial cell activation, and it triggers endothelial proinflammatory activation to promote atherosclerosis and vascular remodeling [31]. 20-HETE stimulates oxidative stress and a proinflammatory response by activating the nicotinamide adenine dinucleotide oxidase family in endothelial cells. Our findings showed that 20-HETE concentrations markedly decreased in the matched P-S groups versus the control group. These findings suggest that ECD inhibits 14,15-DHET expression to lower its circulating concentration, thus limiting the endothelial damage in dyslipidemia with PDR. In TCM theory, phlegm stagnation in the body may result in blood stasis in vessels, ultimately damaging arteries and veins. Among ECD components, *Pinellia ternata* takes the action of drying upon its pungent and warm properties, so it has strong phlegm-reducing power to clear phlegm stagnation and reopen vessels. The phlegm may obstruct qi flow and lead to phlegm–qi stagnation, which may cause vessel obstruction when it is prolonged. Citri reticulatae pericarpium promotes qi flow to resolve phlegm, thus smoothing qi circulation. The persistent presence of phlegm in the body also causes blood stasis. *Poria cocos* can drain and excrete water-damp to prevent phlegm retention. These are potential mechanisms to explain the effect of ECD against endothelial injury (i.e., by driving out pathogenic factors) in TCM.

Atorvastatin calcium is a classic agent against dyslipidemia; it inhibits cholesterol biosynthesis and lowers plasma LDL-C by inhibiting HMG-CoA reductase activity [32]. This study revealed that atorvastatin calcium failed to ameliorate serum 20-HETE and 14,15-DHET concentrations but did improve TC levels in mice with dyslipidemia and PDR. These findings are consistent with those of related mechanistic studies [33].

Notably, the recovery of serum TC, LDL-C, $ONOO^{-}$, 20-HETE, and 14,15-DHET concentrations after ECD treatment in the unmatched P-S group was not as satisfactory. Treatment based on syndrome differentiation is a unique theory and clinical approach of TCM. We treat the disease, syndrome, and formula as an integral whole that has multiple intraconnections; of these, syndrome types are critical whereby a particular formula can be linked to certain diseases. For mice with dyslipidemia and SKYD in the unmatched P-S group, formulas with spleen–kidney strengthening effects are considered matched treatments; other treatments, such as ECD, cannot achieve optimal efficacy. Thus, prescription-syndrome correspondence underlies the efficacy of ECD and scientifically validates the treatment according to syndrome differentiation.

CYP450 epoxygenase may inhibit monocyte inhibition, thus shifting macrophage polarization. As part of the CYP450 epoxygenase-EET-sEH-DHET system, it exerts the biofunctions of CYP450 [34]. Physiologically, the two antagonistic molecules, EET and 20-HETE, maintain endothelial cell equilibrium. Their antagonistic relationship is supported by findings from our previous study of macrophages using RNA sequencing, which showed that DEGs in endothelial macrophages of dyslipidemia with PDR were associated with both harmful and protective biological processes. Thus, we speculate that ECD can activate macrophage polarization via CYP450 pathways of arachidonic acid metabolism, thus alleviating damage to the vascular endothelium and exerting protective effects in dyslipidemia with PDR. From the perspective of prescription-syndrome correspondence, enhanced oxidative stress via activation of endothelial macrophage polarization can be a material basis for dyslipidemia with PDR.

The main limitations of this study are as follows: the specific mechanism of action of ECD is not clear because of the small number of detection indicators. Additional studies on the specific mechanism of action and different doses or duration of Erchen decoction treatment should be carried out in the future.

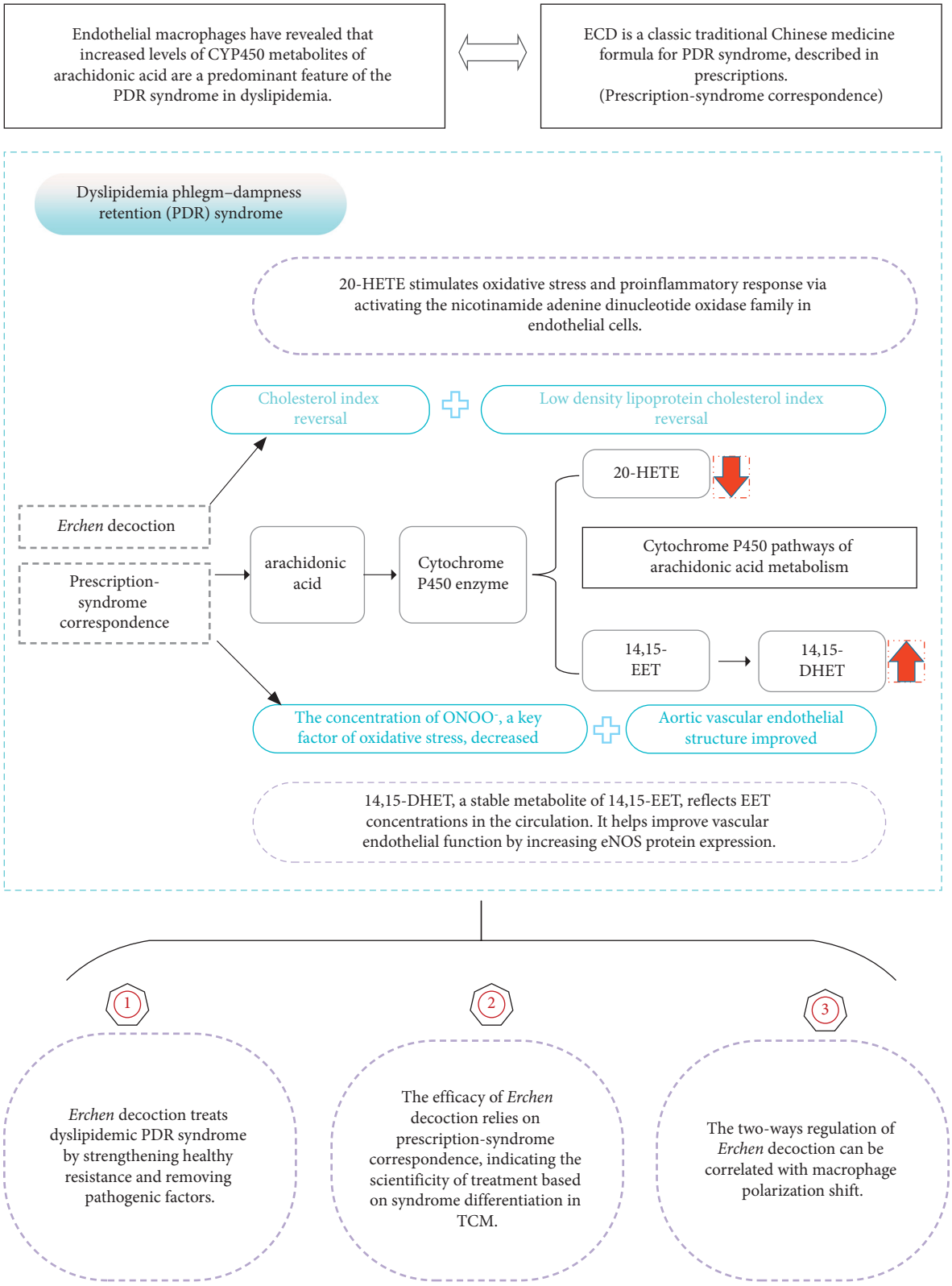

Figure 7: Effects of Erchen decoction on oxidative stress-related cytochrome P450 metabolites of arachidonic acid in mice with dyslipidemia and phlegm-dampness retention syndrome.

5. Conclusion

This study showed that ECD can reverse blood lipid indexes, reduce concentrations of $ONOO^-$, and improve oxidative stress-related metabolite levels (elevating serum 14,15-DHET and lowering serum 20-HETE) in mice with dyslipidemia and PDR, probably via CYP450 pathways of arachidonic acid metabolism. By strengthening healthy resistance and removing pathogenic factors, ECD protects the vascular endothelium to exert therapeutic effects in dyslipidemia with PDR. Compared with unmatched P-S treatment, treatment with ECD was efficacious because of its prescription-syndrome correspondence, which thus scientifically validates the treatment according to the syndrome differentiation in TCM. When reviewed along with our previous findings, this study shows that the efficacy of ECD can be correlated with macrophage polarization. We speculate that dynamic macrophage polarization switch may be a critical process in the pathogenesis of dyslipidemia with PDR according to the prescription-syndrome correspondence theory (Figure 7).

Abbreviations

Nor group:	Normal group
Mod group:	Model group
L-ECD group:	Low-dose ECD group
M-ECD group:	Medium-dose ECD group
H-ECD group:	High-dose ECD group
Con group:	Control group
Unmatched P-S group:	Unmatched prescription-syndrome
ECD:	Erchen decoction.

Data Availability

The datasets used and/or analyzed during the current study are available from the corresponding author on reasonable request.

Ethical Approval

This study was approved by the Medical and Experimental Animal Ethics Committee of Beijing University of Chinese Medicine, approval no. BUCM-4-2021090102-3098 (Beijing, China).

Conflicts of Interest

The authors have no conflicts of interest to disclose in relation to this article.

Authors' Contributions

XX and JC conceived and designed the study. JC, CY, SZ, and WH performed the modeling of animal models of diseases and syndromes and completed the relevant contents of the experiment. CY and FH performed the sampling. JC, CY, ZY, BX, LP, and XX acquired the data. JC, CY, ZY, and BX analyzed and interpreted data. JC and CY drafted the manuscript. XX critically revised the manuscript for important intellectual content. All authors read and approved the final manuscript.

Acknowledgments

Thanks are due to the National Natural Science Foundation of China for its support for this research. This study was supported by the National Natural Science Foundation of China (Grant no. 82004237).

Supplementary Materials

The supplementary materials contain five tables. Supplementary Table 1: TC index in 7 groups of mice. Supplementary Table 2: LDL-C index in 7 groups of mice. Supplementary Table 3: $ONOO^-$ index in 7 groups of mice. Supplementary Table 4: 14,15-DHET index in 7 groups of mice. Supplementary Table 5: 20-HETE index in 7 groups of mice. (*Supplementary Materials*)

References

[1] P. K. Song, Q. Q. Man, H. Li et al., "Trends in lipids level and dyslipidemia among Chinese adults, 2002-2015," *Biomedical and Environmental Sciences: BES*, vol. 32, no. 8, pp. 559–570, 2019.

[2] M. J. Chung, S.-H. Kim, J.-W. Park, Y. J. Lee, and S.-S. Ham, "Platycodon grandiflorum root attenuates vascular endothelial cell injury by oxidized low-density lipoprotein and prevents high-fat diet-induced dyslipidemia in mice by up-regulating antioxidant proteins," *Nutrition Research*, vol. 32, no. 5, pp. 365–373, 2012.

[3] Z. Li, T. Zhao, X. Tan, S. Lei, L. Huang, and L. Yang, "Polymorphisms in PCSK9, LDLR, BCMO1, SLC12A3, and KCNJ1 are associated with serum lipid profile in Chinese han population," *International Journal of Environmental Research and Public Health*, vol. 16, no. 17, p. 3207, 2019.

[4] R. L. Tiwari, V. Singh, and M. K. Barthwal, "Macrophages: an elusive yet emerging therapeutic target of atherosclerosis," *Medicinal Research Reviews*, vol. 28, no. 4, pp. 483–544, 2008.

[5] M. Guo, Y. Liu, Z. Y. Gao, and D. Z. Shi, "Chinese herbal medicine on dyslipidemia: progress and perspective," *Evidence-Based Complementary and Alternative Medicine*, vol. 2014, Article ID 163036, 11 pages, 2014.

[6] J. Chen, C. Ye, Z. Yang et al., "The Correlation between the Traditional Chinese Medicine (TCM) Syndrome and the Concentration of Adiponectin and Peroxynitrite in Dyslipidemia patients," *European Journal of Integrative Medicine*, vol. 8, 2016.

[7] L. C. Davies and P. R. Taylor, "Tissue-resident macrophages: then and now," *Immunology*, vol. 144, no. 4, pp. 541–548, 2015.

[8] J. T. Pesce, T. R. Ramalingam, M. M. Mentink-Kane et al., "Arginase-1-expressing macrophages suppress Th2 cytokine-driven inflammation and fibrosis," *PLoS Pathogens*, vol. 5, no. 4, Article ID e1000371, 2009.

[9] E. M. Moore and J. L. West, "Harnessing macrophages for vascularization in tissue engineering," *Annals of Biomedical Engineering*, vol. 47, no. 2, pp. 354–365, 2019.

[10] J. Chen, C. Ye, Z. Yang et al., "Study on the effect of macrophages on vascular endothelium in mice with different TCM syndromes of dyslipidemia and its biological basis based

on RNA-seq Technology," *Frontiers in Pharmacology*, vol. 12, Article ID 665635, 2021.

[11] R. J. Roman, "P-450 metabolites of arachidonic acid in the control of cardiovascular function," *Physiological Reviews*, vol. 82, no. 1, pp. 131–185, 2002.

[12] T. Wang, Y. Han, H. Li et al., "Proinflammatory lipid signals trigger the health effects of air pollution in individuals with prediabetes," *Environmental Pollution*, vol. 290, Article ID 118008, 2021.

[13] B. Z. Gao, J. C. Chen, L. H. Liao, J. Q. Xu, X. F. Lin, and S. S. Ding, "Erchen decoction prevents high-fat diet induced metabolic disorders in C57BL/6 mice," *Evidence-Based Complementary and Alternative Medicine*, vol. 2015, Article ID 501272, 9 pages, 2015.

[14] P. Scicchitano, F. Cortese, M. Gesualdo et al., "The role of endothelial dysfunction and oxidative stress in cerebrovascular diseases," *Free Radical Research*, vol. 53, no. 6, pp. 579–595, 2019.

[15] A. K. Gitt, D. Lautsch, J. Ferrières et al., "Cholesterol target value attainment and lipid-lowering therapy in patients with stable or acute coronary heart disease: results from the Dyslipidemia International Study II," *Atherosclerosis*, vol. 266, pp. 158–166, 2017.

[16] Y. Yamada, T. Doi, T. Hamakubo, and T. Kodama, "Scavenger receptor family proteins: roles for atherosclerosis, host defence and disorders of the central nervous system," *Cellular and Molecular Life Sciences*, vol. 54, no. 7, pp. 628–640, 1998.

[17] R. Martín-Venegas, R. Casillas, O. Jáuregui, and J. J. Moreno, "Rapid simultaneous analysis of cyclooxygenase, lipoxygenase and cytochrome P-450 metabolites of arachidonic and linoleic acids using high performance liquid chromatography/mass spectrometry in tandem mode," *Journal of Pharmaceutical and Biomedical Analysis*, vol. 56, no. 5, pp. 976–982, 2011.

[18] V. Y. Ng, Y. Huang, L. M. Reddy, J. R. Falck, E. T. Lin, and D. L. Kroetz, "Cytochrome P450 eicosanoids are activators of peroxisome proliferator-activated receptor α," *Drug Metabolism and Disposition*, vol. 35, no. 7, pp. 1126–1134, 2007.

[19] Y. Deng, K. N. Theken, and C. R. Lee, "Cytochrome P450 epoxygenases, soluble epoxide hydrolase, and the regulation of cardiovascular inflammation," *Journal of Molecular and Cellular Cardiology*, vol. 48, no. 2, pp. 331–341, 2010.

[20] A. A. Spector, "Arachidonic acid cytochrome P450 epoxygenase pathway," *Journal of Lipid Research*, vol. 50, pp. S52–S56, 2009.

[21] Z. Cai, G. Zhao, J. Yan et al., "CYP2J2 overexpression increases EETs and protects against angiotensin II-induced abdominal aortic aneurysm in mice," *Journal of Lipid Research*, vol. 54, no. 5, pp. 1448–1456, 2013.

[22] Y. Deng, M. L. Edin, K. N. Theken et al., "Endothelial CYP epoxygenase overexpression and soluble epoxide hydrolase disruption attenuate acute vascular inflammatory responses in mice," *The FASEB Journal*, vol. 25, no. 2, pp. 703–713, 2011.

[23] K. N. Theken, R. N. Schuck, M. L. Edin et al., "Evaluation of cytochrome P450-derived eicosanoids in humans with stable atherosclerotic cardiovascular disease," *Atherosclerosis*, vol. 222, no. 2, pp. 530–536, 2012.

[24] S. Ding, Q. Chen, Y. Huang et al., "Exploring miRNA-related molecular targets of erchen decoction against lipid metabolism disorder using A network pharmacologic approach," *Combinatorial Chemistry & High Throughput Screening*, vol. 25, pp. 986–997, 2022.

[25] F. Donohoe, M. Wilkinson, E. Baxter, and D. J. Brennan, "Mitogen-Activated protein kinase (MAPK) and obesity-related cancer," *International Journal of Molecular Sciences*, vol. 21, no. 4, Article ID 1241, 2020.

[26] S. Ding, J. Kang, L. Tong, Y. Lin, L. Liao, and B. Gao, "Erchen decoction ameliorates lipid metabolism by the regulation of the protein CAV-1 and the receptors VLDLR, LDLR, ABCA1, and SRB1 in a high-fat diet rat model," *Evidence Based Complementary and Alternatative Medicines*, vol. 2018, Article ID 5309490, 12 pages, 2018.

[27] H. Mangge, K. Becker, D. Fuchs, and J. M. Gostner, "Antioxidants, inflammation and cardiovascular disease," *World Journal of Cardiology*, vol. 6, no. 6, pp. 462–477, 2014.

[28] S. Panday, S. Kar, and M. Kavdia, "How does ascorbate improve endothelial dysfunction?-a computational analysis," *Free Radical Biology and Medicine*, vol. 165, pp. 111–126, 2021.

[29] D. Bishop-Bailey and J. Wray, "Peroxisome proliferator-activated receptors: a critical review on endogenous pathways for ligand generation," *Prostaglandins & Other Lipid Mediators*, vol. 71, no. 1-2, pp. 1–22, 2003.

[30] J. Chen, C. Ye, X. Hu et al., "Serum metabolomics model and its metabolic characteristics in patients with different syndromes of dyslipidemia based on nuclear magnetic resonance," *Journal of Pharmaceutical and Biomedical Analysis*, vol. 167, pp. 100–113, 2019.

[31] S. L. Hoopes, V. Garcia, M. L. Edin, M. L. Schwartzman, and D. C. Zeldin, "Vascular actions of 20-HETE," *Prostaglandins & Other Lipid Mediators*, vol. 120, pp. 9–16, 2015.

[32] R. Werida, I. Khairat, and N. F. Khedr, "Effect of atorvastatin versus rosuvastatin on inflammatory biomarkers and LV function in type 2 diabetic patients with dyslipidemia," *Biomedicine & Pharmacotherapy*, vol. 135, Article ID 111179, 2021.

[33] A. Jahangiri, M. Barzegar-Jalali, A. Garjani et al., "Evaluation of physicochemical properties and in vivo efficiency of atorvastatin calcium/ezetimibe solid dispersions," *European Journal of Pharmaceutical Sciences*, vol. 82, pp. 21–30, 2016.

[34] M. Dai, L. Wu, Z. He et al., "Epoxyeicosatrienoic acids regulate macrophage polarization and prevent LPS-induced cardiac dysfunction," *Journal of Cellular Physiology*, vol. 230, no. 9, pp. 2108–2119, 2015.